UCLA
UCLA Electronic Theses and Dissertations

Title

Preparation, Characterization, and Device Applications of Zinc Tin Nitride and Zinc Tin Oxynitride Materials

Permalink

https://escholarship.org/uc/item/2pg6111r

Author

Ye, Shenglin

Publication Date

2015

Peer reviewed|Thesis/dissertation

UNIVERSITY OF CALIFORNIA

Los Angeles

Preparation, Characterization, and Device Applications of Zinc Tin Nitride

and Zinc Tin Oxynitride Materials

A dissertation submitted in partial satisfaction of the

requirements for the degree Doctor of Philosophy

in Materials Science and Engineering

by

Shenglin Ye

2015

ABSTRACT OF THE DISSERTATION

Preparation, Characterization, and Device Applications of Zinc Tin Nitride

and Zinc Tin Oxynitride Materials

by

Shenglin Ye

Doctor of Philosophy in Materials Science and Engineering

University of California, Los Angeles, 2015

Professor Dwight Christopher Streit, Chair

This dissertation presents a comprehensively theoretical and experimental study on zinc tin nitride and zinc tin oxynitride materials. The purposes of this combinatorial study are to understand the fundamental properties of these two materials, and to examine the potential of these two materials for future optoelectronic applications. These fundamental properties are crystal structure, surface morphology, chemical composition, band structures, and optical as well as electrical properties.

Zinc tin nitride ($ZnSnN_2$) thin films have been synthesized on c-plane sapphire substrates and (0001) GaN templates by the reactive radio-frequency (RF) magnetron sputtering method. The properties are investigated by theoretical calculations and experimental results. In terms of theoretical calculation, the lattice constants a, b and c are calculated by using the density functional theory (DFT) method. These constants are comparable to our experimental results as

well as previous calculations. In the case of experimental results, the impacts of substrate temperatures and the ratios of $N_2/(N_2+Ar)$ on films' properties are fully characterized by using various kinds of techniques including X-ray diffraction (XRD), Raman spectroscopy, X-ray photoemission spectroscopy (XPS), scanning electron microscopy (SEM), atomic force microscopy (AFM), Hall effect measurement, and UV-Vis-NIR spectrometry. By optimizing the growth conditions, $ZnSnN_2$ thin films with an average grain size larger than reported results have been obtained. Additionally, for the first time, the valence band structure of $ZnSnN_2$ has been investigated by XPS analysis. The result is consistent with our calculated density of states (DOS). The vibrational modes of $ZnSnN_2$ are also studied by Raman spectroscopy. The Schottky-behavior diodes with a structure of $ZnSnN_2$/GaN heterojunctions have been successfully fabricated, using the standard fabricating process for semiconductor devices. Standard electrical measurements such as C-V measurements reveal the height of the Schottky barrier at the interface between $ZnSnN_2$ and GaN, as confirmed by XPS measurement for band alignment of $ZnSnN_2$/GaN heterojunctions.

Zinc tin oxynitride (ZnSn(ON)) thin films have been deposited on corning 1737 glass substrates and SiO_2/Si wafers by the reactive RF-magnetron sputtering method. By optimizing the O_2 contents in the mixture of total reactive gas, ZnSn (ON) thin films with a Hall mobility of 45 cm^2 $V^{-1}s^{-1}$ and a carrier concentration of 1.63×10^{18} cm^{-3} have been obtained. Additionally, for the first time, thin film transistors (TFTs) based on ZnSn(ON) have been successfully fabricated. The mean linear field effect mobility can reach to 39.6 cm^2 $V^{-1}s^{-1}$, which is in a good agreement with the Hall measurements. Preliminary results show that ZnSn(ON) is a promising candidate for next-generation oxynitride channel layers.

The dissertation of Shenglin Ye is approved.

Eric Pei-Yu Chiou

Mark S. Goorsky

Yang Yang

Dwight Christopher Streit, Committee Chair

University of California, Los Angeles

2015

Table of Contents

List of Figures

List of Tables

Acknowledgments

This work could not have been accomplished without the support and guidance of many people. I would like to express my deepest appreciation to them and my sincerest thanks.

First, I owe thanks to Prof. Dwight Streit, my Ph.D. research advisor, for the opportunity to participate in the dynamic and distinguished research of his group. During the years, I have never been short of encouragement, trust, and inspiration from my advisor, for which I am most thankful.

I would also like to thank my committee members, Prof. Yang Yang , Prof. Eric Pei-Yu Chiou, and Prof. Mark Goorsky, for their mentorship.

I will not forget to thank my dearest colleagues in the Prof Dwight's Lab: Jiechen Wu, Jinhee Park, Xiaoxing Lu and Teresa Ha. I will miss our collaboration and discussions with one another. I am glad to have the opportunity to work and study in a nice and engaging environment.

Also, I am grateful for my peers' help. Jeff Mackay from Prof Goosky's lab helped me with many XRD works and the useful advice he gave to me for characterization of crystal structures. Yi Xia from Prof. Ozolin's group guided me with analyzing the materials' properties by DFT method. He also spent much time on calculations for my materials. Tze-bin Song from Prof Yang Yang's group helped me with obtaining high quality of SEM images and obtaining the first Raman spectra for $ZnSnN_2$. Jing Gao from Prof Yang yang's lab gave me many useful suggestions for preparing this presentation and with AFM imaging. Wenbo Xin from Prof Jenn-ming Yang's lab assisted me with analysis of TEM images. Huajun Chen from Prof Yang yang's lab provided me with the help in fabricating the thin film transistors.

I want to thank all the staffs in the integrated system nanofabrication cleanroom (ISNC) of California nanosystem institute (CNSI) in UCLA. They gave me a lot of supports during these past four years.

I also appreciate Wilson Lin for offering valuable supports for the standard electrical measurements in UCLA Microlab.

At last, I thank my wife, Xiaolin Li, my parents, my grandparents, my wife's parents, and my other family members. I would not have reached this step without their belief in me.

VITA

| 2004 | B.S. Instrumental Technology, University of Shanghai for Science and Technology, Shanghai, China |

| 2007 | M.S. Optical Engineering, University of Shanghai for Science and Technology, Shanghai, China |

| 2008-2010 | R & D Engineer, Optorun Co.,Ltd. Saitama-Ken, Japan |

| 2014 | M.S. Materials Science and Engineering, University of California, Los Angeles, CA, USA |

| 2011-2015 | Graduate Student Researcher, Department of Materials Science and Engineering, University of California, Los Angeles, CA, USA |

Publications

Shenglin Ye, Yi Xia, Jeffrey Mckay, Jiechen Wu, Xiaoxing Lu, Jinhee Park, Dwight Streit, "Valence band structure of $ZnSnN_2$ studied by x-ray photoelectron spectroscopy," Spring Materials Research Society Meeting, San Francisco, April 8th 2015

Shenglin Ye, Yi Xia, Jeffrey Mckay, Jiechen Wu, Xiaoxing Lu, Jinhee Park, Dwight Streit, "Preparation and characterization of next generation nitrides; $ZnSnN_2$", Tech Forum, UCLA, February 3rd 2015

Wan-Ching Hsu, Huanping Zhou, Song Luo, Tze-Bin Song, Yao-Tsung Hsieh, Hsin-Sheng Duan, Shenglin Ye, Wenbing Yang, Chia-Jung Hsu, Chengyang Jiang, Brion Bob, and Yang Yang. Spatial Element Distribution Control in a Fully Solution-Processed Nanocrystals-Based 8.6% Cu2ZnSn(S,Se)4Device. ACS Nano, 8 (9) (2014)

Huanping Zhou, Tze-Bin Song, Wan-Ching Hsu, Song Luo, Shenglin Ye, Hsin-Sheng Duan, Chia-Jung Hsu, Wenbing Yang and Yang Yang. Rational Defect Passivation of $Cu_2ZnSn(S,Se)_4$ Photovoltaics with Solution-Processed Cu_2ZnSnS_4:Na Nanocrystals. Journal of American Chemical Society, 135, 15998 (2013)

Wan-Ching Hsu, Huanping Zhou, Song Luo, Shenglin Ye, Tze-Bin Song, Yang Yang. Grain Growth of CZTS from Nanoparticle Selenization, 39th IEEE Photovoltaic Specialists Conference, Tampa, FL. (2013)

Jingbi You, Chun-Chao Chen, Ziruo Hong, Ken Yoshimura, Kenichiro Ohya, Run Xu, Shenglin Ye, Jing Gao, Gang Li, and Yang Yang. 10.2% Power Conversion Efficiency Polymer Tandem Solar Cells Consisting of Two Identical Sub-Cells. Advanced Materials, 25, 3973-3978 (2013)

Shenglin Ye, Xiaohui Tan, Minlin Jiang, Bin Fan, Ken Tang, Songlin Zhuang, "The impact of different Na-incorporating methods on CIGS thin film solar cells with a Na-free substrate," Applied Optics, vol 49, no 12, 2010

Xiaohui Tan, Shenglin Ye, Bin Fan, Ken Tang, Xu Liu, " Effects of Na incorporated at different periods of deposition on Cu(In,Ga)Se2 films," Applied Optics, vol 49, no 16, 2010

Shenglin Ye et al.,"Valence band structure of $ZnSnN_2$ investigated by X-ray photoemission spectroscopy and DFT calculation", in progress

Shenglin Ye et al.,"Vibration modes of $ZnSnN_2$ studied by Raman spectroscopy", in progress

Shenglin Ye et al.,"Tuning the band alignment of $ZnSnN_2$/GaN heterojunctions for versatile opto-electronic applications", in progress

Shenglin Ye et al.,"Effect of surface treatment on the band alignment of AlGaN/GaN heterojunctions", in progress

Chapter 1 Introduction

This introduction starts with the current development status and drawbacks of III-nitride semiconductor materials, and explains the motivation of finding next-generation nitrides (Section 1.1). Then, it reviews the background and history of Zn-IV-nitride and oxynitride materials, and summarizes the fundamental structural and opto-electrical properties of those materials (Section 1.2). Later, the potential applications of Zn-IV-nitride and oxynitride compounds are described (Section 1.3). Finally, this introduction concludes with the scope and organization of this thesis (Section 1.4).

1.1 Motivation

In the past 20 years, due to their unique properties, group III-nitride semiconductor materials (AlN,GaN and InN) have been widely applied in the field of optoelectronics[1].[2] For example, the band gap of $In_{1-x}Ga_xN$-based materials can be adjusted across the whole visible spectrum by controlling the ratio of Ga to In in order to match the AM 1.5 solar spectrum. The power conversion efficiency of $In_{1-x}Ga_xN$-based thin film solar cells can reach 33%, which is a theoretical maximum efficiency[3].[4] In addition, using the method of band gap engineering, solid state lighting can be achieved based on the GaN/ $In_{1-x}Ga_xN$ hetero-junction structure. This is one of the most important prerequisites for manufacturing LED displays and high-performance laser diodes. In 2014, the Nobel physics prize was awarded to Isamu Akasaki, Hiroshi

Amano and Shuji Nakamura for their contributions to improving the quality of GaN materials and invention of the blue LEDs [5].

However, group III-nitrides, especially $In_{1-x}Ga_xN$-based semiconductor materials, also have their drawbacks. First, both indium and gallium are not earth-abundant elements, which will limit the mass production of photovoltaic modules and LED displays because the eventual costs of these optoelectronic devices are largely dependent on the availability of raw materials. Second, indium-based materials are not environmentally friendly due to the fact that indium, as a kind of heavy metal, features potential possibilities of bio-toxicity [6]. Therefore, in order to meet the needs of environmental safety as well as reduction of production costs, people are now looking for next-generation nitrides whose electrical and optical properties are comparable to their III-nitride counterparts.

1.2 Background of Zn-IV-nitride and Zn-IV-oxynitride materials

1.2.1 Zn-IV-N_2 group materials

Zn-IV-N_2 semiconductor materials are widely regarded as a favorable candidate for replacing with group III-nitrides according to careful theoretical calculation as well as related experimental results. Zn-IV-N_2 semiconductors, where IV refers to Si, Ge or Sn, consist solely of earth-abundant, non-toxic and inexpensive elements [7],[8]. According to the US geological survey, tin and zinc are much more abundant than indium (10^2 to 10^3 times) [9] [10].The details are shown in the Figure 1.1. The electrical and optical properties of this kind of nitride materials are similar to III-nitrides. Meanwhile, replacing one group III element (Ga, In or Al) with a

2

combination between Zn and group IV elements could provide more possibilities to broaden the range of physical and chemical properties. Compared to group III-nitrides, Zn-IV-N$_2$ materials have some unique advantages.
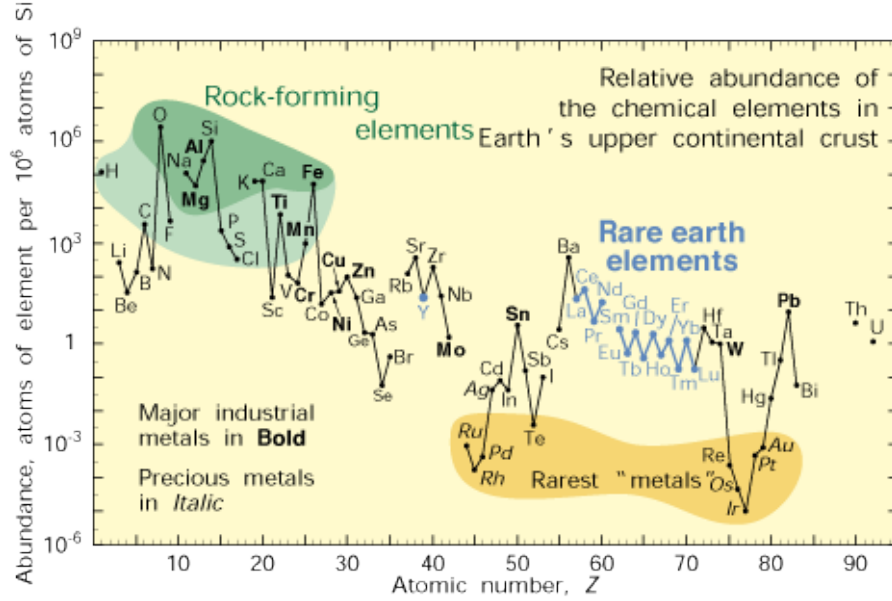
Figure 1.1 The relative abundance of elements in the Earth's upper continental crust in terms of the US Geology Survey [9]

First, various kinds of thermodynamically stable compounds will be formed based on this kind of novel materials. Second, the lattice mismatch among Zn-IV-N$_2$ materials is smaller than the mismatch generated from group III-nitrides, which could be used to reduce the stain-induced polarization field in the heterojunctions and to improve the quality of preparation of heterojunctions. Finally, due to a different point-defect formation mechanism, p-type doping will be more easily realized in Zn-IV-N$_2$ semiconductor materials than in group III-nitrides materials [11]. During the period of GaN research, people were puzzled by how to realize p-type doping in GaN materials until Professor Nakamura found a reasonable way to do it and make blue LED based on GaN homogenous p-n junction structure.

3

The crystal structure of Zn-IV-nitride semiconductor materials is orthorhombic; whose possible space groups are $Pbn2_1$, $Pna2_1$ and $Pmc2_1$. The prototype of these novel compounds is beta-$NaFeO_2$ [11],[12]. Figure 1.1 shows the crystal structure of GaN and Zn-IV-N_2 compounds.

(a)

(b)

(c)
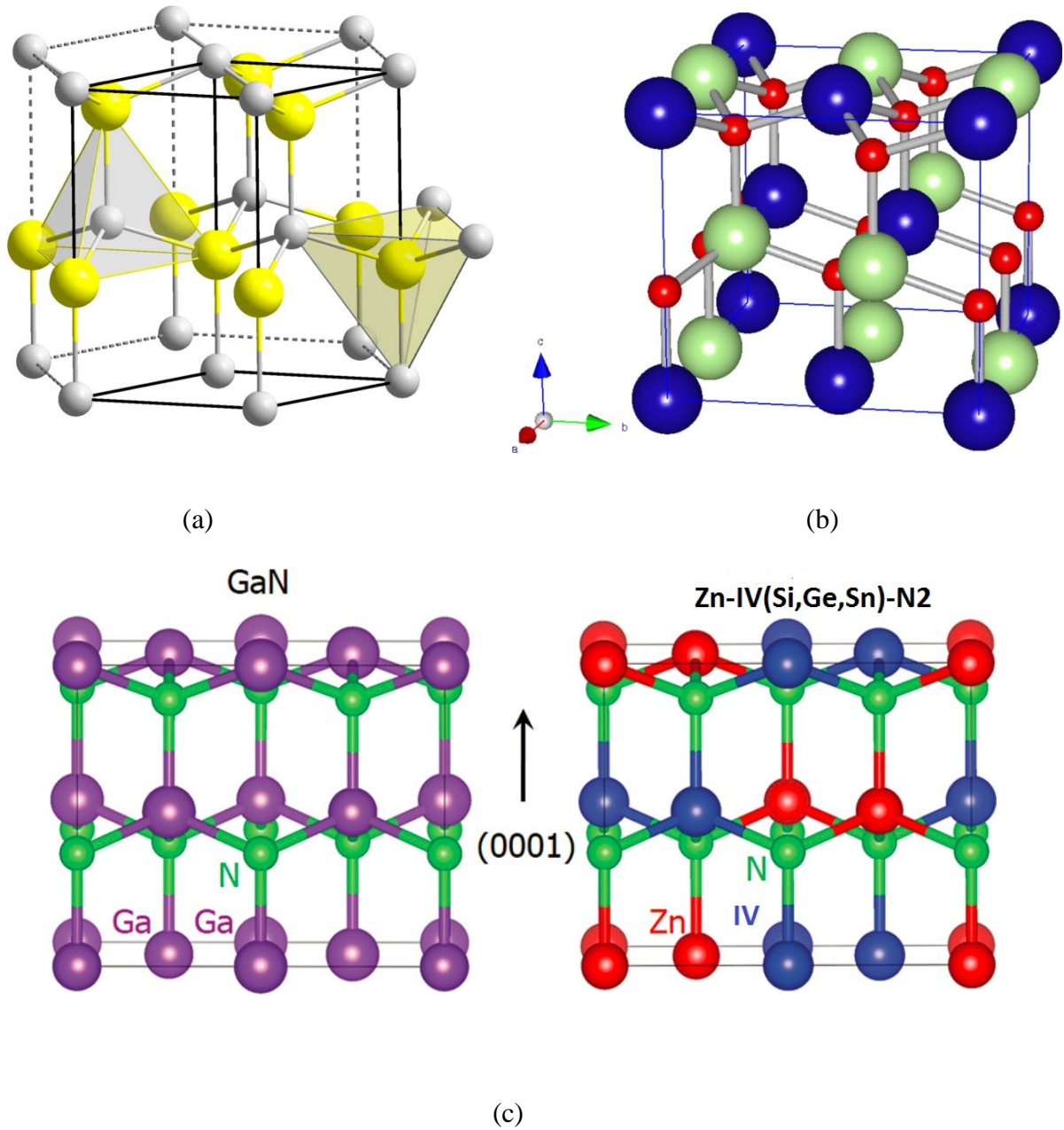
Figure 1.2 Crystal structure of GaN and Zn-IV-N_2 compounds. (a) 3D view of GaN crystal structure: small light grey spheres are N atoms; large yellow spheres are Ga atoms [13]. (b) 3D view of Zn-IV-N_2

4

crystal structure: small red spheres are N atoms, light green spheres are group IV atoms (Si,Sn or Ge) and dark blue spheres are Zn atoms. Adapted from [14] with permission of American Physical Society. (c) wurtzite GaN and orthorhombic $ZnSnN_2$ along the (0001) orientation. Adapted from [15] with the permission of John Wiley and Sons Publisher

How to synthesize Zn-IV-N_2 compounds with high quality is one of the most important premises of current researches on materials' fundamental properties as well as devices' applications.

Preparation of $ZnGeN_2$ was first reported in 1970 based on the reaction of NH_3 with Zn_2GeO_4 or the reaction of metal Zinc with Ge_3N_4 [11],[16].

$$8NH_3 + 3Zn_2GeO_4 \rightarrow 3ZnGeN_2 + N_2 + 3Zn + 12H_2O \qquad (1\text{-}1)$$

$$Ge_3N_4 + 2Zn \rightarrow 2ZnGeN_2 + Ge \qquad (1\text{-}2)$$
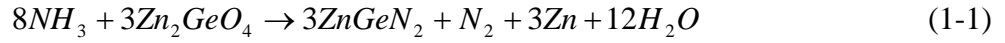
By using the neutron-diffraction method, Wintenberger et al. studied the ordering of cations(Zn and Ge atoms) and reported the structure of $ZnGeN_2$ to be orthorhombic (lattice constant: a=6.44 Å, b=5.45 Å and c=5.19Å) [17]. In 1992, Endo et al. demonstrated growth of the single crystal $ZnGeN_2$ using the high-pressure synthesis method. Their $ZnGeN_2$ crystals were opaque with a high degree of impurities [11],[18]. From 1999 to 2005, some research groups reported to synthesize $ZnGeN_2$ thin films through chemical vapor deposition (CVD) or the RF-sputtering method. Zhu et al. used metal-organic chemical vapor deposition (MOCVD) to grow thin films on the c-plane or r-plane sapphire substrates incorporated by a GaN buffer layer [19]. According to the experimental results, they pointed out that their $ZnGeN_2$ thin films featured disorder on the Zn or Ge sublattice. Misaki et al. prepared $ZnGeN_2$ thin films on sapphire substrates without using GaN buffer layer by plasma-enhanced MOCVD [20],[21],[22], and their measurement of the band gap of $ZnGeN_2$ was about 3.3 eV. In addition, Kikkawa et al. used the RF-sputtering method to deposit $ZnGeN_2$ thin films on silicon as well as glass substrates. The band gap of thin

films was indicated to be around 3.1eV [23]. In 2008, Du et al. used vapor-liquid-solid (VLS) technique to grow the polycrystalline $ZnGeN_2$ materials. This growth method resulted in large needle-shaped crystals with a few microns in diameter and hundred microns in length [11],[24]. The band gap of these materials was reported to be 3.4 eV, which was measured by photoluminescence technique.

Endo et al also successfully synthesized $ZnSiN_2$ powder by using the high-pressure method [18]. Relying on optical absorption analysis, they reported the band gap of this material to be 3.64eV. $ZnSiN_2$ thin films were reported to be grown on different substrates by a few groups. Cook and Muth et al. used the MOCVD technique to prepare $ZnSiN_2$ thin films on a r-plane sapphire substrate, calculated the refraction indices of these films and determined the band gap to be 4.4 eV [25]. Osinsky et al. synthesized $ZnSiN_2$ films based on SiC substrates [26]. And Mintairov et al. reported infrared reflection of $ZnSiN_2$ crystalline films on r-sapphire substrates with the help of infrared spectroscopy [27]. Crystal structure of $ZnSiN_2$ is also orthorhombic and their obtained lattice constants were a=6.18 Å, b=5.34 Å and c=5.01 Å [28].

There are few reports about growing $ZnSnN_2$ materials due to the difficulty of their preparation. Recently, Quayle et al. synthesized polycrystalline $ZnSnN_2$ by a plasma-assisted vapor-liquid-solid method (PAVLS)[11],[29] for the first time. Based on the results of X-ray diffraction (XRD) measurement, the crystal structure of this material is found to be orthorhombic and their obtained lattice parameters were a=6.75 Å, b=5.84 Å and c=5.42 Å. In addition, they also indicated that the band gap of $ZnSnN_2$ was about 1.7eV using photoluminescence and photoluminescence excitation (PLE) spectroscopy. N. Feldberg et al. reported growth of single or textured polycrystalline $ZnSnN_2$ thin films through the molecular beam epitaxy(MBE) technique[30]. They indicated that cation sublattice disorder leads to a dramatic effect on the

bandgap as well as crystal structure. In 2013, Lahourcade et al. used the RF-sputtering method to synthesize $ZnSnN_2$ thin films on c-plane sapphire and GaN substrates. These films feature orthorhombic crystal structure with Pna2_1 space group. The optical band gap and carrier concentration were estimated to be 2 eV and 10^{21} cm^{-3} respectively based on ellipsometry and Hall measurement [12].

Figure 1.2 shows the bandgap as a function of lattice constant "a" for III-nitrides as well as Zn-IV-N_2 materials. In this diagram, open symbols represent the calculated data and solid circles indicate the experimental results. The experimental lattice constants, bandgaps and bowing parameters of III-nitrides (AlN, GaN and InN) are from [31]. In addition, The experimental parameters for Zn-IV-N_2 materials are taken from [24],[26],[29].
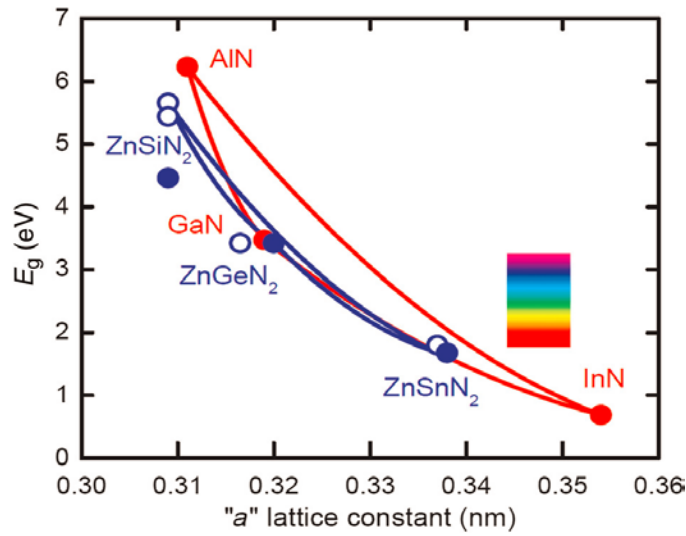
Figure 1.3 Band gaps versus lattice constants "a" in III-N and Zn-IV-N_2 nitrides. open circles: calculated values; filled circles: experimental values. (Reprinted from [29] with the permission of Cambrige University Press)

Table 1.1 is the summary of lattice parameters and band gap for Zn-IV-N2 compound. Here, all theoretical calculation data are from [11]. In terms of experimental results, the data are taken from [12],[17],[24],[25],[26],[27],[29].

Table 1.1 Parameters (a,b,c) and Band gap(Eg) of Zn-IV-N_2 compound

Zn-IV-N_2 compound		Theoretical calculation*	Experimental results
ZnGeN$_2$	a(Å)	6.42	6.44[17]
	b (Å)	5.54	5.45[17]
	c (Å)	5.27	5.19[17]
	Eg(eV)	3.60	3.4 [24]
ZnSiN$_2$	a(Å)	6.16	6.18[27]
	b (Å)	5.41	5.35[27]
	c (Å)	5.11	5.05[27]
	Eg(eV)	5.92	4.46[25,26]
ZnSnN$_2$	a(Å)	6.70	6.75[29]
	b (Å)	5.80	5.84[29]
	c (Å)	5.53	5.46[29]
	Eg(eV)	2.15	1.7[29] or 2.0[12]

* From [11]

1.2.2 Zn-IV-oxynitride materials

Zinc germanium oxynitride (ZnGe(ON)) was first found by Mauanye et al. when they synthesized ZnGeN$_2$ compound[16]. In 2007, Lee et al. reportedly prepared ZnGe(ON) using the reaction between GeO$_2$ and ZnO with NH$_3$ flow at 850 ˚C. This material exhibits a wurtzite crystal structure with space group P6$_3$mc. And its band gap wa confirmed to be 2.7eV [32]. Then, in 2009, researcher groups from France and Sweden also used a similar method to grow zinc

germanium oxynitride materials [33],[34]. Figure 1.3 demonstrates the refined crystal structure of zinc germanium oxynitride compound.

Until now, there are no reports about growth of zinc silicon oxynitride or zinc tin oxynitride materials in the literature.
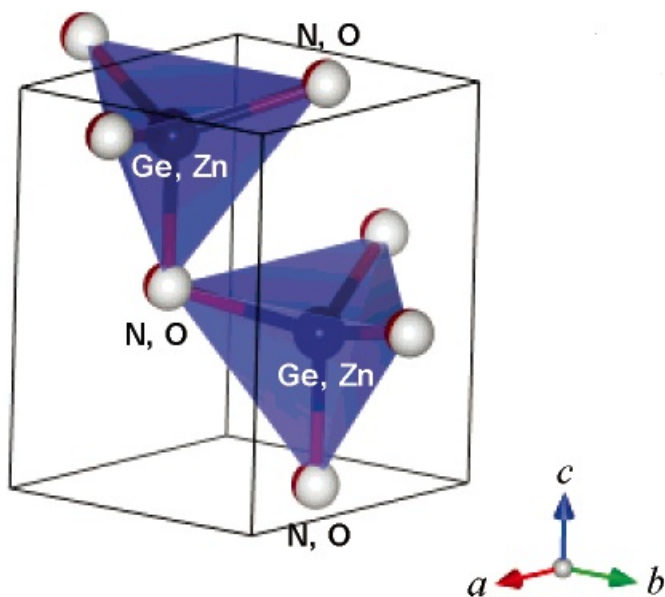
Figure 1.4 Crystal structure of $(Zn_{1.44}Ge)(N_{2.08}O_{0.38})$ based on the $(Ge,Zn)(N,O)_4$ tetrahedron (Reprinted from [32] with the permission of American Chemical Society)

1.3 Applications of Zn-IV-nitride and oxynitride materials

Development of Zn-IV-N_2 materials is still in the initial stage, but researchers have already tried to find possible applications for these compounds. Osinsky et al. reported a novel device configuration for SiC-based bipolar transistors with incorporation of $ZnSiGeN_2/ZnGeN_2$

hetero-structure as the n-type emitters. They found that the contact resistance between metal and

$ZnSi_{1-x}Ge_xN_2$ could reach to $5.3 \times 10^{-7} \Omega\text{-cm}^2$ and this value is similar to the best one achieved

based on n-GaN or n-GaAs materials [26]. Figure 1.4 demonstrates the schematic of SiC-based

bipolar transistors with $ZnSi_xGe_{1-x}N_2$ emitters. In 2013, Atchara Punya et al. investigated the

band offset among $ZnGeN_2$, $ZnSnN_2$, GaN and ZnO using first principle calculation. They

pointed out that the heterojunctions of $ZnGeN_2$/GaN and ZnO/GaN are type II structures, which

are useful for charge separation at the junctions' interfaces. They also proposed a possible

columnar solar cell structure based on the concept of band alignment among these materials. And

figure 1.5 shows the schematic of this kind of photovoltaic cells [35].

$ZnSnN_2$ compound has been regarded as one kind of most promising materials for future

photovoltaic application due to its relatively small band gap, which is reported to be between

1.4eV and 2eV [12],[29],[30].
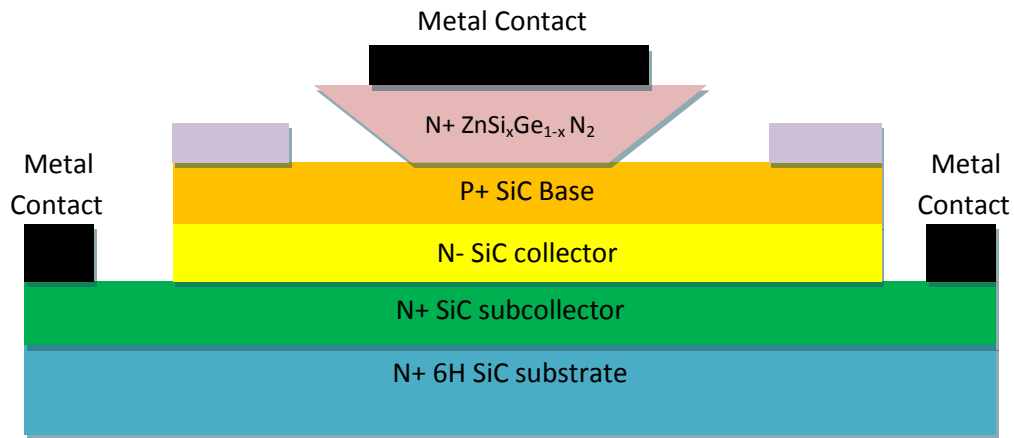
Figure 1.5 Schematic of SiC-based bipolar transistors with ZnSixGe1-xN$_2$ emitters (Adapted from [26], Copyrighted by IEEE)

10

Figure 1.6 Schematic of nanosize columnar solar cell of ZnO, GaN and $ZnGeN_2$ (Reprinted from [35] with the permission of American Physical Society)

Recently, zinc germanium oxynitride has been reported to be a promising material for photocatalytic overall water splitting. Lee et al. obtained water splitting under the illumination from ultraviolet to visible light using $(Zn_{1.44}$ $Ge)(N_{2.08}O_{0.38})$ powders with 5 wt% RuO_2 nanoparticles on their surfaces[32]. By trying various kinds of synthetic methods for ZnGe(ON) as well as adjusting compound's composition, F.Tessier et al. indicated that low Zn/Ge ratio and high crystallization status are two important factors for achieving photocatalytic water splitting[33]. K.Takanabe et al. also improved the photocatalytic activity of ZnGe(ON) material through modification of zinc germanium oxynitride with metal doping as well as post-calcination[34]. Figure 1.6 demonstrates the schematic of overall water splitting [33].

11
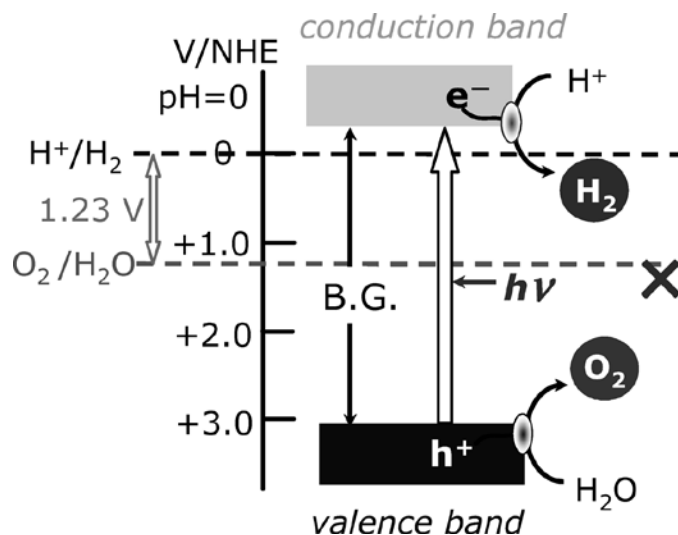
Figure 1.7 Schematic of overall water splitting (Reprinted from [33] with the permission of American Chemical Society)

1.4 Scope and Organization

In this thesis, zinc tin nitride and oxynitride materials have been synthesized by the RF-sputtering method. These materials' properties such as crystal structures, lattice parameters, electronic band configuration etc. are investigated by theoretical calculations and experimental results. The initial devices based on $ZnSnN_2$ as well as ZnSn(ON) compounds have been fabricated and preliminary results indicate that these novel materials are some of the most potential candidates for future optoelectronic applications. Chapter 2 introduces the fundamental principle of density functional theory (DFT), reviews the history of DFT calculation about Zn-IV-N_2 group materials and describes our theoretical calculation results for zinc tin nitride compound. Chapter 3 summaries growth of $ZnSnN_2$ thin films on sapphire and GaN substrates and characterization of films' properties through many kinds of techniques such as X-ray diffraction(XRD), X-ray photoemission spectroscopy(XPS), etc. And these values of materials'

12

properties obtained by experiments match with our calculated data. This chapter also discusses device applications of $ZnSnN_2$. The first schottky-behavior diode has been successfully fabricated. This device is based on $ZnSnN_2$/GaN heterojunctions structure. Standard electrical measurements such as C-V measurement reveal the height of schottky barrier at the interface between $ZnSnN_2$ and GaN, as confirmed by XPS measurement. Chapter 4 summarizes the preparation and characterization of ZnSn(ON) thin films, and studies the effect of $O_2/(N_2+Ar)$ ratio on films' properties. Chapter 4 also demonstrates a novel thin film transistor structure with ZnSn(ON) active channel material. It describes the fabrication process, and demonstrates the achievement of the preliminary results. Chapter 5 concludes this study and opens avenues for future research.

Chapter 2 Theoretical calculation of materials' properties based on density functional theory (DFT) method

2.1 Introduction to density functional theory (DFT) method

Density functional theory (DFT) is one of the most popular and successful computational quantum mechanical modeling approaches in condensed-matter physics, computational physics, and computational chemistry. It is used to study the electron structure of many-body systems. For example, DFT can be applied for calculating the binding energy of molecules as well as the band structure of solids. And DFT is also a method which relies on a rigid conceptual framework. In the next section, we will introduce more details about the DFT method [36].

2.1.1 Hohenberg-Kohn theorems and Kohn-Sham equations

The DFT method is the fundamental framework of first-principles electronic structure theory, which offers a "mean-field" rule to obtain the effective potential affected by an electron with other electrons and the nuclei in the solid [11]. The DFT method is mainly based on two Hohenberg and Kohn theorems and a series of self-consistent equations derived by Kohn and Sham in the mid-1960s [11],[36],[37],[38], [39]. Due to his pioneering work, Kohn was awarded the Nobel Prize in Chemistry 1998 [40].

The first Hohenberg and Kohn theorem (H-K theorem) is: "The ground-state energy from Schrödinger's equation is a unique functional of the electron density"[37],[39]. This H-K theorem indicates that the ground-state electron density could determine all the ground state

properties of a many-electron system. The importance of this theorem is to decrease the problem with 3N dimensions to a problem with just three dimensions for a many-body problem of N electrons, by finding a function of the electron density [36],[37],[39]. The second H-K theorem defines an energy functional for the system; "The electron density that minimizes the energy of the overall functional is the true electron density corresponding to the full solution of the Schrödinger equation". This theorem confirms that the energy functional could be minimized by a correct electron density of ground state [36],[37],[39].

Although Hohenerg and Kohn theorems have proven that effective potentials could be determined by the electron density independently, the exact functional forms of energy and potential are still unknown. Then, a reasonable approximation is necessary [11]. The most common approximation is Kohn-Sham functional combined with the local density approximation (LDA) [11],[28],[38],[41]. By using this approach, the functional form demonstrated by H-K theorems can be written down in terms of the single-electron wave functions for solving a one-particle Schrödinger equation. The Kohn-Sham (K-S) equations are listed as follows:

$$\left[-\frac{\hbar^2}{2m}\nabla^2 + V_s(\vec{r}) \right] \Psi_i(\vec{r}) = \varepsilon_i \Psi_i(\vec{r})$$

$$n_s(\vec{r}) = \sum_i^N \left| \Psi_i(\vec{r}) \right|^2$$

(2-1)

In equation (2-1), $n_s(\vec{r})$ indicates the density of electrons in a many-body system; $\Psi_s(\vec{r})$ is the one-electron wave function located at the position $\vec{r}$; and $V_s(\vec{r})$ means the effective single-particle potential. And $V_s(\vec{r})$ can also be represented by three different potentials:

$$V_s(\vec{r}) = V(\vec{r}) + V_H(\vec{r}) + V_{XC}(\vec{r})$$

$$V_H(\vec{r}) = e^2 \int \frac{n_s(\vec{r'})}{\left|\vec{r} - \vec{r'}\right|} d^3r' \tag{2-2}$$

$$V_{XC}(\vec{r}) = \frac{\delta E_{XC}(\vec{r})}{\delta n_s(\vec{r})}$$

Here, $V(\vec{r})$ is the potential which denotes the interaction between atomic nuclei and an electron;

$V_H(\vec{r})$ is called as the Hartree pontential describing the Coulomb repulsion between electrons;

and $V_{XC}(\vec{r})$ is the exchange-correlation potential, which can be defined as a functional derivative

of the exchange-correlation energy. Because both $V_H(\vec{r})$ and $V_{XC}(\vec{r})$ rely on electron density

$n_s(\vec{r})$ which is related to $\Psi_s(\vec{r})$ as well as $V_s(\vec{r})$, the solution of the Kohn-Sham equations is

self-consistent [36],[38],[39]. The flow chart of solving the K-S equations is outlined in the

Figure 2.1.

```
                    ┌─────────────┐
                    │    Start    │
                    └──────┬──────┘
                           │         ←──────────────────┐
                           ▼                             │
     ┌──────────────────────────────────────────┐       │
     │ Generate  a  trial electron density, $n_s(\vec{r})$ │       │
     └──────────────────┬───────────────────────┘       │
                        ▼                                │
     ┌──────────────────────────────────────────┐       │
     │ Calculate $V_s(\vec{r})$ and $\Psi_s(\vec{r})$  based on $n_s(\vec{r})$ │       │
     └──────────────────┬───────────────────────┘       │
                        ▼                                │
     ┌──────────────────────────────────────────┐       │
     │ Calculate $n_{ks}(\vec{r})$ by solving equation (2-1) │       │
     └──────────────────┬───────────────────────┘       │
                        ▼                                │
                    ◇─────────◇          No              │
                   ╱ $n_{ks}(\vec{r}) \cong n_s(\vec{r})$ ╲ ──────────────┘
                    ◇─────────◇
                        │ Yes
                        ▼
   ┌────────────────────────────────────────────────┐
   │ Export the ground-state electron density, $n_{ks}(\vec{r})$ by │
   │           solving equation (2-1)               │
   └────────────────────┬───────────────────────────┘
                        ▼
                 ┌─────────────┐
                 │     End     │
                 └─────────────┘
```
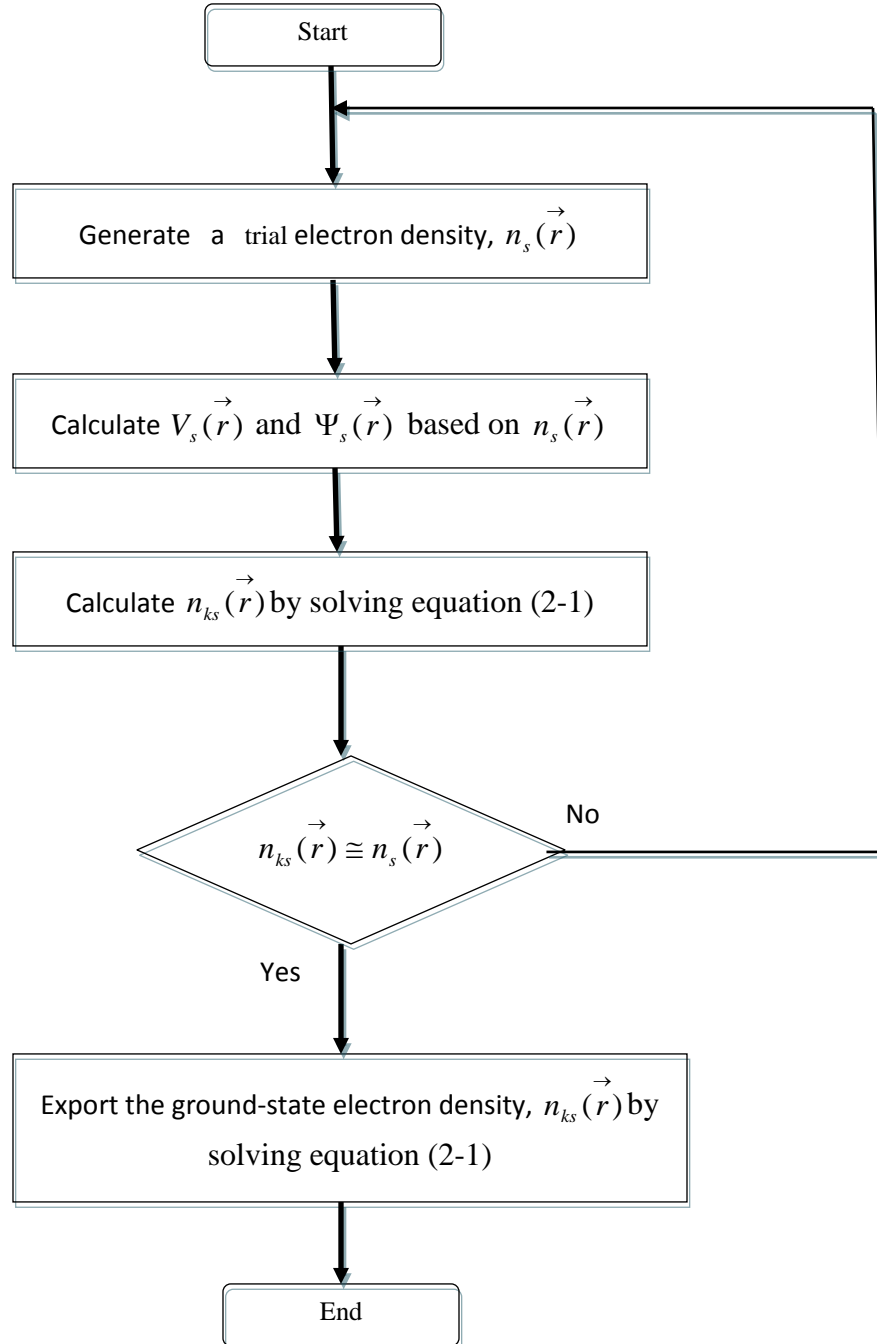
Figure 2.1 Flow chart of solving the Kohn-Sham equations

2.1.2 Overview of different density functional approximations

In order to achieve a more accurate approximation based on the DFT calculation, first, we need to find a well-defined exchange-correlation functional. There are various kinds of functionals and the relationships between them have been illustrated in Figure 2.2 by John Perdew et al. [42]. They used a "Jacob's ladder", which is a terminology from the Bible, to categorize different functionals. From this figure, we can clearly understand that local density or spin-density approximation (LDA or LSDA), generalized gradient approximation (GGA) [43], [44]and meta-GGA [45] construct the bottom rungs of this ladder. These three approximations are most commonly used for the non-empirical DFT calculations. Hyper-GGA and generalized random-phase approximation (RPA) are the fourth and fifth rungs of Jacob's ladder. These two functionals usually feature more physical information with solving the Schrödinger equation more accurately.

HEAVEN OF CHEMICAL ACCURACY

unoccupied $\{\phi_i\}$ ———————— generalized RPA

ε_x ———————— hyper-GGA

τ and/or $\nabla^2 n$ ———————— meta-GGA

∇n ———————— GGA

n ———————— LSD
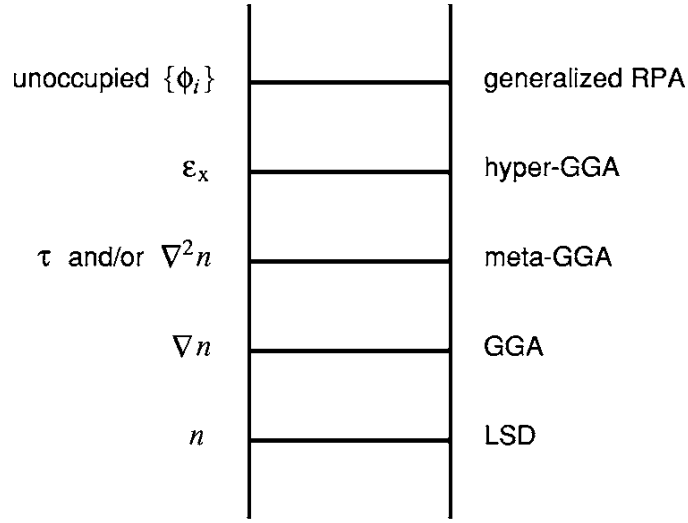
HARTREE WORLD

Figure 2.2 Jacob's ladder of density functional approximations to the exchange-correlation energy (Reprinted from [42] with the permission of AIP publishing)

LDA is one of the simplest approximations to the practical K-S functional, which makes an assumption that the local exchange and correlation energy per particle is equal to the exchange energy for an uniform electron gas having the same density as the local electron density [28],[38],[39]. This relation can be expressed by equation (2-3); here, $\varepsilon_{xc}^{unif}(n)$ is the exchange energy of an uniform electron gas.

$$E_{XC}^{LDA}(n) = \int \varepsilon_{xc}^{unif}(n) \cdot n(\vec{r})d^3 r \qquad (2-3)$$

LSDA is a direct generalization of the LDA with the electron spin:

$$E_{XC}^{LSDA}(n) = \int \varepsilon_{xc}^{unif}(n\uparrow, n\downarrow) \cdot n(\vec{r})d^3 r \qquad (2-4)$$

19

$\varepsilon_{xc}^{unif}(n\uparrow, n\downarrow)$ is the exchange-correlation energy per particle, including uniform spin density $n\uparrow$ and $n\downarrow$ [34,40]. This value can be obtained precisely from the quantum Monte Carlo simulation and other many-electron methods [46].

Compared to LDA, nonempirical GGA is regarded to be more accurate due to the fact that GGA funtional features more physical ingredients than LDA functional. The exchange-correlation energy of GGA is dependent not only on the local electron density but also on the gradient in the electron density. The expression of GGA is listed as follows:

$$E_{XC}^{GGA}(n\uparrow, n\downarrow) = \int \varepsilon_{xc}(n\uparrow, n\downarrow, \nabla n\uparrow, \nabla n\downarrow) \cdot n(\vec{r}) d^3 r \qquad (2\text{-}5)$$

The Perdew-Burke-Ernzerhof (PBE) functional is one of most important nonempirical funtionals of GGA. And this kind of approximation is called PBE GGA [44].

Meta-GGA functional is the third rung of Jacob's ladder. The exchange-correlation energy of meta-GGA include the local electron density $n(\vec{r})$, the first and second derivative of electron density $\nabla n(\vec{r})$, $\nabla^2 n(\vec{r})$ and the Kohn-Sham orbital kinetic energy density $\tau(\vec{r})$ [42],[47],[48].

$$E_{XC}^{MGGA}(n\uparrow, n\downarrow) = \int \varepsilon_{xc}^{MGGA}(n\uparrow, n\downarrow, \nabla n\uparrow, \nabla n\downarrow, \nabla^{2/} n\uparrow, \nabla^2 n\downarrow, \tau\uparrow, \tau\downarrow) \cdot n(\vec{r}) d^3 r$$
$$\tau(\vec{r}) = \frac{1}{2} \sum_i^{occupied} \left| \nabla\Psi_i(\vec{r}) \right|^2 \qquad (2\text{-}6)$$

Generally speaking, LDA and LSDA are local functionals of the electron density. In comparison, GGA belongs to a semi-local functional for the electron density and meta-GGA can be classified as a semi-local functional of both the electron density and the occupied orbitals [40]. And the Tao-Perdew-Staroverov-Scuseria(TPPS) functional represents a commonly used

nonempirical meta-GGA functional, which makes use of the kinetic energy density of the K-S

orbitals $\tau(\vec{r})$ to replace the Laplacian of the electron density $\nabla^2 n(\vec{r})$ in the form of exchange-

correlation energy [48].

The fourth rung of Jacob's ladder is the hyper-GGA method [49],[50]. In hyper-GGA's

equation, the exact exchange energy density $\varepsilon_x(\vec{r})$ has been included.

$$E_{XC}^{HGGA}(n\uparrow,n\downarrow) = \int \varepsilon_{xc}^{HGGA}(n\uparrow,n\downarrow,\nabla n\uparrow,\nabla n\downarrow,\nabla^{2/}n\uparrow,\nabla^2 n\downarrow,\tau\uparrow,\tau\downarrow,\varepsilon_x\uparrow,\varepsilon_x\downarrow)\cdot n(\vec{r})d^3r$$

$$\varepsilon_x(\vec{r}) = -\frac{1}{2n(\vec{r})}\int \frac{\left|\sum_i^{occupied}\Psi_i^*(r')\Psi_i(r)\right|}{|r'-r|}d^3r' \tag{2-7}$$

Hyper-GGA functional is semi-empirical and nonlocal, and defines energy exchange through a

combination between a GGA exchange and the exact change.

Generalized random-phase approximation (RPA) is the last rung of Jacob's ladder, which

includes all of the Kohn-Sham orbitals [51],[52],[53],[54]. The RPA functionals need a lot of

basis sets for calculation and are still not suitable for practical application.

2.2 History of theoretical calculation of Zn-IV-N$_2$ group materials based on DFT method

In 1999, Limpijumong et al. [55] reported the first calculated band-structure of ZnGeN$_2$

materials based on the LDA and linearized muffin-tin orbital (LMTO) method [56],[57]. In 2008,

V.L.Shaposhnikov et al. presented the structural, electronic and optical properties of ZnSiN$_2$ and

ZnGeN$_2$ ternary compounds using pseudo-potential plane-wave methods [11],[58]. Recently,

Lambrecht et al. have carefully studied various kinds of properties of Zn-IV-N_2 materials with the DFT method [7],[59],[60],[61],[62]. They also optimized the band-structure's calculation by incorporating the GW approach [8],[63]. Last year, Chen et al. presented the defect physics and electronic band structure of $ZnSnN_2$ materials using the non-local hybrid functional (HSE) [15].

2.2.1 Electronic structures of Zn-IV-N_2 materials

LDA and GGA methods are widely used for estimating the electronic structures of Zn-IV-N_2 compounds. The total energy properties of binding and structural parameters could be precisely obtained by using these approximations [55]. However, the value of band gap calculated from these two methods is usually smaller than the one obtained from experiments. The origin of this kind of underestimation is that LDA and GGA methods are basically valid for the properties of ground state such as lattice constants etc. and can not be effectively applied for the calculation of excited-state properties. Then, in order to predict and calculate the excited-state properties including band gaps and quasiparticle excitation more accurately, other new DFT methods should be introduced. And the quasi-particle self-consistent GW (QSGW) method [8] and the hybrid GGA with HSE functional [64] are regarded as the better approximations for predicting properties of ground-states as well as band gaps [12],[15].

Figure 2.3 (a) demonstrates the band structures of Zn-IV-N_2 materials calculated by LDA and QSGW methods. The LDA calculated band gaps of $ZnSiN_2$, $ZnGeN_2$ and $ZnSnN_2$ obtained by LDA are 3.6eV, 1.66eV and 0.55eV respectively. In comparison, the band gaps of $ZnSiN_2$, $ZnGeN_2$ and $ZnSnN_2$ simulated by QSGW approaches have increased up to 6.01eV, 3.6eV and 2.64eV, which are closer to the experimental results. In terms of the elements' orbital energy level, Zn-3d and N-2s energy levels have dramatic downward shifts to the top of the valence

band. For example, the position of Zn-3d of $ZnSnN_2$ presented by QSGW method is 1.5eV lower than the position of Zn-3d in LDA method. Also, from this figure, we can find that $ZnGeN_2$ and $ZnSnN_2$ are direct band gap materials while $ZnSiN_2$ is indirect band gap material by determining whether the valence band maximum (VBM) is at Γ or not [8],[11]. The band structure of $ZnSnN_2$ calculated based on HSE funtionals is shown in Figure 2.3(b). The band gaps are 1.82eV and 1.42eV respectively according to the different mixing parameters, which are comparable to the recent optical measured data [12].

The density of states of Zn-IV-N_2 materials has been indicated in Figure 2.4. In the valence bands, there are three regions. First, N-2s-like bonding contributes to the main density of states in the lower valence band around -15eV. Second, N-2p orbital is dominant in the range from VBM (0 eV) to -5eV. Third, the overlapping between Zn-3d orbital and N-2p orbital has a great impact on the distribution of density of states in the range from -5eV to -10eV. In addition, group IV cations' orbitals construct the conduction bands with the slight contributions from Zn-s orbital, N-s orbital or N-p orbital [8],[15].
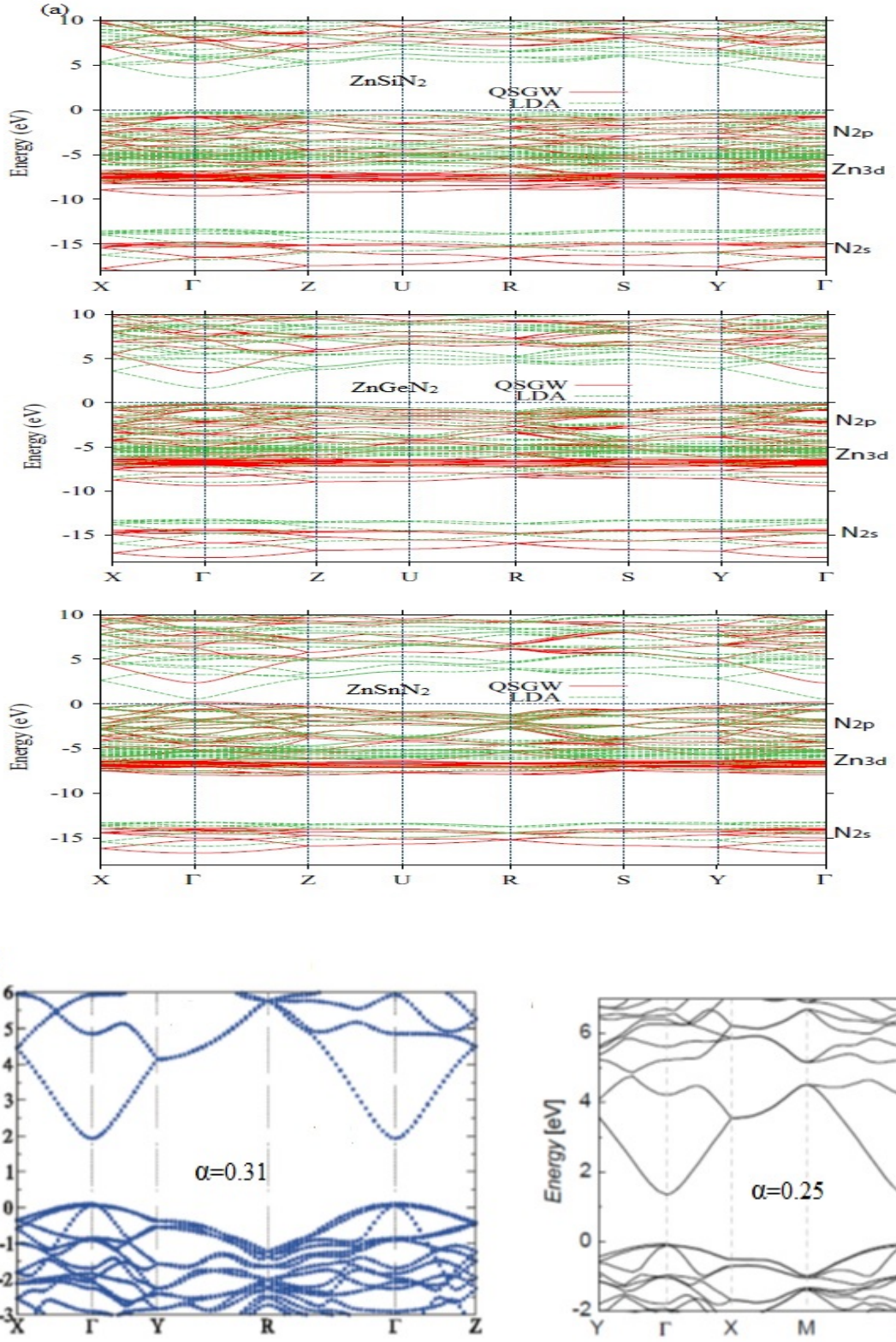
Figure 2.3 (a) Band structures of Zn-IV-N2 materials calculated by the QSGW approximation (Adapted from [8] with the permission of American Physical Society) (b) Band structure of $ZnSnN_2$ compound

24

calculated base on HSE funtionals with different mixing parameter α (Adapted from [12],[15] with the permission of John Wiley and Sons Publisher)
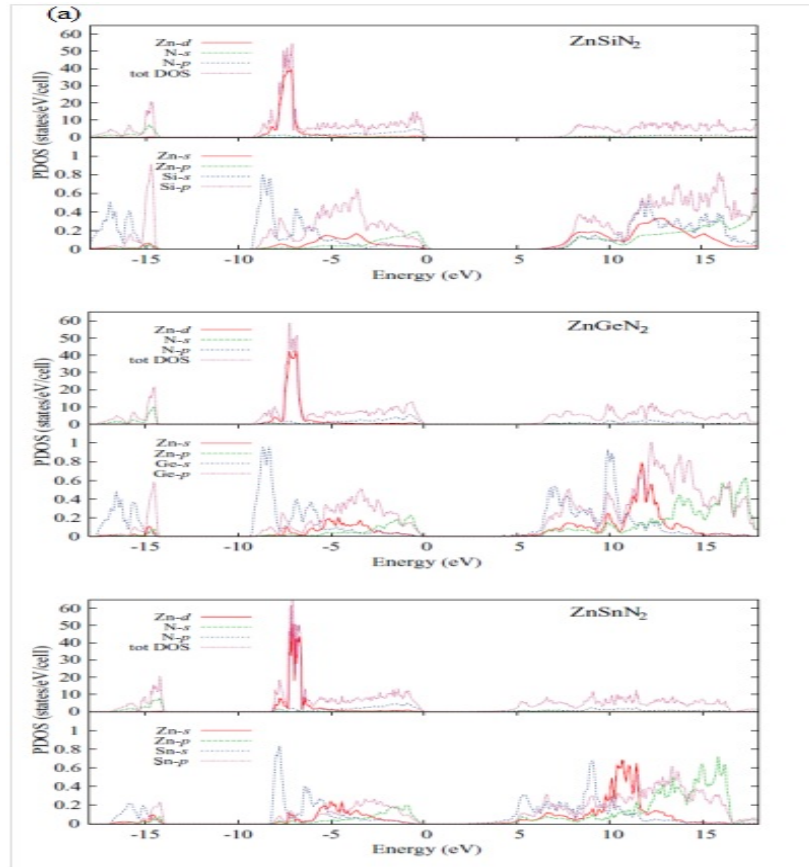
Figure 2.4 Density of states of Zn-IV-N_2 materials calculated by the QSGW approximation (Adapted from [8] with the permission of American Physical Society)

Table 2.1 summarized the band gaps, conduction band mass and valence band mass calculated based on LDA, QSGW and HSE functional. These results are from Ref.[8], [11], [12], [15].

Table 2.1 Summary of band gap, conduction band mass m_c and valence band mass m_v calculated by LDA, QSGW and Hyper-GGA(HSE) methods

	Band gap(eV)	Conduction band mass m_c	Valence band mass m_v
$ZnSiN_2$	3.6(LDA), 6,91(QSGW)	0.293(QSGW)	0.52(QSGW)
$ZnGeN_2$	1.66(LDA,)3.99(QSGW)	0.185(QSGW)	0.53(QSGW)
$ZnSnN_2$	0.55(LDA), 2.64(QSGW), 1.84 or 1.42(HSE)	0.141(QSGW), 0.13(HSE)	0.392(QSGW)

2.2.2 Phonon related properties of Zn-IV-N_2 materials

By using LDA and density-functional perturbation theory (DFPT) [65],[66], W.R.L. Lambrecht et al. have calculated the phonon vibrational modes of Zn-IV-N_2 materials at the Γ point(zone center). And they point out that this kind of materials belongs to the C_{2v} group according to the symmetry theory [59],[60],[61],[62]. Table 2.2 includes main vibrational modes of Zn-IV-N_2 compounds and these data are adapted from [11],[59],[60],[62].

Phonon densities of states are very useful for indicating many thermodynamic properties including the vibrational specific heat as well as entropy. In addition, the Raman spectra can also be explained from the density of phonon states. Figure 2.4 demonstrates the phonon band structure and total density of phonon states of Zn-IV-N_2 materials. From this figure, one can figure out the fact that there are obvious differences in the phonon distributions of $ZnSiN_2$, $ZnSnN_2$ and $ZnGeN_2$. Both $ZnSnN_2$ and $ZnGeN_2$ have four main branches over the whole frequency region. There are gaps among the branches in $ZnSnN_2$, while in $ZnGeN_2$, the two middle bands just connect with each other. In terms of $ZnSiN_2$, a broad band with the

26

combination with acoustic and optical phonon ranges has been found. For more details, please refer to [62].

Table 2.2 Phonon vibrational modes of Zn-IV-N_2 compounds

		Vibrational modes					
	a_2	b_{1T}	b_{1L}	b_{2T}	b_{2L}	a_{1T}	a_{1L}
	139	164	165	147	148	135	135
	154	178	178	169	169	168	169
	181	258	279	224	241	242	266
	300	399	403	357	358	287	287
ZnSiN$_2$	350	493	501	422	423	443	443
From[60]	422	507	509	466	471	456	456
	522	583	584	538	597	506	528
	538	630	634	625	648	584	586
	569	656	713	697	697	624	702
	678	784	812	776	784	766	766
	802	819	903	856	921	818	923
	831						
	109	134	135	107	107	108	108
	127	153	153	131	131	124	124
	130	178	180	155	159	146	147
	153	203	211	191	191	163	167
ZnSnN$_2$	185	224	224	237	238	206	206
From [62]	235	368	401	355	355	344	359
	338	429	435	370	440	359	389
	424	516	539	496	525	527	477
	483	541	579	560	562	528	554
	543	673	708	675	692	666	666
	668	713	720	700	739	677	716
	713						

	130	167	168	129	129	133	133
	163	194	194	166	166	168	168
	183	238	239	208	210	192	192
ZnGeN$_2$	201	308	310	266	266	224	227
From [59]	266	324	324	340	340	300	301
	341	512	538	482	491	483	484
	471	550	557	506	561	485	527
	555	598	651	600	628	586	623
	568	652	702	673	673	623	668
	654	767	794	775	790	760	763
	754	815	823	791	860	764	825
	820						
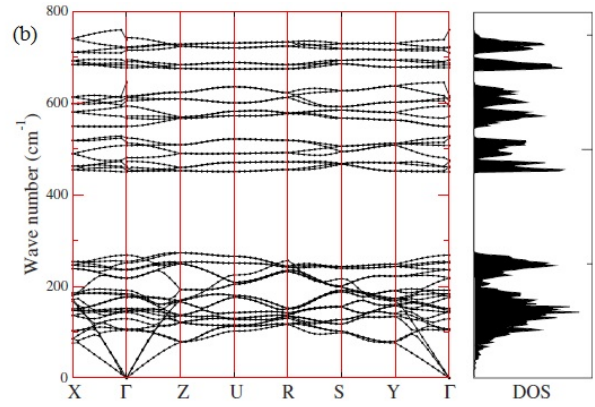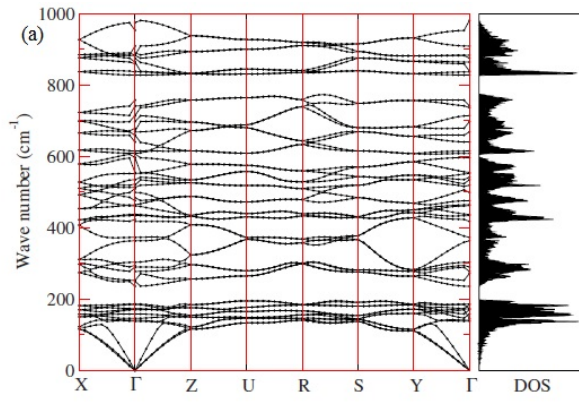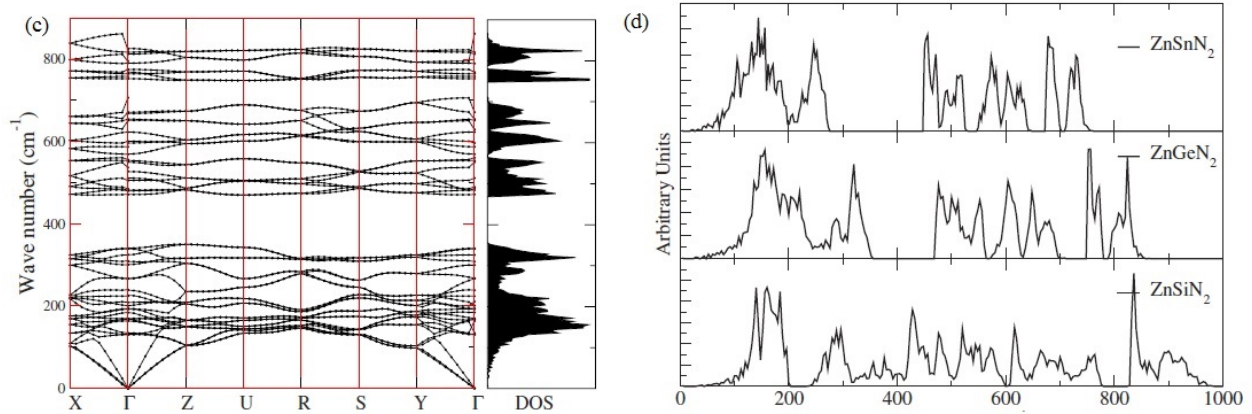
Figure 2.5 Phonon dispersions in (a) $ZnSiN_2$ (b) $ZnSnN_2$ (c) $ZnGeN_2$ and (d) Total density of state in Zn-IV-N_2 compounds (Reprinted from [62] with the permission of American Physical Society)

Raman spectroscopy is widely applied for the study of the phonon's properties. A.Punya et al. has compared the experimental Raman spectrum of a needle-like single crystal $ZnGeN_2$ and the spectrum of a polycrystalline $ZnGeN_2$ with sub-micron-size grain. There are significant differences in these two spectra. On one hand, they point out that the Raman spectrum of the polycrystalline one is similar to a phonon density of states. One kind of possible reason explained by them is that the small grain or the other serious disorder breaks the crystalline symmetry. By incorporating the second harmonics into the spectrum, the calculated phonon density of states of $ZnGeN_2$ can match with the experimental Raman spectrum. On the other hand, in the spectrum of the single crystal $ZnGeN_2$, the q=0 allowed modes can be distinguished easily. And the appearance of sharp peaks in the spectrum indicates the high crystalline property and estimates the existence of ordered cations [11],[63]. Figure 2.5 shows the comparison of Raman spectrum and phonon density of states of $ZnGeN_2$ with different crystal sizes.

29
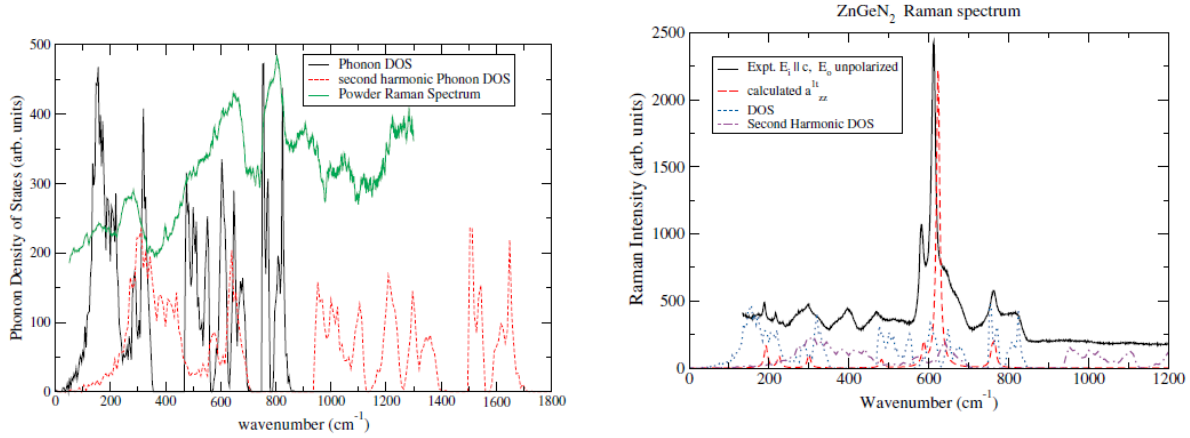
Figure 2.6 Left: Comparison of powder Raman spectrum from [67] (solid curve) with calculated phonon density of states for ZnGeN2 (dashed). Right: Comparison of a needle single crystal Raman spectrum from [61] (solid black line) with zone-center-calculated Raman spectrum for a Raman tensor component (dashed line) and phonon density of states (dotted line) and its second harmonic (dash-dotted line) (Reprinted from [63] with the permission of of John Wiley and Sons Publisher)

2.2.3 Thermodynamic stability and defect physics of Zn-IV-N$_2$ materials

Until now, although the construction of the full ternary phase diagram of Zn-IV-N$_2$ materials is still in progress, some initial achievements have been achieved. A. Punya et al. obtain the formation energies (enthalpies) of Zn-IV-N$_2$ at zero pressure and temperature using full –potential linearized muffin-tin orbital (FP-LMTO) method [11],[56],[57],[63]. The formation energies for ZnSiN$_2$, ZnSnN$_2$ and ZnGeN$_2$ are -4.84 eV/f.u., -2.32 eV/f.u. and -2.43 eV/f.u. respectively. In contrast, the formation energies of ZnSnN$_2$ and ZnGeN$_2$ calculated by S.Y.Chen et al. are only -0.13eV/f.u. and -1.31 eV/f.u. based on the plane wave pseudo-potential method [15]. And the origin of different formation energies of ZnSnN$_2$ reported from these two research groups is still unknown. Chen et al. also present that the formation energy can be regarded as the total reaction energy of the following reaction,

$$Zn(hcp) + Sn(diamond) + N_2(gas) \rightarrow ZnSnN_2 \tag{2-8}$$
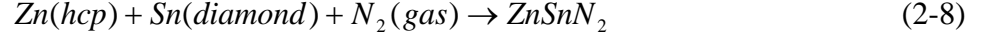
Here, Zn is in the hexagonal close packed (hcp) structure, Sn is in the diamond structure, and N_2 are gas molecules. In order to obtain the stable phase of $ZnSnN_2$ under the thermodynamic equilibrium as well as to eliminate the appearance of the secondary phase including the metal phases (Zn or Sn precipitation), binary compound Zn_3N_2 or Sn_3N_4, some rules should be obeyed. And these restrictions are listed as follows [11],[15]:

$$\begin{aligned}
\mu_{Sn} + \mu_{Zn} + 2\mu_N &= \Delta H_f(ZnSnN_2) \\
3\mu_{Zn} + 2\mu_N &\leq \Delta H_f(Zn_3N_2) \\
3\mu_{Sn} + 4\mu_N &\leq \Delta H_f(Sn_3N_4) \\
\mu_{Sn} \leq 0; \mu_N &\leq 0; \mu_{Zn} \leq 0
\end{aligned} \tag{2-9}$$

In addition, Chen et al. have compared the chemical potential diagram of $ZnSnN_2$ and $ZnGeN_2$ and point out that $ZnSnN_2$ has a much smaller formation energy and narrower stable regions compared with $ZnGeN_2$. Figure 2.6(a) and (b) show the calculated chemical potential regions for the stability of single-phase $ZnSnN_2$ and $ZnGeN_2$ [15]. Table 2.3 summarizes the formation energies of Zn-IV-N_2 compounds calculated by LDA, GGA and Hyper-GGA approaches(adapted data from [15],[63]).

Table 2.3 Formation energy (eV/per formula unit) of Zn-IV-N_2 compounds calculated by LDA, GGA and Hyper-GGA approaches

	LDA	GGA	Hyper-GGA(HSE functional)
$ZnSiN_2$	-4.68	-4.84	
$ZnGeN_2$	-1.98	-2.43	-1.32
$ZnSnN_2$	-1.68	-2.32	-0.13
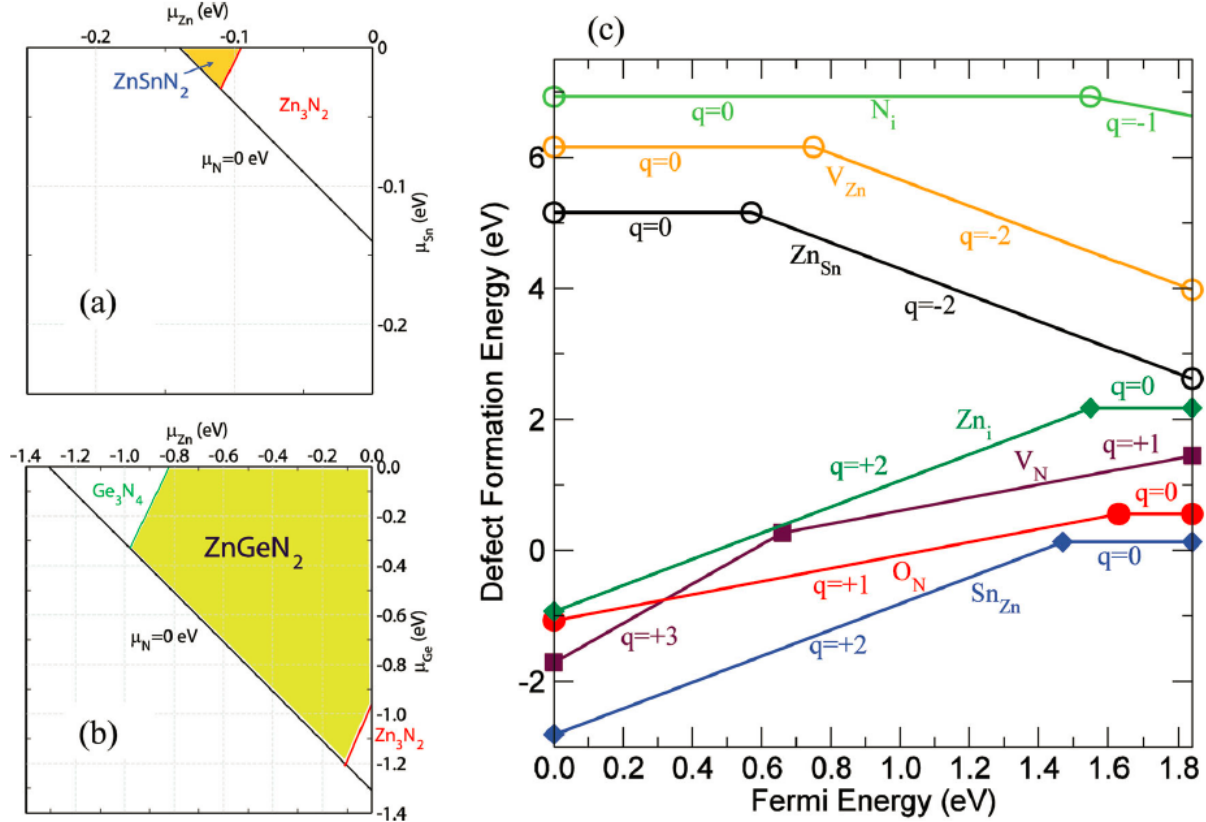
Figure 2.7 The calculated chemical potential regions of stable single-phase (a) $ZnSnN_2$ and (b) $ZnGeN_2$ (c) The change of the defect formation energy as a function of the Fermi energy when $\mu_{Zn} = -0.11eV; \mu_{Sn} = -0.02eV; \mu_N = -0.02eV$ (Reprinted from [15] with the permission of John Wiley and Sons Publisher)

There are few reports about the defect physics of Zn-IV-N_2 materials. W.R.L. Lambrecht et al. speculate that p-type doping is more easily realized in Zn-IV-N_2 compounds than the one in GaN. And group-I elements including Cu, Li and Na and group-III elements such as In, Ga, and Al are two kinds of promising candidates as the p-type dopants in Zn-IV-N_2 compounds. However, it is still unknown that the point defects created by these extrinsic dopants are deep level defects or shallow level defects [11]. Recently, S.Y. Chen et al. have calculated the formation energies of possible point defects in $ZnSnN_2$ [15]. They indicate that the formation energies of the donor defects such as Sn_{Zn}, V_N or Zn_i are significantly lower than those of

acceptor defects including Zn_{Sn}, V_{Zn} and N_i, which means $ZnSnN_2$ is a kind of intrinsic n-type material. And it is very difficult to do the p-type doping in $ZnSnN_2$ compounds from the perspective of thermodynamic analysis. In addition, they also point out that Sn_{Zn} antisite defect owns the lowest formation energy about 0.13eV among all the possible point defects, and the energy level of this point defect is 0.37eV below the conduction band maximum (CBM). Figure 2.6(c) presents the change of the defect formation energy as a function of the Fermi energy for the $ZnSnN_2$ compound [15].

2.3 Calculated materials' properties of Zinc tin nitride by DFT method

In this section, the materials' properties such as crystal structure, band gap and density of states of $ZnSnN_2$ have been calculated based on our theoretical methods. The calculated results have been discussed. The future work of our DFT calculation is also proposed.

2.3.1 Computational method

The structure relaxation is performed via Vienna Ab initio simulation package (VASP) [68] with the projector-augmented wave (PAW) method using the Perdew-Becke-Ernzerhof (PBE) generalized gradient approximation for the exchange-correlation (xc) functional. In this implementation, projector augmented–wave (PAW) pseudo-potentials [69] are applied for treating the core electrons. The calculations are carried out with a energy cutoff of 600 eV for the plane-wave basis set. The Brillouin zone integration of orthorhombic structure is sampled by a 6×6×6 Monkhorst-Pack k-point mesh [70] in the 16-atom primitive cell. Each atom in the

primitive cell is fully relaxed with force convergence threshold of 0.01eV/Å. After relaxation, a k-point mesh of 4×4×4 is used to perform density of states calculation utilizing the non-local hybrid functional (HSE) with a mixing parameter α of 0.3, which is the percentage of the semi-local GGA exchange potential replaced by the screened Fock exchange.

2.3.2 Results and discussion

Stoichiometric zinc tin nitride belongs to the space group P$na2_1$ (this space-group denomination is in the International Tables of Crystallography) with the space No. 33 (symmetry group C_{2v}). It has an orthorhombic structure. Our DFT calculation is carried out based on the beta-$NaFO_2$ structure, which is the prototype of the crystal structure for Zn-IV-N_2 compounds [11], with the symmetry preserved. The primitive cell of $ZnSnN_2$ is composed of 16 atoms (4 Sn atoms, 4 Zn atoms and 8 N atoms) in an orthorhombic unit cell. The calculated lattice parameters (a, b, c) of this cell are 5.91 Å, 5.54 Å and 6.81 Å respectively. Table 2.4 shows the calculated and experimental lattice constants from our work and other literatures. And the crystal structure of $ZnSnN_2$ is shown in the Figure 2.7. The internal positions of atoms in this primitive cell are listed in Table 2.5.

We present the calculated band structure of $ZnSnN_2$ using PBE-GGA functional in Figure 2.8. And the figure shows that both the valence band maximum (VBM) and the conduction band minimum (CBM) are located at Γ point, which indicates that $ZnSnN_2$ is a kind of direct band gap material. In addition, it also demonstrates that the shape of the conduction band near the minimum is closer to a conicalness shape rather than parabola shape, which is consistent with the result calculated by T.R.Paudel [29]. One of possible reasons is that $ZnSnN_2$ has a very small conduction effective mass. And the conduction band mass of $ZnSnN_2$ is estimated to be only about 0.14 m_0 or 0.13 m_0 [8],[11],[12]. The band gap obtained from this band structure is

about/around 0.1eV, which is similar to the value reported by T.R.Paudel in Ref.[29]. T.R.Paudel calculated the band gap of $ZnSnN_2$ to be 0.07eV using local density approximation (LDA) with the FP-LMTO method. However, the band gaps estimated by PBE-GGA from our work as well as LDA approach do not agree with those measured by experiments. S.Y.Chen et al. reported the band gap of polycrystalline $ZnSnN_2$ to be about 2 eV [12]. Quayle et al. determine the band gap of $ZnSnN_2$ to be 1.7eV using photoluminescence excitation spectroscopy (PLE). In our work, the band gap is extracted from the optical transmission data to be 1.6eV—1.9eV according to different samples. This significant underestimation of band gaps from LDA and PBE-GGA is due primarily to the fact that these two methods are basically valid for the properties of ground state and cannot be effectively used for the computation of excited-state properties. In Section 2.2.1, readers can find more details. In addition, GGA also reproduces slightly larger lattice parameters, which is confirmed by our work shown in Table 2.4. And then, a smaller band gap will be generated [11].

In order to reproduce the correct band gap in line with experimental measurements, we utilize the non-local hybrid functional (HSE) including partial exact exchange following Chen et al. [12],[15], which gives rise to a band gap of about 2.0 eV. The total and decomposed density states of different orbitals and elements in $ZnSnN_2$ structure have been shown in Figure 2.9 and Figure 2.10. In the valence bands, there are three main regions. First, N-2s-like bonding with Zn and Sn contributes mainly to the density of states in the lower valence band around -15eV. Second, the N-2p orbital is dominant in the range from VBM (0 eV) to -5eV. Third, the overlap between Zn-3d orbitals and N-2p orbitals has a great impact on the distribution of density of states in the range from -5eV to -10eV. A very sharp peak of the Zn-3d orbital is found near the N-2p broad peak. In addition, we find that DOS in the region near the valence band maximum

35

(VBM) is mainly determined by N-2p orbitals as well as Zn-3d orbitals with a slight contribution of Sn orbitals. And N-2s orbitals, N-2p orbitals and Sn orbitals contribute to the DOS in the region near the conduction band minimum (CBM). This result is consistent with the ones reported by reference [8] and reference [15]. In addition, the position of Zn-3d peak is around -6.8eV, which is close to the one calculated by QSGW method and lower than that obtained by LDA approach [8].

Table 2.4 Calculated and experimental lattice parameters a, b and c of $ZnSnN_2$

Structure	Lattice constants	Our computed result	Our experimental result	Other theoretical results	Other experimental results
Pna2$_1$	a	6.81	6.75	6.721[a], 6.76[b]	6.753[c]
	b	5.91	5.86	5.842[a], 5.85[b]	5.842[c]
	c	5.54	5.53	5.459[a], 5.58[b]	5.462[c]

[a] From [12]

[b] From[62]

[c] From[19]
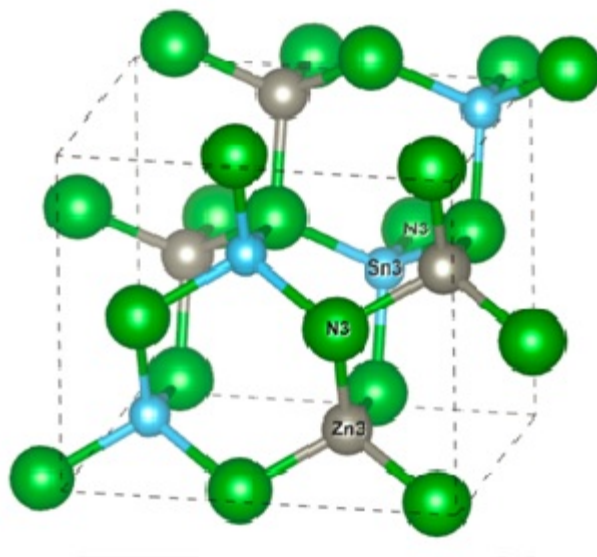
Figure 2.8 Crystal structure of stoichiometric ZnSnN$_2$: grey spheres represent zinc atoms, blue spheres represent tin atoms and green spheres represent nitrogen atoms

Table 2.5 Internal atom positions in the primitive cell with 16 atoms

	Atom	x	y	z
ZnSnN$_2$	Sn	0.0872	0.0018	0.1249
		0.9127	0.5018	0.8751
		0.5872	0.0018	0.3751
		0.4128	0.5018	0.6249
	Zn	0.4171	0.5021	0.1249
		0.5829	0.0021	0.8750
		0.9171	0.5021	0.3750
		0.0083	0.0021	0.6249
	N$_{Sn}$ or N$_{Zn}$	0.083	0.6225	0.1261
		0.9173	0.1225	0.8738
		0.5827	0.6225	0.3738
		0.4173	0.122	0.6261
		0.4197	0.1275	0.1238
		0.5803	0.6275	0.8761
		0.9197	0.1275	0.3761
		0.0829	0.6275	0.6238
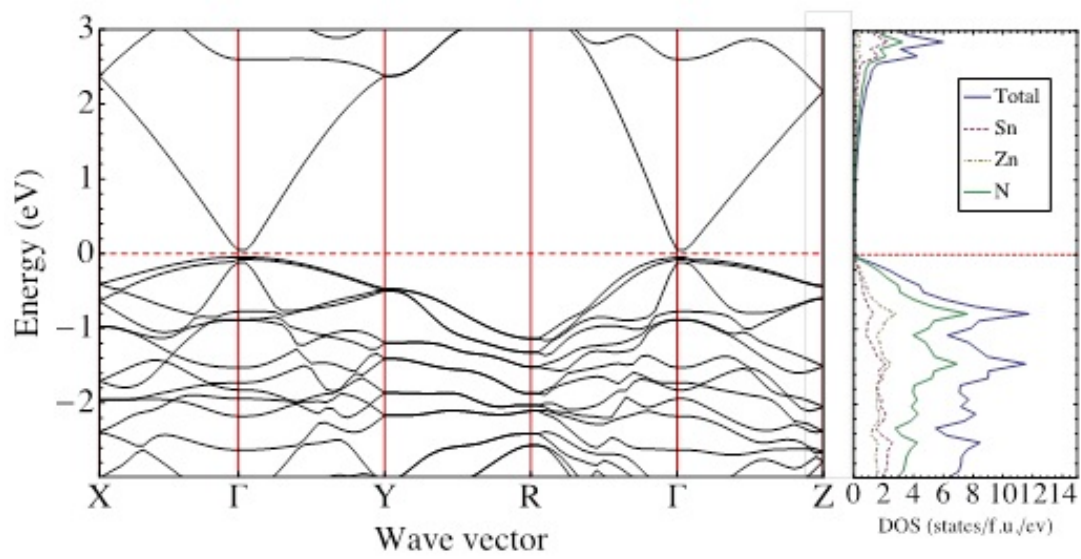
Figure 2.9 Band structure of ZnSnN$_2$ calculated by the PBE-GGA method
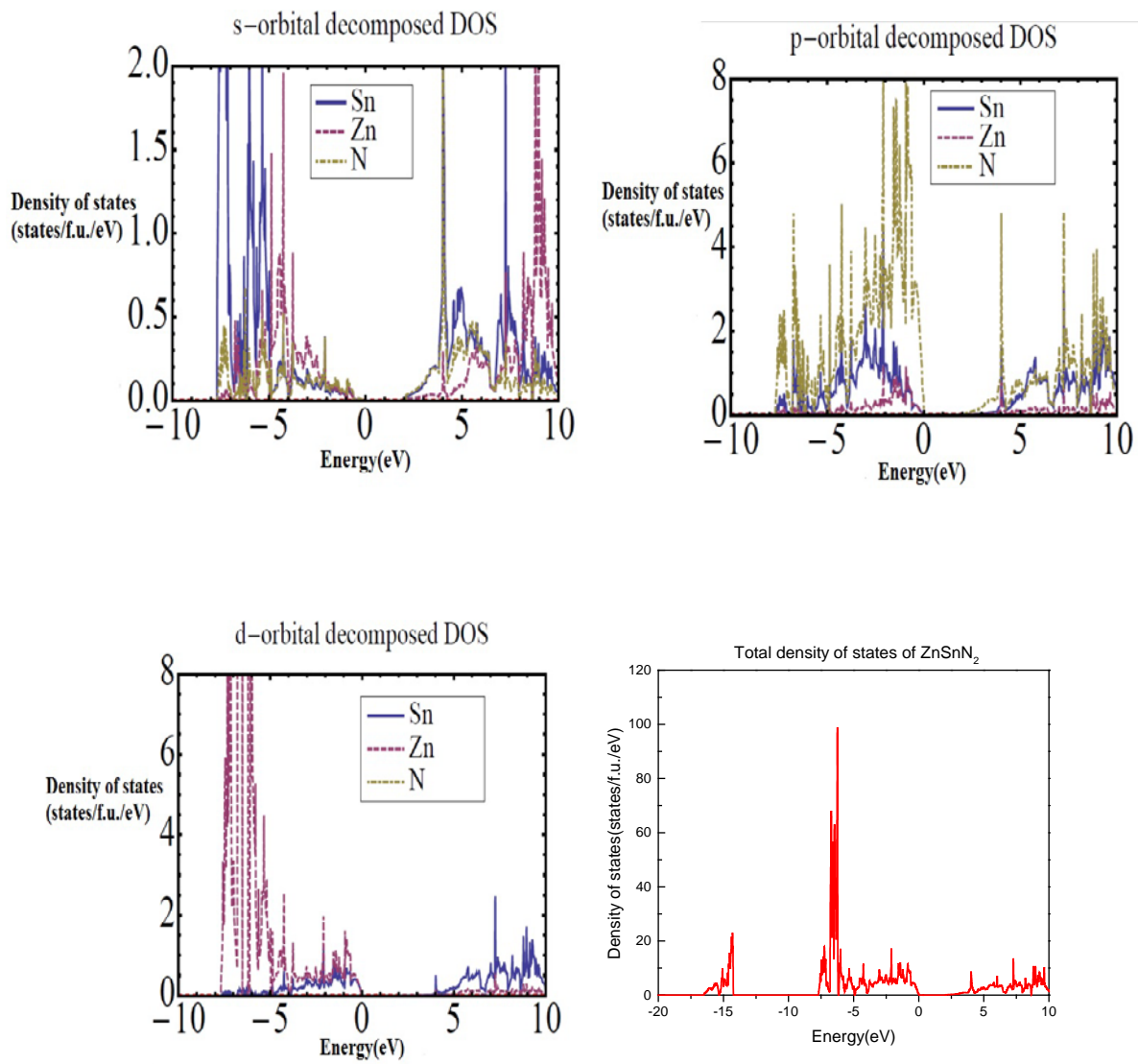
Figure 2.10 Upper left: s-orbital decomposed density of states, upper right: p-orbital decomposed density of states, and bottom left: d-orbital decomposed density of states, bottom right: total density of state.
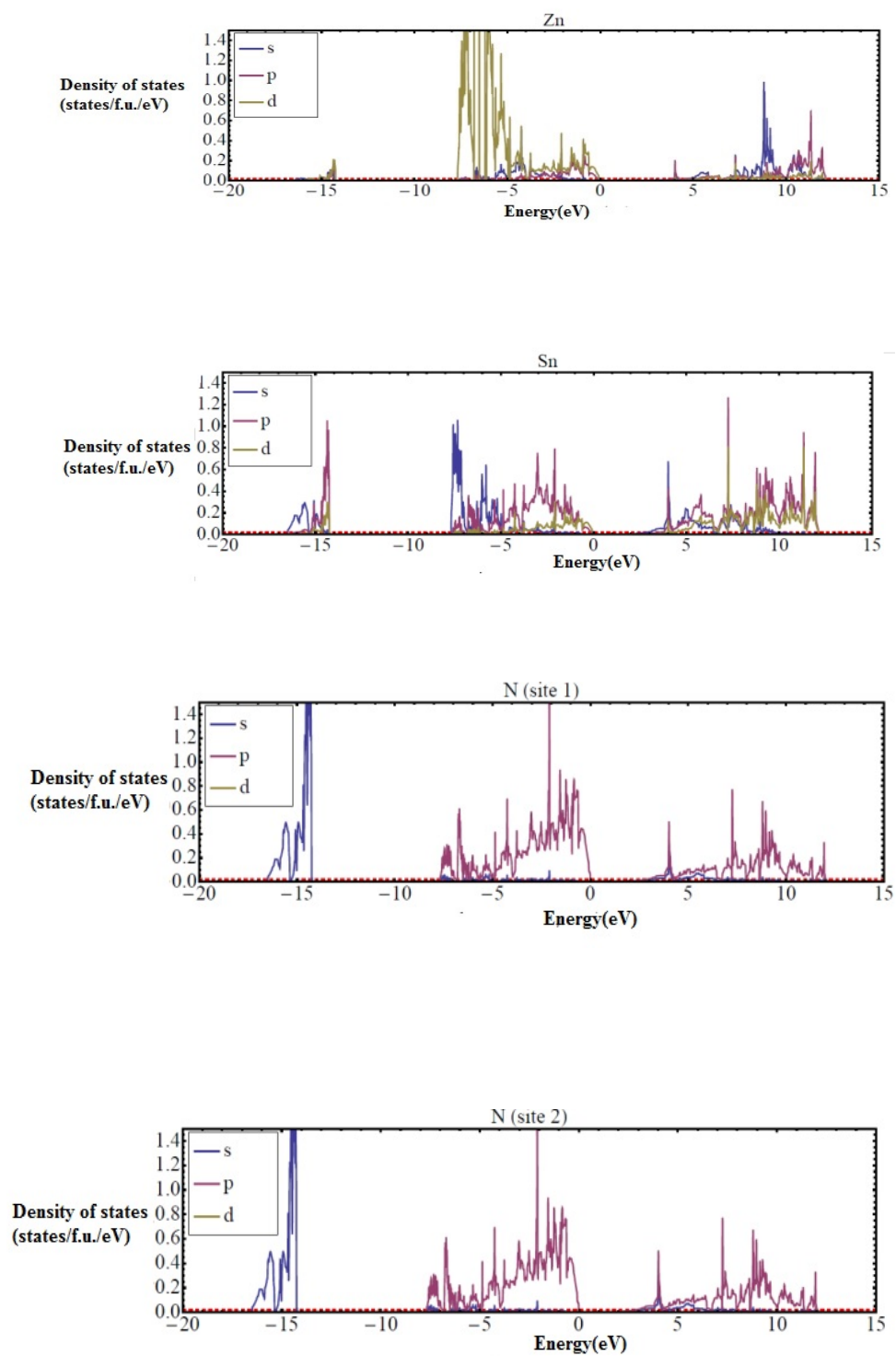
Figure 2.11 Decomposed density of states of different elements in ZnSnN$_2$, from top to bottom: Zn, Sn, N1, N2.

2.3.3 Conclusion and outlook

In conclusion, we have presented a first-principles calculation of the crystal structure, lattice parameters, atomic positions, band structure and density of states of $ZnSnN_2$. The calculated lattice constants a, b and c are comparable to our experimental results as well as previous calculations. In terms of the band structure, we find that the band gap obtained by PBE-GGA is underestimated significantly compared with experimental data from our work and reported by other groups. This is because the GGA method, intrinsically, is not suitable for the estimation of the excited-state properties such as the band gap. In addition, based on the careful analysis of the total and decomposed density of states of $ZnSnN_2$, we can predict that DOS of the valence band can be separated into 3 regions, namely, the N-2s orbital contributes to the DOS in the range around -15eV, the N-2p orbital dominates the range from 0 to -5eV and hybridization between Zn-3d orbitals and N-2p orbitals construct the distribution of DOS in the range from -5eV to -10eV.

In the future study, first, we need to recalculate the band structure using HSE hybrid functional in order to accurately extract effective masses for both VBM and CBM. In addition, from the density of states of phonon, many kinds of thermal properties such as vibrational specific heat and entropy can be extracted. Therefore, for the next step, we will focus on the calculation of the phonon dispersions and density of states based on our computed crystal structure of $ZnSnN_2$. Also, we will try to explain our Raman and infrared spectra from experiments, using the calculated vibration modes. Finally, although W.R.L.Lambrecht et al. speculate the possibility of p-type doping in $ZnSnN_2$ [11], there is no report about this topic. Then, we will try to choose different group-I elements such as Cu, Na and Li and group-III

elements such as Ga, Al, In as extrinsic dopants and calculate the formation energy of the point defects created by those dopants.

.

Chapter 3 Preparation, characterization and device applications of zinc tin nitride thin film materials

This chapter describes the preparation, characterization, and related device applications of zinc tin nitride thin films.

3.1 Preparation of zinc tin nitride thin films

In this study, polycrystalline $ZnSnN_2$ thin films were deposited on c-plane sapphire and (0001) GaN template substrates, using a reactive radio frequency (RF) magnetron sputtering system (ULVAC JSP 8000). A 4-inch diameter zinc tin alloy ($Zn_{0.75}Sn_{0.25}$, 99.995% purity, ACI alloy Inc.) was used as the sputtering target and the substrates were mounted on a rotating metal plate at a horizontal distance of 15cm from the target. The RF sputtering power was set to 300W, and the substrate temperature was adjusted from 275 ^{o}C up to 400 ^{o}C. The reactive sputtering gas is the mixture of pure N_2 and Ar with plasma activation. The base pressure of sputtering chamber was in the low range of 10^{-6} Torr (1.0×10^{-6} — 3.0×10^{-6} Torr). Prior to the films deposition, a pre-sputtering process was performed for 20 minutes with pure Ar gas atmosphere in order to clean the surface of target. The film thicknesses were obtained by Dektak profilometry after deposition.

3.2 Characterization of zinc tin nitride thin films

3.2.1 Crystal structure

Thin films' x-ray diffraction (XRD) measurements ($\theta - 2\theta$ geometry) were performed using a PANalytical X'Pert Pro x-ray powder diffractometer with a Cu Kα radiation source and a sealed proportional detector equipped with X'Pert highscore software. Grazing incident x-ray diffraction scans were taken with a Bede D1 diffractometer equipped with a Maxflux (TM) focusing graded x-ray mirror and a two bounce Si 220 channel-cut collimator crystal using CuKa1 radiation from a sealed x-ray tube. A small incident angle is used (1 degree) and the detector position ranges from 15-60 degrees in order to make the diffraction measurement more surface sensitive.

Figure 3.1 shows the simulated powder diffraction spectra for the $ZnSnN_2$ based on the orthorhombic crystal structure in the Pna2$_1$ space group (left figure) and the comparison between the measured xrd pattern obtained from the grazing incident angle scan (right figure). The films were grown under the condition of $N_2/(N_2+Ar)$ ratio of 50% and substrate temperature of 275˚C. The main characteristic peaks from the experimental data match with the ones in calculated pattern, which means the crystal structure of our $ZnSnN_2$ films is orthorhombic. The lattice parameters a,b, and c are listed in the Table 3.1 and calculated by the following equations[71]:

Bragg's equation: $$\lambda = 2d \sin \theta \qquad\qquad\qquad (3\text{-}1)$$

λ is the X-ray wavelength(here, the Cu Kα1 characteristic line is 1.54Å ; d is the lattice space distance; and θ is the diffraction angle.

Orthorhombic plane spacing: $$\frac{1}{d^2} = \frac{1}{a^2} + \frac{1}{b^2} + \frac{1}{c^2}$$ (3-2)

Table 3.1 Lattice space distance and lattice parameters calculated from measured xrd pattern

Peak position $2\theta(°)$	Miller index h k l	Space distance d (Å)	Lattice parameters		
			a(Å)	b(Å)	c(Å)
30.4536	120	2.9328			
32.4756	002	2.7547			
34.5657	121	2.5926	5.855 ± 0.0112	6.749 ± 0.0238	5.527 ± 0.0143
54.1137	320	1.6934			
59.3385	123	1.5561			
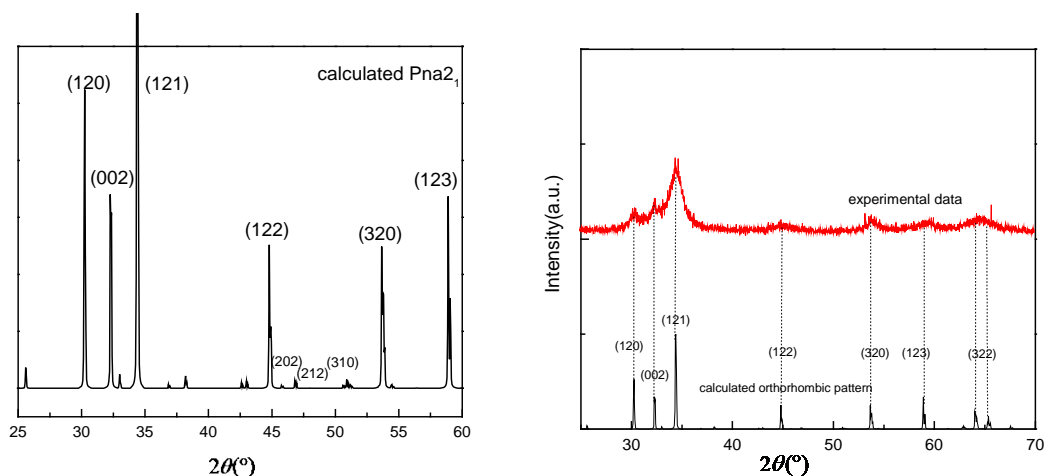
Figure 3.1 Left: Calculated xrd pattern for ZnSnN$_2$ Right: comparison between measured and calculated xrd pattern

Figure 3.2 shows the impact of substrate temperature on the crystal structure. These films were deposited on the c-plane sapphire substrates at the different substrate temperatures in the range between 275 ˚C and 400 ˚C with N$_2$/(N$_2$+Ar) ratio of 50%. With the increase of substrate temperatures, the values of full width half maximum (FWHM) of characteristic peaks decreased notably, suggesting the mean grain sizes become larger. In addition, this phenomenon also indicates that the crystallinity of the films improved significantly upon increasing the substrate temperatures. Additionally, we can find that a characteristic peak (*) from Zn$_3$N$_2$ phase (JCPDS #88-0618) became more and more obvious at the surface of films according to the spectra of grazing incident angle xrd.
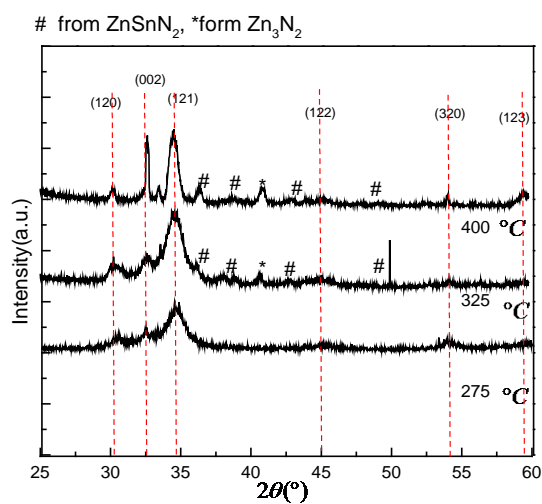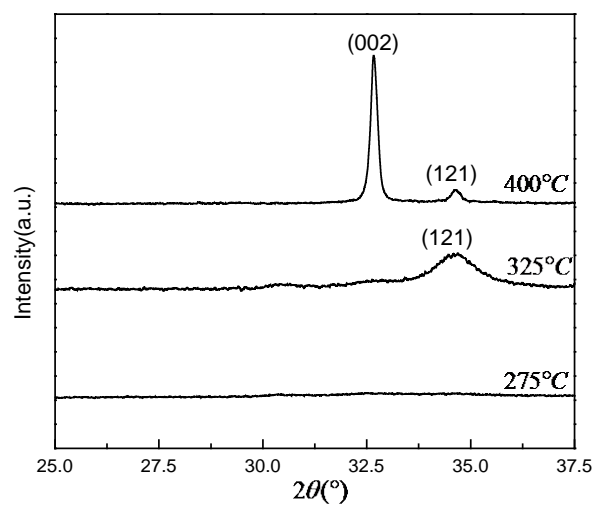
Figure 3.2 Upper: XRD patterns with a $\theta-2\theta$ configuration for as-deposited films with different substrate temperatures at a fixed $N_2/(N_2+Ar)$ ratio of 50%, Lower: XRD patterns with a $1°$ grazing incident angle configuration for as-deposited films with different substrate temperatures at a fixed $N_2/(N_2+Ar)$ ratio of 50% (# from $ZnSnN_2$ and * from Zn_3N_2)
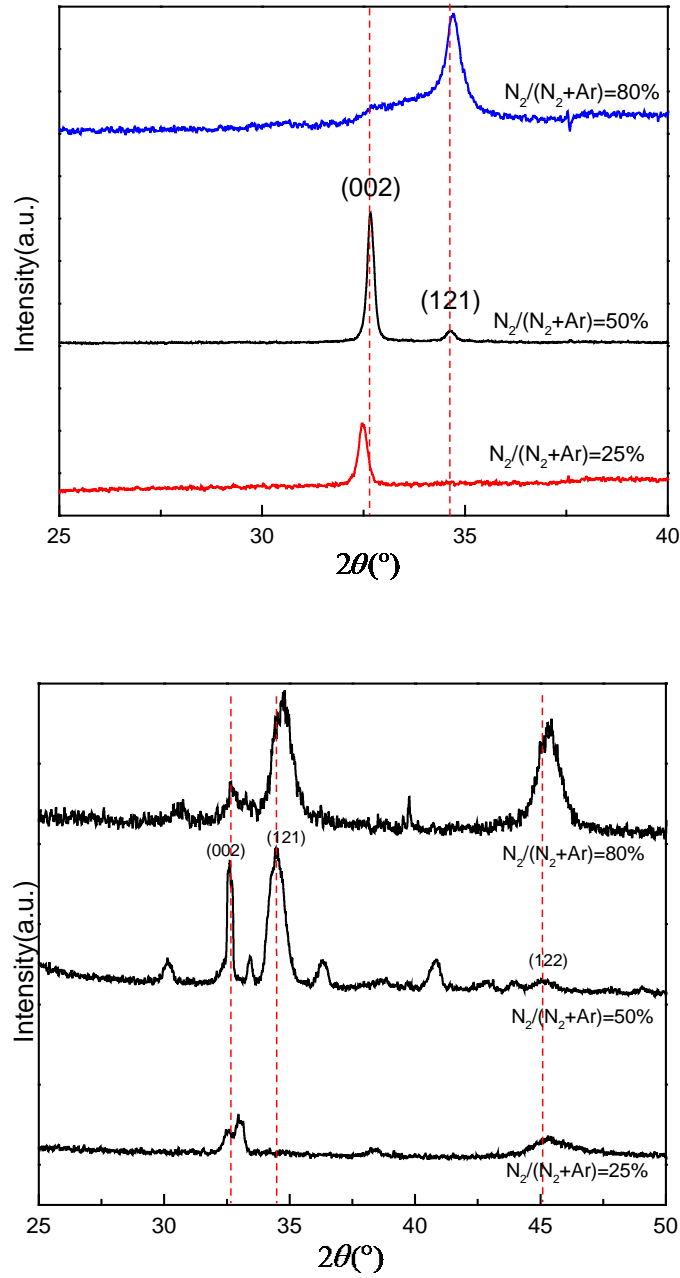
Figure 3.3 Upper: XRD patterns with a $\theta - 2\theta$ configuration for as-deposited films with various $N_2/(N_2+Ar)$ ratios at a substrate temperature of 400˚C, Lower: XRD patterns with a 1˚ grazing incident angle configuration for as-deposited films with various $N_2/(N_2+Ar)$ ratios at a substrate temperature of 400˚C

XRD patterns for films deposited at various $N_2/(N_2+Ar)$ ratios including 25%, 50% ,and

80%, are shown in Figure 3.3. With the increased incorporation of N_2 in the total reactive gas

mixture, the preferential orientation of crystal growth changed in these polycrystalline films. In the films with low and medium ratios of $N_2/(N_2+Ar)$, the (002) plane $ZnSnN_2$ peak dominates. However, in the films with high ratio of $N_2/(N_2+Ar)$, the peak related with (121) crystal plane is more obvious. Also, we note the point that when the N_2 content increases to 80% of the total sputtering gas mixture, the peak of (122) crystal plane is much sharper and more dominant at the surface of films from the grazing incident angle xrd scans. Table 3.2 summarizes the values of full width half maximum (FWHM) and average crystallite sizes of films of different $N_2/(N_2+Ar)$ ratios at a fixed substrate temperature of 400 ˚C. It is clear that the best crystalline quality is attained at the $N_2/(N_2+Ar)$ ratio of 50% with smallest value of FWHM and largest crystallite size. And the largest crystallite size is approximately 133nm, which is larger than other results reported until now[29],[72],[73], based on the peak of (002) plane using Scherrer's formula:

$$t = \frac{0.9\lambda}{B\cos\theta_B} \tag{3-3}$$

Here, λ is the x-ray wavelength, B is the full width half maximum (FWHM), θ is the Bragg angle, and t is the average crystallite size.

Table 3.2 The values of full width half maximum (FWHM) and average crystallite sizes of films of different $N_2/(N_2+Ar)$ ratios at a fixed substrate temperature of 400 ˚C

$N_2/(N_2+Ar)$	Peak position(˚)	Crystal plane(hkl)	FWHM(˚)	Average crystallite size(Å)
25%	32.458	(002)	0.232	511
	32.653	(002)	0.062	1335
50%	34.572	(121)	0.108	770
80%	34.677	(121)	0.181	460

3.2.2 Vibrational modes

The crystal point group of $ZnSnN_2$ is C_{2v}.The character table for this group is shown in Table 3.3. In this table, x, y, and z mean the transformations of the x, y, and z coordinates and R_x, R_y, and R_z indicate the rotation about the x, y, and z axes. The irreducible representations such as A_1, B_1 and B_2 correspond to the z, x, and y respectively. The A_2 irreducible representation is related to a xy matching function. The vibrational modes at Γ of $ZnSnN_2$ can be identified by character table [11],[74]. There are seventy-eight vibrational modes of all symmetries, including A_2, B_{1T}, B_{1L}, B_{2T}, B_{2L}, A_{1T}, and A_{1L} [11],[62]. Raman spectroscopy is useful for observing the molecular vibrations. In $ZnSnN_2$, all modes are Raman-active [62]. Table 2.2 lists the vibrational modes of $ZnSnN_2$.

Raman spectra of $ZnSnN_2$ thin films were acquired by a Renishaw inVia Confocal Raman system using a 633 nm wavelength line of an ionized argon laser and the laser power was 5mW. The diameter of focused spot size was around 1um.

Table 3.3 Character table for C_{2v} with the irreducible representations: first column, irreducible representations; first row, classes (Adapted from [74] with the copyright by Pearson Prentice Hall)

	E	C_2	$\sigma_v(xz)$	$\sigma_{v'}(yz)$		
A_1	1	1	1	1	z	$x^2+y^2+z^2$
A_2	1	1	-1	-1	R_z	xy
B_1	1	-1	1	-1	x, R_y	xz
B_2	1	-1	-1	1	y, R_x	yz

Figure 3.4 shows the comparison between the Raman spectrum of $ZnSnN_2$ thin films from our experiment and the calculated phonon density of states for $ZnSnN_2$ from ref.[62]. This experimental sample is grown on the c-plane sapphire substrates at the substrate temperature of 400 ˚C with $N_2/(N_2+Ar)$ ratio of 50%. The Raman spectrum of our sample is comparable to the total phonon density of states (DOS). The similar observations have been reported by Viennois et al. and Timothy J. Peshekfor et al. for the Raman spectra of polycrystalline $ZnGeN_2$ [61],[67]. A possible explanation for this observation is that small crystallite sizes disrupt the crystal symmetry, which will result in the DOS-like Raman spectra of polycrystalline films [11],[61]. In addition, due to the polycrystalline nature, our spectrum doesn't show any well-defined polarization dependence.

The calculated density of states from Ref [62] is mainly composed of three main regions, a folded acoustic branch between 100 cm^{-1} and 300 cm^{-1}, a lower optical branch between 430 cm^{-1} and 630 cm^{-1}, and an upper optical branch between 660 cm^{-1} and 760 cm^{-1}. In our

experiment, one peak at 237 cm^{-1} is found in the low frequency region, which can be assigned to the corresponding second peak in the folded acoustic branch of DOS. According to the literature, this characteristic peak originates from the vibration of Sn element [62]. However, the first calculated peak at around 150 cm^{-1} cannot be observed in our spectrum. A possible explaination is that it is a temperature-dependant peak. At higher substrate temperature (for example, 400°C), we cannot find this peak. On the other hand, this peak can be detected in the lower substrate temperature such as 275°C. In the medium frequency region from 430 cm^{-1} to 630 cm^{-1}, two main peaks are detected at 483 cm^{-1} and 572 cm^{-1}. In comparison, there are four peaks in this lower optical branch in the calculated DOS. This difference mainly resulted from the limit of resolution and peaks broadening. In addition, a combination of signals is observed in the frequency range from 300 cm^{-1} to 430 cm^{-1}, in which there is a gap of DOS. Background scattering as well as overtones from the experiments lead to this phenomenon. In the high frequency region, one peak at 683 cm^{-1} is measured. This peak can be related with the two splitting peaks in the upper optical region based on theoretical calculations. Again, the difference between experimental and theoretical calculation is still far from resolution. In ZnSnN$_2$, the optical modes are mainly determined by the motion of N atoms because N has a much smaller atomic mass than Zn and Sn. Meanwhile, due to an existence of bimodal distribution in bond lengths, namely short Sn-N and long Zn-N stretching, the force constants between Zn-N stretching and Sn-N stretching are significantly different. So, Zn-N bonds with small force constants are estimated to result in the lower optical modes. In contrast, Sn-N bonds with large force constants can be correlated with higher optical modes. Here, we assign the peak of 683 cm^{-1} to Sn-N bonds. The peak of 572 cm^{-1} corresponds to Zn-N bonds [59],[62]. Finally, we point

out that the underlying overtones play an important role in causing the tendency of higher intensity appearing at higher frequency in our experiment.

The Raman spectra of $ZnSnN_2$ thin films with different substrate temperatures at a fixed $N_2/(N_2+Ar)$ ratio of 50%, c-plane sapphire substrate, and (0001) GaN substrate are shown in Figure 3.5. With the temperature increase from 275 ˚C to 400 ˚C, two characteristic peaks related to Zn-N and Sn-N bonds become more obvious. Also, the FWHM of these two peaks are sharper, which indicates the crystallinity of films improved from the increase of the substrate temperature. And this result is consistent with the XRD analysis. In addition, the peak position of Sn-N stretching shifted from 674 cm^{-1} to 683 cm^{-1} with an increase in the substrate temperature. Main peaks in the spectrum of c-plane sapphire substrate are 373 cm^{-1}, 416 cm^{-1}, 444 cm^{-1}, 575 cm^{-1} and 745 cm^{-1}. In the Raman spectrum of (0001) GaN substrate, peaks at 569 cm^{-1}, 661 cm^{-1}, and 141 cm^{-1} are obtained. The first peak at 150 cm^{-1} in the acoustic branch of DOS is detected in our experiment at the substrate temperature of 275 ˚C, suggesting the appearance of the peak dependant on the substrate temperature.

The impacts of various $N_2/(N_2+Ar)$ ratios on the vibrational modes of $ZnSnN_2$ thin films are described in Figure 3.6. The relative intensity ratio of I_{Zn-N}/ I_{Sn-N} decreased with an increase in the $N_2/(N_2+Ar)$ ratio, suggesting that the number of Zn-N bonds decreases and the number of Sn-N bonds increases in $ZnSnN_2$ films. This is confirmed by the compositional analysis through XPS and EDX. This trend is observed at the substrate temperatures of 400 ˚C and 275 ˚C, indicating non-temperature dependence of peak detectability. In addition, we find that the peak of 237 cm^{-1} in the folded acoustic region splits into two peaks (233 cm^{-1} and 255 cm^{-1}) in $ZnSnN_2$ films prepared at the substrate temperature of 400 ˚C with the $N_2/(N_2+Ar)$ ratio of 25%.

The reason for this kind of peak splitting is still unclear. Also, it is worth noting that the peak at 156 cm^{-1} in the low frequency region will become more obvious with the decreased incorporation of N$_2$. The origin of this characteristic peak is not clear. Additionally, the peak at 233 cm^{-1}, corresponding to the vibration of Sn atoms, was much broader with the decrease of N$_2$/(N$_2$+Ar) ratios at the substrate temperature of 275 ˚C.

Figure 3.7 compares the Raman spectrum of ZnSnN$_2$ films grown on the c-plane sapphire substrate with the one of ZnSnN$_2$ films grown on (0001) GaN substrate. The main peaks observed in these two spectra are almost the same except for the appearance of GaN substrate's peaks in the upper spectrum.
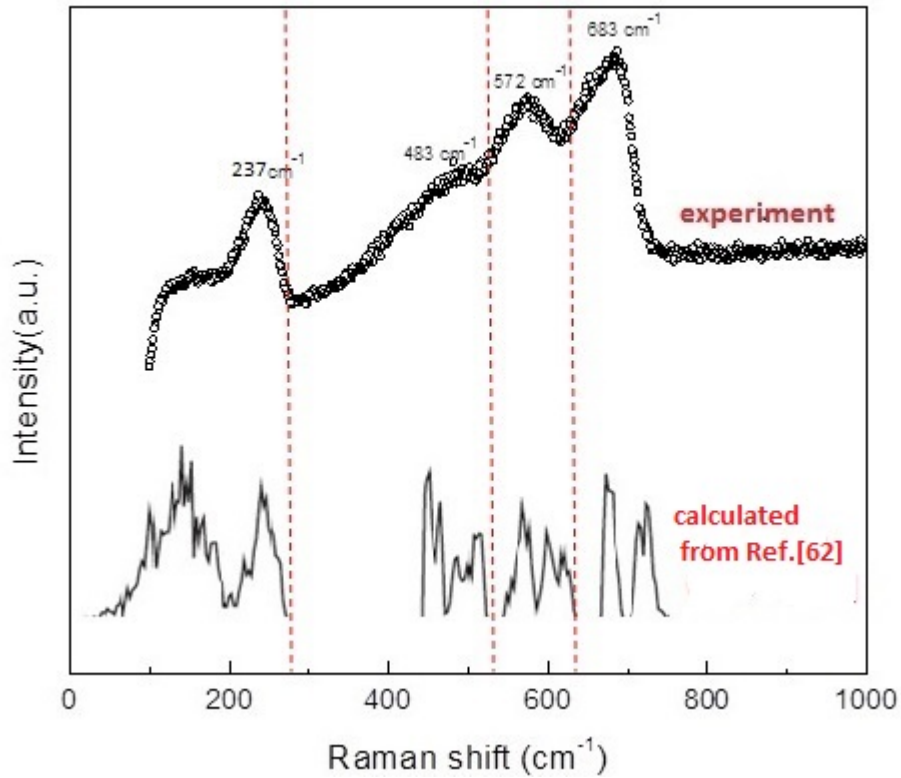
Figure 3.4 Comparison of the Raman spectrum of polycrystalline ZnSnN$_2$ thin films from our experiment with calculated phonon density of states for ZnSnN$_2$, from T.R. Paudel et al. [62]
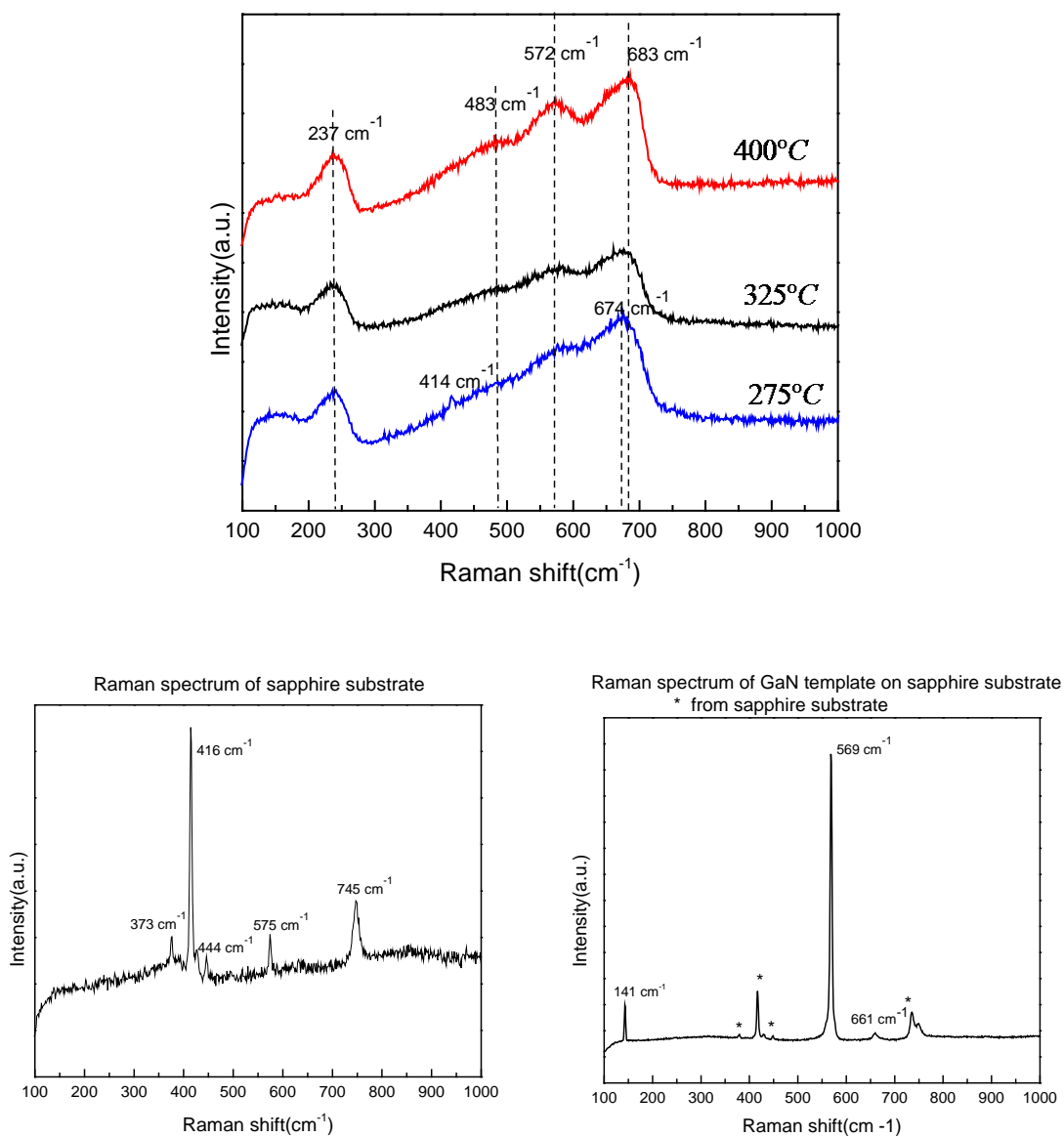
Figure 3.5 Upper: Raman spectrum of ZnSnN$_2$ thin films with various substrate temperatures at a fixed N$_2$/(N$_2$+Ar) ratio of 50%; Lower left: Raman spectrum of c-plane sapphire substrate; Lower right: Raman spectrum of c-plane(0001) GaN substrate
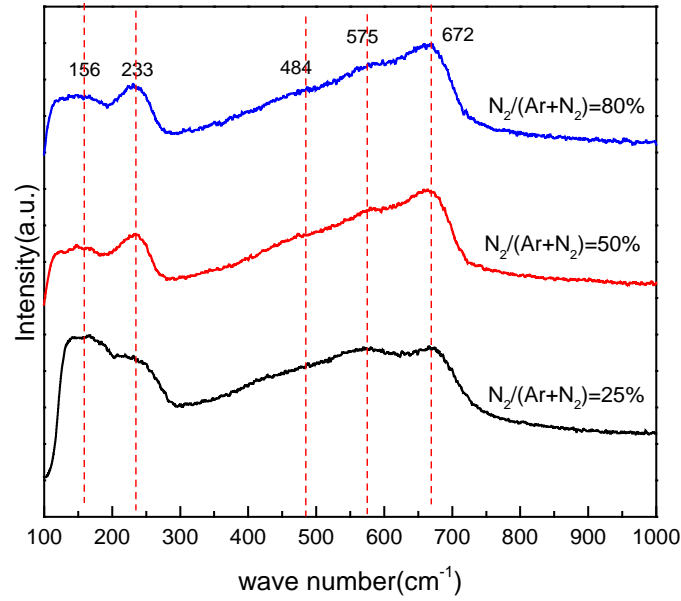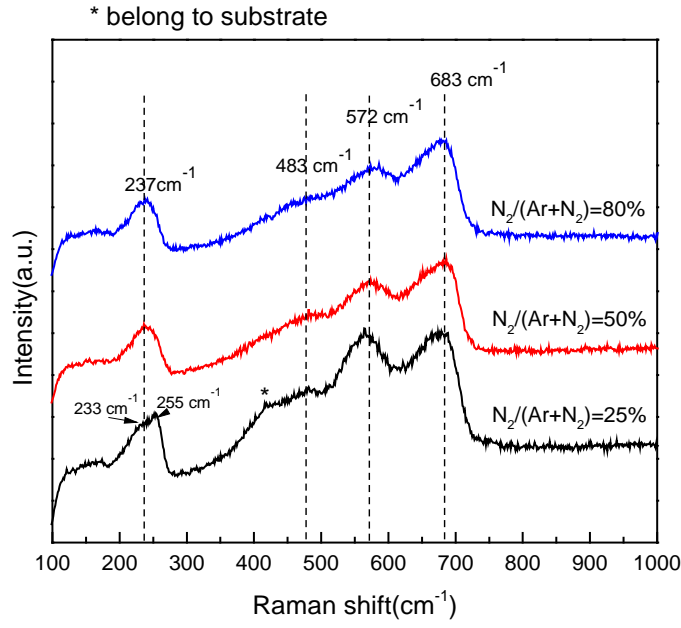
Figure 3.6 Upper: Raman spectrum of ZnSnN$_2$ thin films with different N$_2$/(N$_2$+Ar) ratios at a fixed substrate temperature of 400 ˚C(* from c-plane sapphire substrates); Lower: Raman spectrum of of ZnSnN$_2$ thin films with different N$_2$/(N$_2$+Ar) ratios at a fixed substrate temperature of 275 ˚C
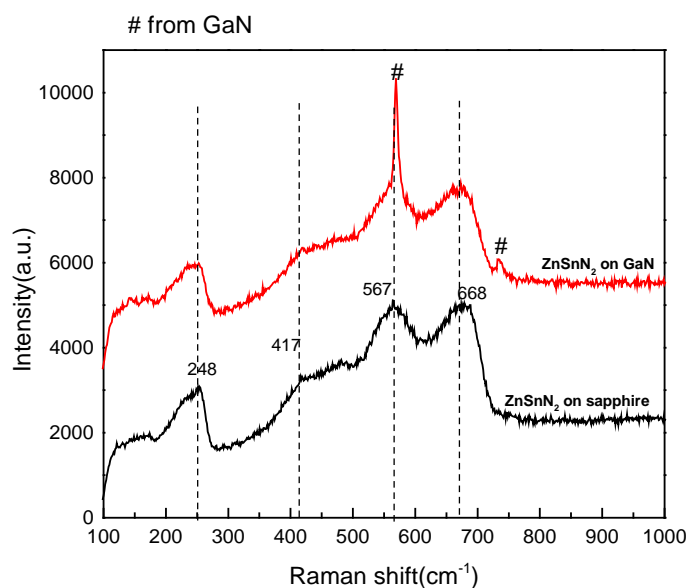
Figure 3.7 Raman spectrum of $ZnSnN_2$ thin films grown on c-plane sapphire substrate and (0001) GaN substrate with the $N_2/(N_2+Ar)$ of 25% at the substrate temperature of 400 ˚C

3.2.3 Chemical bonding, composition and valence band structure

Chemical bonding states, surface composition and valence band structure of $ZnSnN_2$ thin films were investigated by X-ray photoelectron spectroscopy (XPS). Bulk composition of films was investigated by energy dispersive X-ray spectroscopy (EDXS). XPS measurements were performed using a Kratos XPS Axis Ultra DLD system, with the base pressure of 10^{-8} Torr. A monochromatic Al Kα (1486.6 eV) X-ray source was used for excitation and the spectra of fine scans were collected with a pass energy of 20 eV. The obtained XPS spectra were referenced with respect to the surface C 1s line at the binding energy (BE) of 285.0 eV [75]. The spectra were curve-fitted by the commercial software package CasaXPS, with a mixture of Gaussian and Lorentzian line shapes based on a Shirley-type background. No Ar+ ion etching was performed

before collecting X-ray generated electrons to avoid denitrification of $ZnSnN_2$ films by Ar+ bombardment [76],[77]. EDXS results were obtained using a FEI Nova NanoSEM 230 scanning electron microscope. The accelerating voltage of 18 kV was used for EDXS measurements. Table 3.4 lists the details of different $ZnSnN_2$ thin films investigated by XPS and EDXS.

Table 3. 4 The details of different $ZnSnN_2$ samples

Sample No.	Substrate temperature (˚C)	$N_2/(N_2+Ar)$ (%)	Thickness(nm)
S3	325	50	340
S5	275	50	380
S8	400	50	400
Y4	400	25	400
Y6	400	80	380

Figure 3.8 to Figure 3.13 show the high resolution XPS spectra of Zn 2p 3/2 line, N1s line, and Sn 3d 5/2 line of $ZnSnN_2$ thin films deposited at different substrate temperatures with the fixed $N_2/(N_2+Ar)$ ratio of 50%. Figure 3.8 indicates that the position of Zn 2p 3/2 peak shifts from 1021.51 eV to 1021.11 eV in binding energy (BE) with the increase of substrate temperatures. This peak corresponds to the Zn-N bonding in $ZnSnN_2$ and the binding energy of this Zn-N bonding is lower than the one reported in Zn_3N_2 materials [76],[77]. We also find another small peak located at 1019.11 eV in the XPS spectrum of S5's Zn 2p 3/2 line. This peak is related to metallic Zn, suggesting the existence of secondary phase of metallic Zn at the surface of films deposited at the low substrate temperature (275˚C).
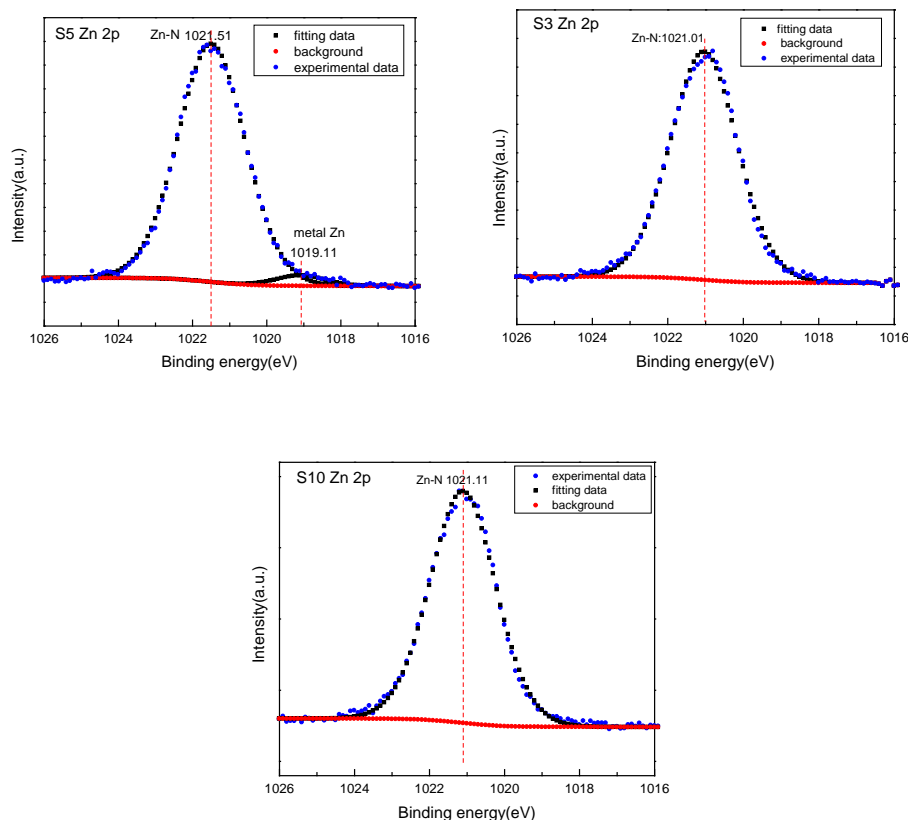
Figure 3. 8 High resolution XPS spectra of Zn 2p 3/2 line for different substrate temperature at the fixed $N_2/(N_2+Ar)$ ratio of 50% ; Upper left: 275˚C, Upper right: 325˚C, Lower: 400˚C

It is shown, in Figure 3.9, that two peaks are observed at the spectra of N1s line. The main N1s peak located at 396.31eV or 396.61eV is regarded as the combination of N-Zn bonding and N-Sn bonding in $ZnSnN_2$ films, indicating a significant chemical shift in comparison with the N 1s peak of free amine (398.8eV). The chemical shift in this peak (2.3 to 2.5 eV) is smaller than the chemical shift for Zn_3N_2 (3 eV) [76], suggesting that the N-metal (Zn and Sn) bonds of $ZnSnN_2$ undergo less ionization than the N-Zn bonds in Zn_3N_2. The broad and small peak is related to the N-H bonds reported at 398.3 eV [76]. It is possible that the hydrolysis

of ZnSnN$_2$ with air exposure leads to the formation of N-H bonds. In addition, by increasing the substrate temperatures, the binding energy of main N1s peak increased from 396.31eV to 396.61eV, which suggests the decrease in valence electron density of ZnSnN$_2$ surface [76].
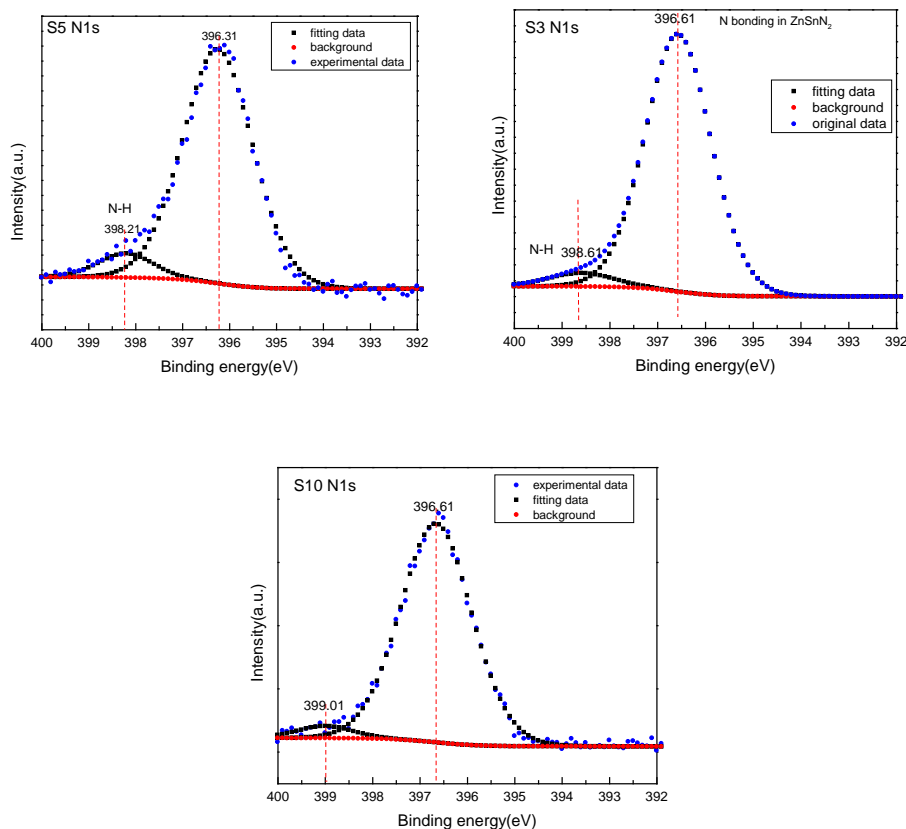
Figure 3.9 High resolution XPS spectra of N 1s line for different substrate temperature at the fixed N$_2$/(N$_2$+Ar) ratio of 50%; Upper left: 275°C, Upper right: 325°C, Lower: 400°C

Figure 3.10 demonstrates XPS spectra of Sn 3d 5/2 line at different substrate temperatures. The main Sn 3d 5/2 peak corresponds to the Sn-N bonds in ZnSnN$_2$ and the binding energy of this Sn-N bonding slightly increased from 486.01 eV to 486.21 eV with the increase in substrate temperatures. In addition, a small peak of metallic Sn is observed from the S10's spectrum, indicating the appearance of secondary phase of metallic Sn at the surface of films deposited at the high substrate temperature (400°C).

Figure 3.10 High resolution XPS spectra of Sn 3d 5/2 line for different substrate temperature at the fixed $N_2/(N_2+Ar)$ ratio of 50%; Upper left: 275˚C, Upper right: 325˚C, Lower: 400˚C

Figure 3.11 to Figure 3.13 show the high resolution XPS spectra of Zn 2p 3/2 line, N1s line, and Sn 3d 5/2 line of $ZnSnN_2$ thin films grown at various $N_2/(N_2+Ar)$ ratios at the fixed substrate temperatures of 400 ˚C. Figure 3.11 shows that the position of Zn 2p 3/2 peak shifts from 1021.11 eV to 1021.58 eV in binding energy (BE) with the increase of $N_2/(N_2+Ar)$ ratios.

Figure 3.11 High resolution XPS spectra of Zn 2p 3/2 for different $N_2/(N_2+Ar)$ ratios with the fixed substrate temperature of $400°C$; Upper left: 25%, Upper right: 50%, Lower: 80%

Figure 3.12 demonstrates the spectra of N 1s line for different $N_2/(N_2+Ar)$ ratios. We find that by increasing the $N_2/(N_2+Ar)$ ratios, the binding energy of main N1s peak increased from 396.61eV to 397.37eV, suggesting the decrease in valence electron density of $ZnSnN_2$ surface. Also, there is a negative correlation between the valence electron density and the $N_2/(N_2+Ar)$ ratios. In addition, the peak of N-H bonding cannot be observed in the spectrum of Y6's sample clearly. The reason is unclear and we assume that the large amount of N_2 incorporation during deposition suppressed the hydrolysis of $ZnSnN_2$ thin films, resulting in absence of the peak.

Figure 3.12 High resolution XPS spectra of N 1s for different $N_2/(N_2+Ar)$ ratios with the fixed substrate temperature of $400^\circ C$; Upper left: 25%, Upper right: 50%, Lower: 80%

Figure 3.13 shows XPS spectra of Sn 3d 5/2 line for different $N_2/(N_2+Ar)$ ratios. The binding energy of this Sn-N bonding increased slightly from 486.21 eV to 486.57eV with increasing $N_2/(N_2+Ar)$ ratios. In addition, the peaks representing metallic Sn are found in the spectra of Sample S10 and Y6, suggesting the appearance of secondary phase of metallic Sn at the surface of films deposited at the medium and high ratios of $N_2/(N_2+Ar)$ (50% and 80%). Finally, a peak at 487.57 eV is observed in the Y6's spectrum. This broad peak is attributed to Sn-O bonding due to the surface oxidation.
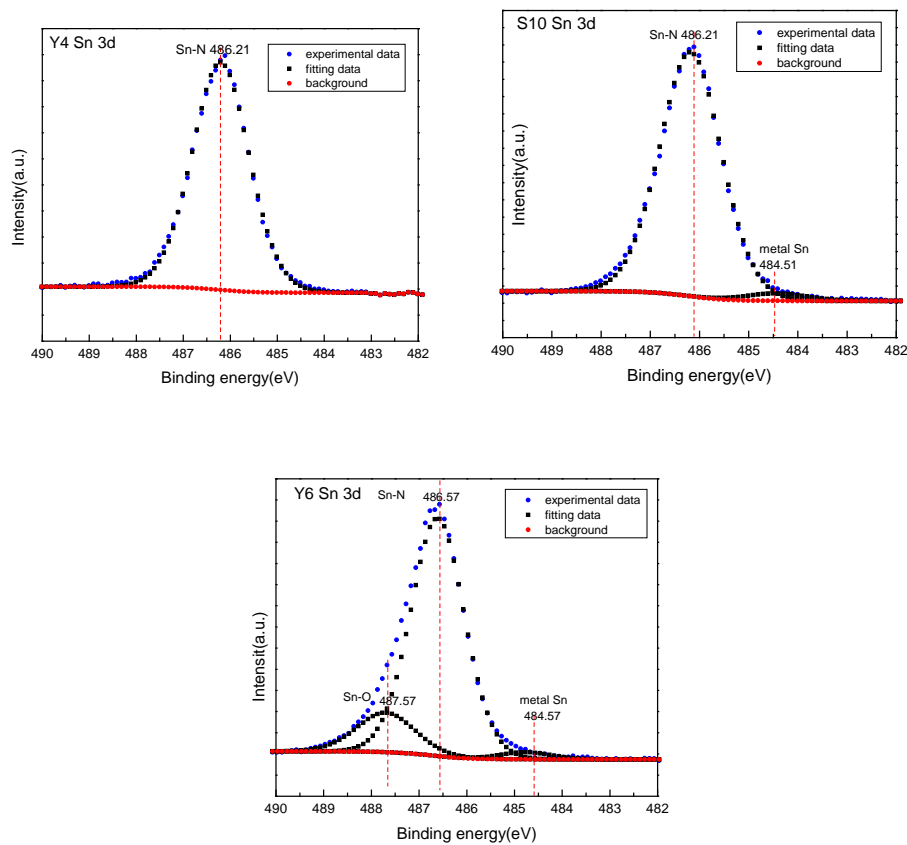
Figure 3.13 High resolution XPS spectra of Sn 3d 5/2 for different $N_2/(N_2+Ar)$ ratios with the fixed substrate temperature of 400˚C ; Upper left: 25%, Upper right: 50%, Lower: 80%

The surface and bulk composition are obtained from XPS and EDXS measurements. The compositional data are summarized in the Table 3.5 and Table 3.6, respectively. First, the surface composition is different from the bulk composition. For example, N-poor surface compositions are observed for all the samples by XPS. However, the bulk relative ratios of N/(Zn+Sn) are much closer to the stoichiometric target measured by EDXS results. This suggests the spatial existence of inhomogeneous composition distribution in our $ZnSnN_2$ films. Second, the surface relative ratio of Zn/Sn decreases from 1.62 to 0.98 with the increase in substrate temperatures from 275˚C to 400˚C. The same trend is also found in the bulk relative ratio of Zn/Sn. Third, with increasing $N_2/(N_2+Ar)$ ratios from 25% to 80% at the fixed substrate temperature of 400˚C,

the surface composition switches from Zn-rich to Sn-rich condition. The films, deposited at the substrate temperature of 400°C and $N_2/(N_2+Ar)$ of 50%, feature nearly stoichiometric composition.

Table 3.5 Summary of surface compositions of different samples analyzed by XPS

Sample No	Element composition (atomic %)			Relative ratio	
	Zn	Sn	N	Zn/Sn	N/(Zn+Sn)
S5	37.6	23.2	39.2	1.62	0.65
S3	32.1	27.2	40.7	1.18	0.68
S10	28.6	29.2	42.2	0.98	0.73
Y4	31.5	27.6	40.9	1.14	0.69
Y6	21.8	31.8	46.4	0.68	0.86

Table 3.6 Summary of bulk compositions of different samples analyzed by EDXS

Sample No	Element composition (atomic %)			Relative ratio	
	Zn	Sn	N	Zn/Sn	N/(Zn+Sn)
S3	28.34	20.32	51.32	1.39	1.03
S10	25.4	21.43	53.17	1.18	1.13
Y4	27.54	18.34	54.13	1.5	1.18
Y6	22.01	22.26	55.73	0.99	1.26
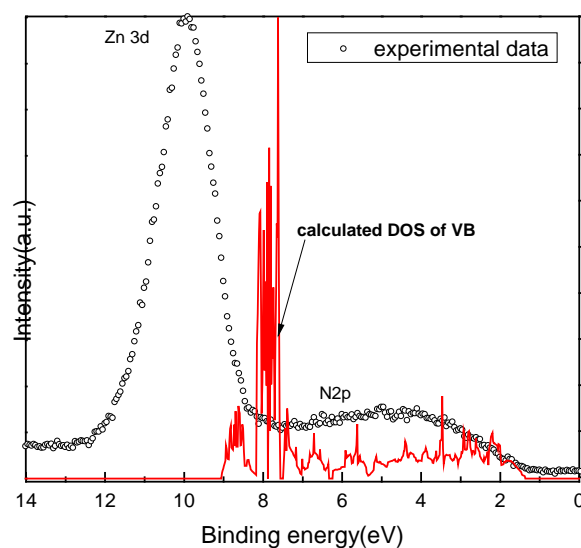
Figure 3. 14 Comparison of the XPS spectrum of valence band from our experiment (black dotted line) with our calculated VB-DOS (red solid line) for $ZnSnN_2$

Figure 3.14 shows the comparison of the XPS spectrum of valence bands from our experiment with our calculated density of states of valence bands (DOS of VB or VB-DOS) for $ZnSnN_2$ by DFT-HSE functional. The sample investigated by XPS was grown at the substrate temperature of 400 ˚C and with the $N_2/(N_2+Ar)$ ratio of 50%. The DFT calculations are performed with setting the value of valence band maximum (VBM) as zero eV. However, the experimental VBM at the surface is fitted to be 1.36eV away from the zero point. Therefore, the calculated DOS of VB was shifted horizontally by 1.36 eV in order to match the experimental location of the VBM from the XPS spectrum. It is suggested from the figure that the valence band structure measured by XPS is consistent with our calculated density of states of valence band. The sharp peak of Zn 3d orbital is near to the broad peak of N2p orbital and the overlap between these two peaks contribute most to the signal profile in the energy band region from -10eV to VBM. However, the peak position of Zn 3d orbital from experimental data is different from the calculated one. There are two possible reasons. (1) The film doesn't exhibit a

66

stoichiometric and defect-free surface. Then, these non-stoichiometric defects will affect the peak position. (2) In XPS measurement, the instrumental broadening [78], background noise as well as surface charging will also lead to unintentional peak shifts. By considering these factors, more resonances between calculated VB-DOS and XPS spectrum of valence bands can be achieved in the future.

Figure 3.15 shows the high resolution XPS spectra of valence band structure at different substrate temperatures with a fixed $N_2/(N_2+Ar)$ ratio of 50%. In this figure, it is shown that the position of VBM shifts from 0.51eV to 1.36 eV by increasing substrate temperatures from 275 ˚C to 400 ˚C. To explain this phenomenon, we propose two possible reasons. (1) The most favorable defects in $ZnSnN_2$ are Sn_{Zn} antisites with smallest formation energy according to the literatures [15],[73]. With the increase of substrate temperature, the relative ratio of Sn/Zn is changed from 1.62 to 0.98(details are listed in Table 3.5), which means that the surface composition shifts from a "Zn rich" to a "Zn-neutral" condition. Then, the population of Sn_{Zn} (n-type) point defects will increase. As a result, the Fermi level at the surface will be closer to the conduction band minimum as well as far from the valence band maximum. (2) With increasing substrate temperatures, the band gaps of $ZnSnN_2$ thin films increase from 1.6 eV to 1.9 eV, which will also lead to the VBM shift.

Figure 3.16 illustrates the high resolution XPS spectra of valence band structure at various $N_2/(N_2+Ar)$ ratios with a fixed substrate temperature of 400 ˚C. It is noted that the VBM has shifted from 1.26 eV to 1.61 eV due to the increase in the ratios of $N_2/(N_2+Ar)$ from 25% to 80%. The surface compositions of films are observed to change from a "Zn-rich" condition to a "Sn-rich" status. Again, the increase of Sn-enriched Zn-depleted defects will result in more

carrier density and a larger difference between Fermi level and valence band maximum (VBM) at the surface.
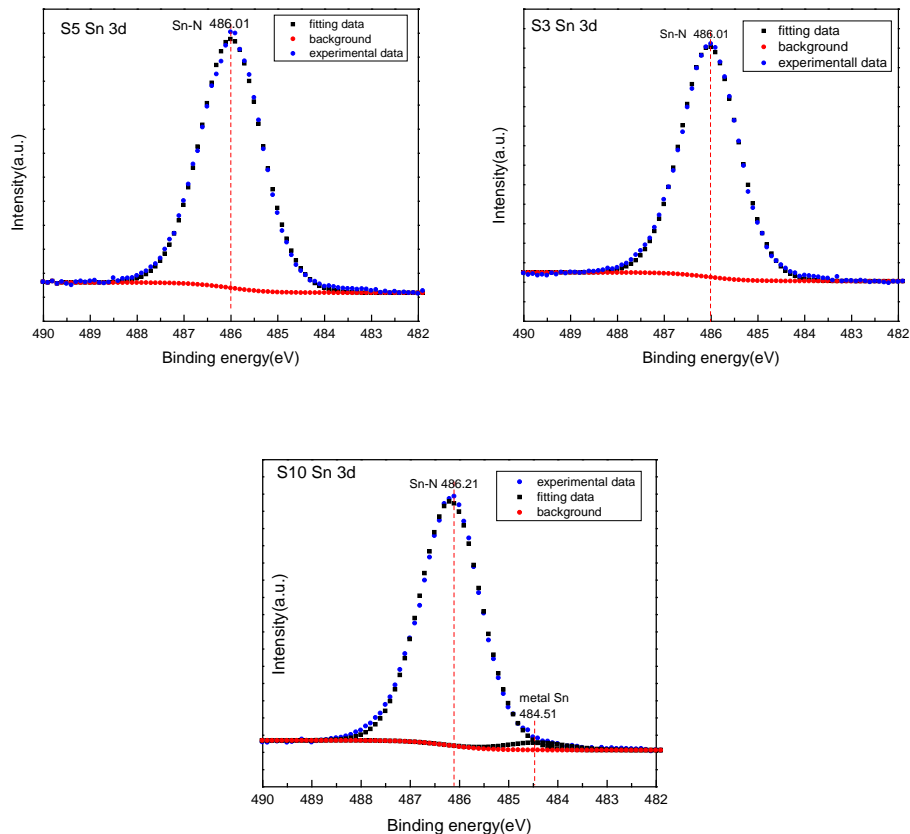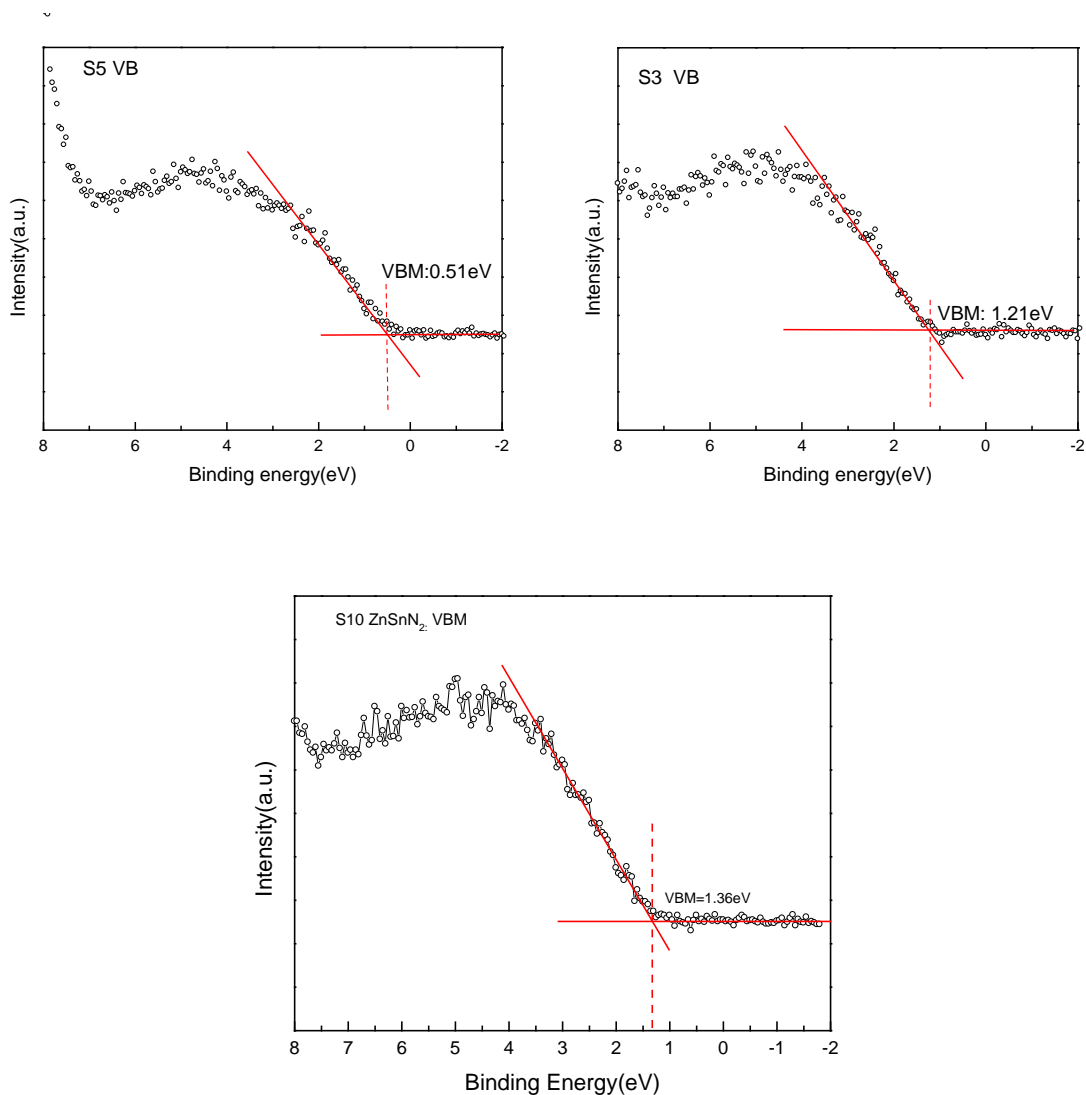

Figure 3.15 High resolution XPS spectra of valence band structure for different substrate temperature at the fixed $N_2/(N_2+Ar)$ ratio of 50%, Upper left: 275°C, Upper right: 325°C, and Lower: 400°C.
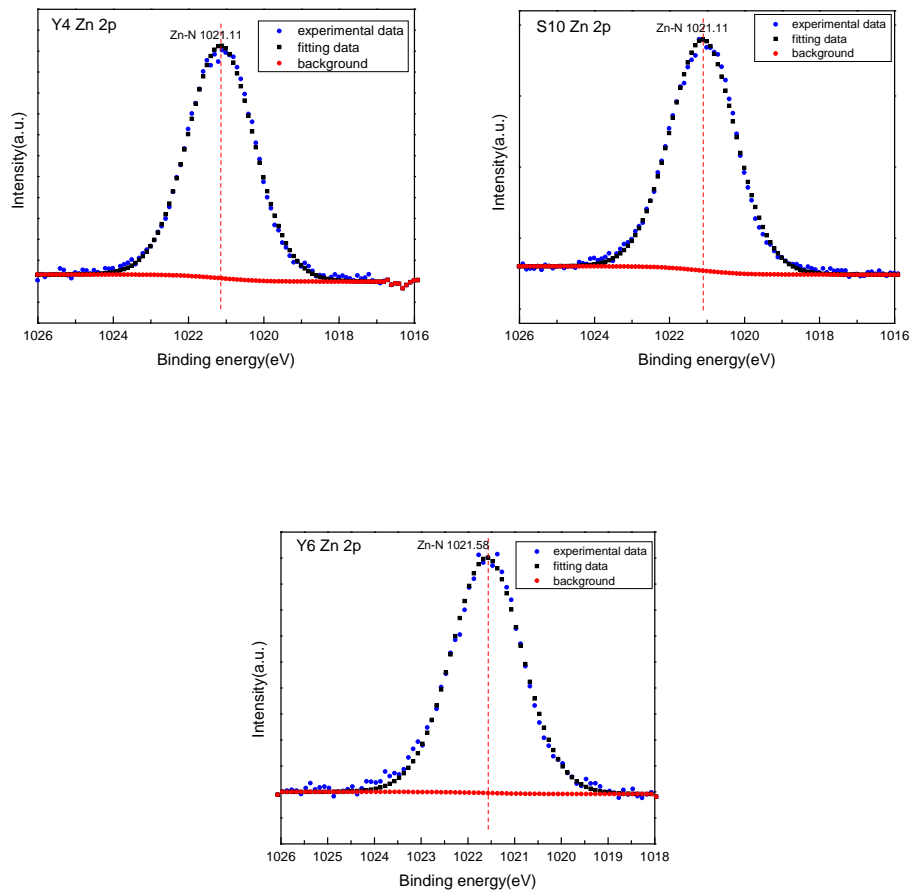
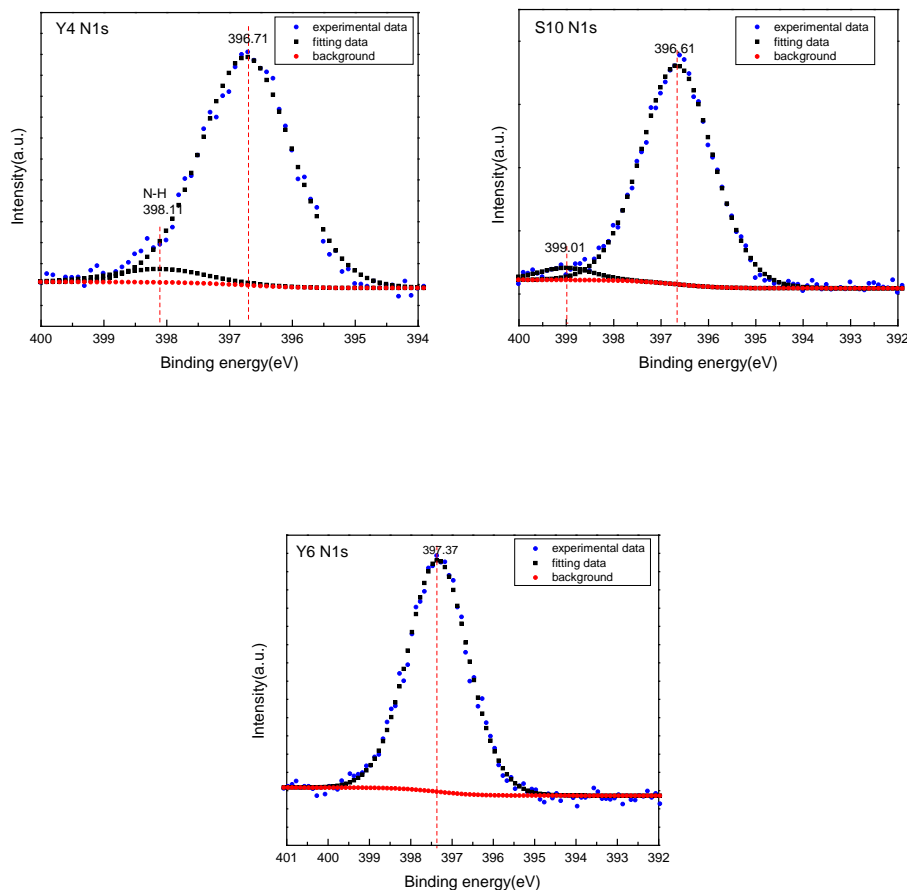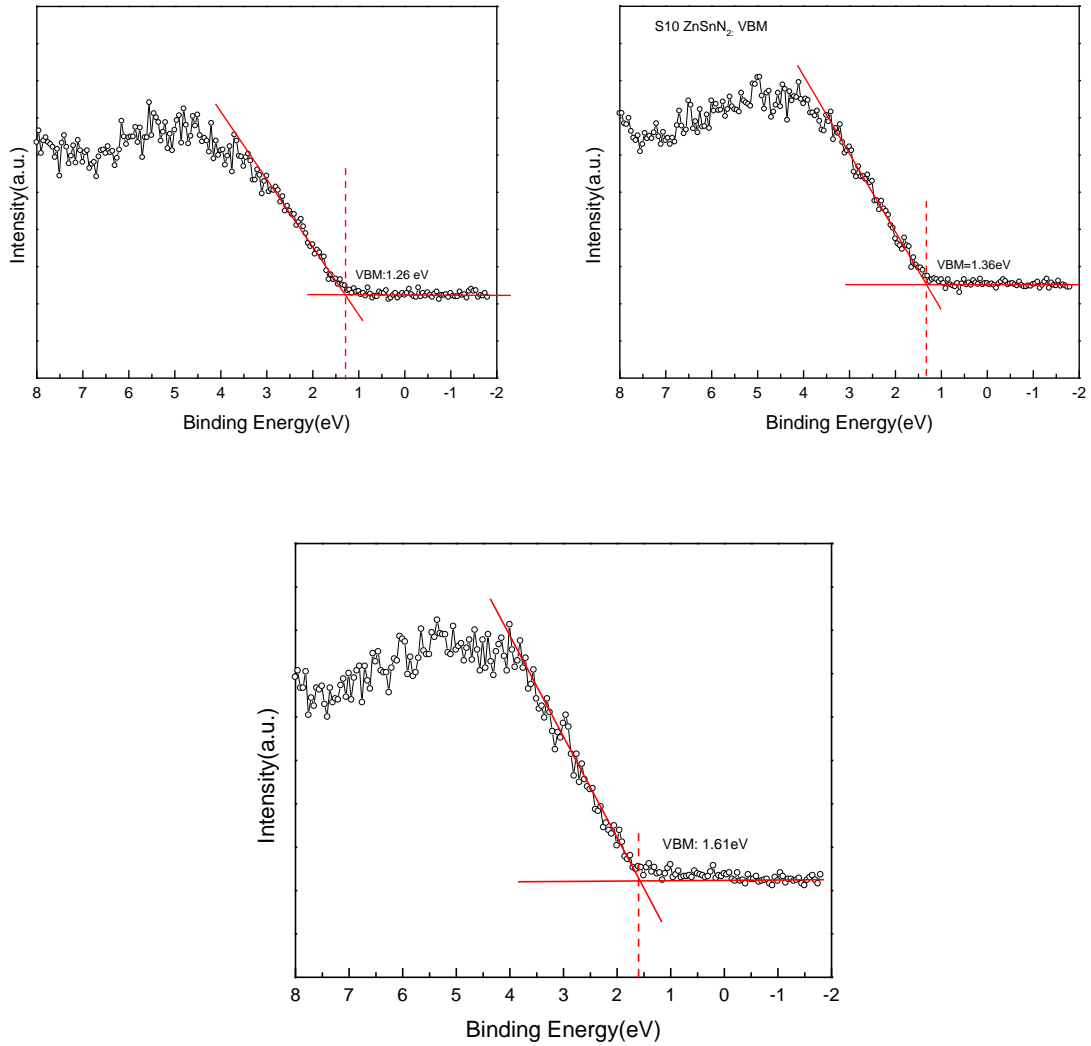Figure 3.16 High resolution XPS spectra of valence band structure for different $N_2/(N_2+Ar)$ ratios with the fixed substrate temperature of 400°C, Upper left: 25%, Upper right: 50%, and Lower: 80%.

3.2.4 Surface morphology

Scanning electron microscopy (SEM) and atomic force microscopy (AFM) were employed to investigate the properties of surface morphology of $ZnSnN_2$ thin films. The top-

view scanning electron microscope (SEM) images were taken on a FEI Nova NanoSEM 230 field emission scanning electron microscope. AFM images were obtained from a Quesant Q-scope atomic force microscopy (scanning probe microscopy).

Figure 3.17 shows the top-view SEM image of $ZnSnN_2$ thin films grown at the substrate temperature of 400 ˚C with a $N_2/(N_2+Ar)$ ratio of 50%. It is found that the film's surface is covered by many needle-like nano rods or wires. The dimension of these wires is around 100nm, which is roughly comparable to the mean crystallite size calculated by XRD measurements.
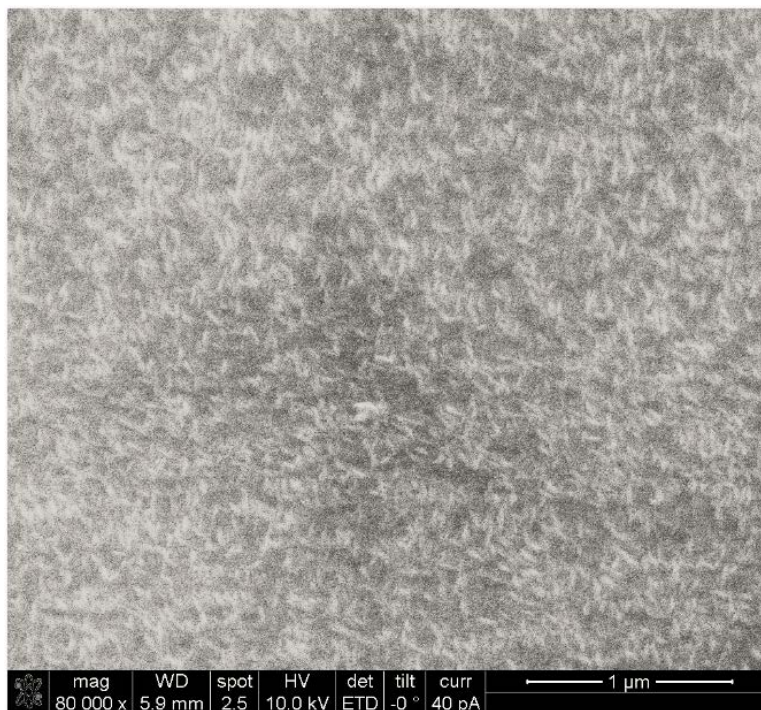
Figure 3.17 SEM image of $ZnSnN_2$ thin films deposited at the substrate temperature of 400 ˚C with $N_2/(N_2+Ar)$ ratio of 50%. (SEM conditions are HV=10kV, WD=5.9 mm, spot size=2.5, and scale bar=1um).

The surfaces of $ZnSnN_2$ thin films deposited at various substrate temperatures, from 325˚C to 400˚C, are illustrated in Figure 3.18. At the low temperature, a smooth and homogeneous surface is formed. No significant features or grain boundaries can be found,

suggesting the relatively smaller grain sizes. With the increase of substrate temperatures, the grain sizes increase obviously.
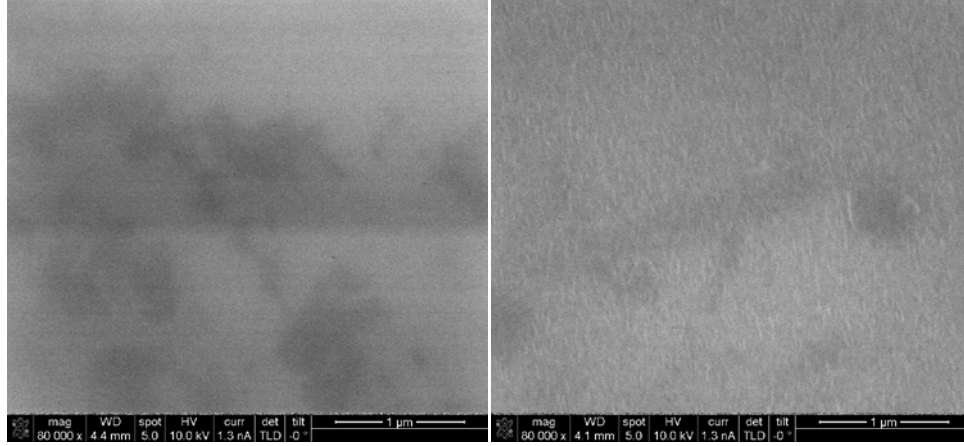
Figure 3.18 SEM images of $ZnSnN_2$ thin films deposited at the fixed $N_2/(N_2+Ar)$ ratio of 50% with different substrate temperatures, Left: 325 ˚C, and Right: 400 ˚C. (SEM conditions: HV=10kV, spot size=5, and scale bar=1um).

Figure 3.19 demonstrates the SEM images of $ZnSnN_2$ thin films grown at the substrate temperature of 400 ˚C with different $N_2/(N_2+Ar)$ ratios. At medium and high contents of N_2 incorporation, needle-like nano wires are found at the surfaces of films. In comparison, only some small grains are observed at the films grown at low ratio of $N_2/(N_2+Ar)$.
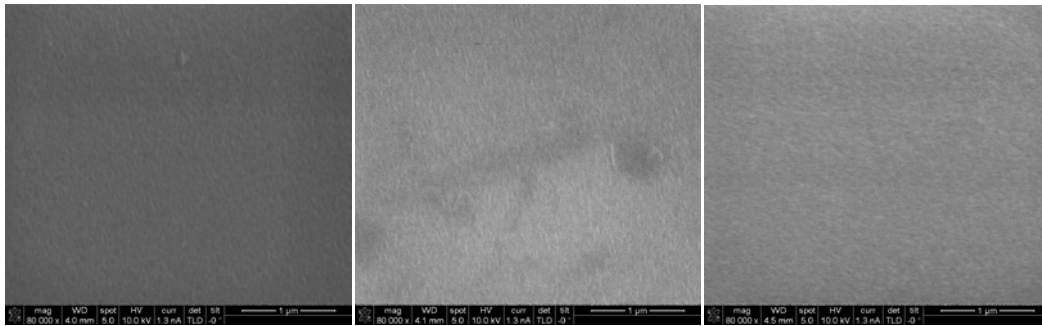
Figure 3.19 SEM images of $ZnSnN_2$ thin films deposited with a fixed substrate temperature of 400 ˚C with various $N_2/(N_2+Ar)$ ratios, Left: 25%, Middle: 50%, and Right: 80%. (SEM conditions: HV=10kV, spot size=5, and scale bar=1um).

Figure 3.20 shows the AFM images of $ZnSnN_2$ thin films deposited with a fixed substrate temperature of 400 ˚C with various $N_2/(N_2+Ar)$ ratios. With the increase in the ratios of $N_2/(N_2+Ar)$, the surfaces' features changes dramatically. Many needle-like columns along with the z-axis are observed at the surface with the $N_2/(N_2+Ar)$ ratio of 50%, in agreement with the SEM image. This finding also suggests the crystal growth with preferential orientation (along (002) direction), which has been confirmed by XRD measurement. In addition, no clear features are found at the surface with the $N_2/(N_2+Ar)$ ratio of 25%. Also, we can still observe some nano pillars at the surface with the $N_2/(N_2+Ar)$ ratio of 80%.
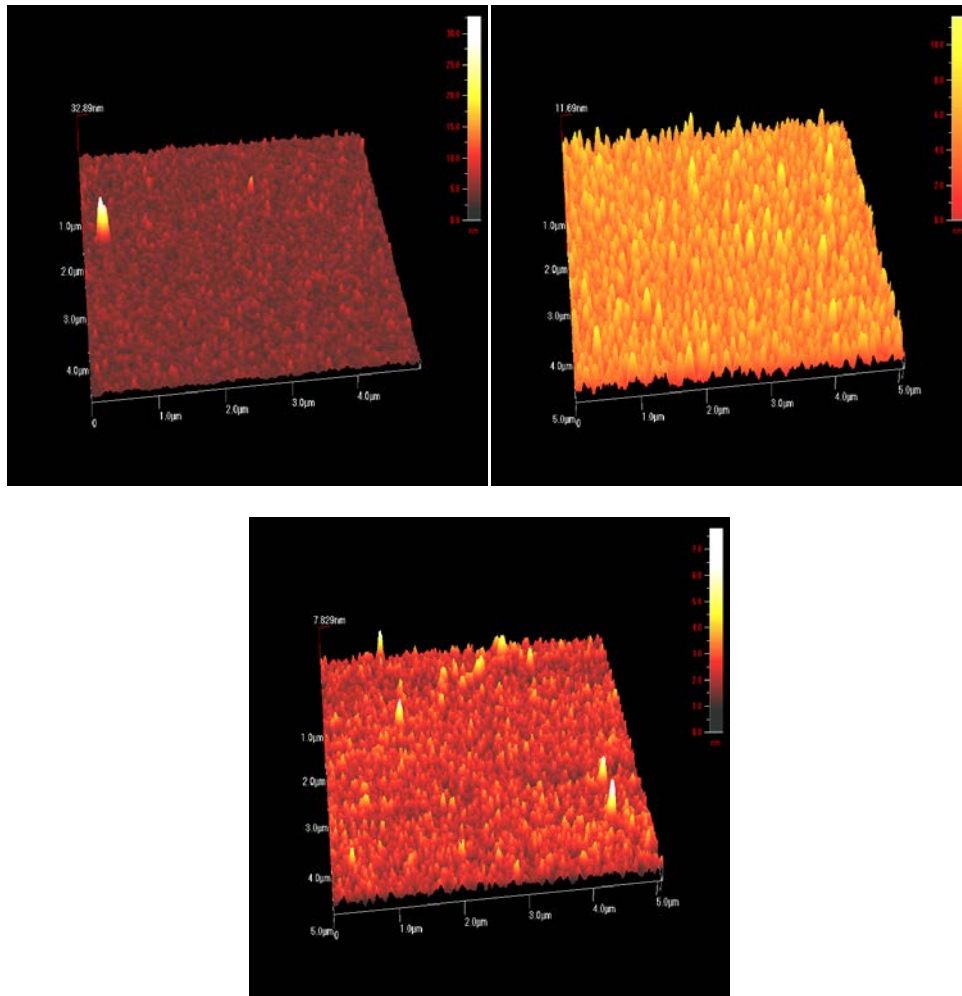
Figure 3.20 3D AFM images of $ZnSnN_2$ thin films deposited with a fixed substrate temperature of 400 ˚C with various $N_2/(N_2+Ar)$ ratios, 25%(upper left), 50%(upper right) and 80%(lower).

3.2.5 Electrical properties

The electrical properties of $ZnSnN_2$ films such as carrier concentration, resistivity and mobility were characterized by Hall-effect measurements and four-probe resistivity measurements. Our room temperature Hall measurements were operated in a DHE-21 Hall system from SES Instruments Pvt. Ltd, using a standard four point Vand der Pauw contact layout [77]. The four-probe resistivity measurements were carried on a Omnimap RS 35C resistivity mapper to obtain the films' resistivity. Because a good ohmic contact is usually required for electrical measurements including Hall and four-probe resistivity measurements, 120nm-thick Al films with Van der Pauw patterns were deposited on the $ZnSnN_2$ samples as ohmic contacts before our measurements. The magnetic field's magnitude was set to 2700 G in Hall system. The investigated samples were grown on c-plane sapphire substrates and (0001) GaN substrates with different substrate temperatures and $N_2/(N_2+Ar)$ ratios. All samples are found to feature n-type semiconductor characteristics. For most samples, the carrier concentration is in the range of 10^{19} cm^{-3} to 10^{21} cm^{-3}, the resistivity is between 10^{-2} Ωcm and 10^{-3} Ωcm, and the values of mobility are in the range of 4.5 to 9.6 $cm^2V^{-1}s^{-1}$. These results are consistent with the data reported in previous works [12],[29],[30],[72],[73]. It is necessary to mention that the mobility of $ZnSnN_2$ films, deposited on GaN substrate with the $N_2/(N_2+Ar)$ ratio of 25% and at the substrate temperature of 400 ˚C, was measured to be 48 $cm^2V^{-1}s^{-1}$. To our knowledge, this is the reported highest Hall mobility for polycrystalline $ZnSnN_2$ thin films until now.

Figure 3.20 reflects the relationship between the electrical properties of $ZnSnN_2$ and different substrate temperatures. The carrier concentration increased as the substrate temperature was increased. And the resistivity correspondingly decreased with the increase of substrate temperature. It is noted that the resistivity values are minimally affected by the substrate

temperature in the range between 325 ˚C and 400 ˚C. In contrast, a sharper change of resistivity is observed as the substrate temperature increases from 275 ˚C to 325 ˚C.

The Hall mobility first increased then decreased with increasing temperatures from 275 ˚C to 400 ˚C. To understand this phenomenon, we need to investigate the carrier transport in ZnSnN$_2$ thin films. The relationship among Hall mobility, carrier concentration and resistivity is illustrated using the following equation:

$$\mu = \frac{1}{\rho n e} \qquad (3\text{-}4)$$

Here, μ is Hall mobility, ρ is the resistivity, n is carrier concentration, and e is the electron charge (1.6×10^{-19} C). It is well known that the mobility of polycrystalline semiconductors is mainly determined by ionized impurity scattering and grain boundary scattering [77],[79]. When the temperature increases from 275 ˚C to 325 ˚C, the crystallinity of films has significantly improved. The average grain size changes from 10nm to 55nm, as confirmed by XRD analysis. As a result, the mobility increases although the carrier concentration also increases, suggesting the grain boundary scattering is a main factor affecting the mobility in this temperature region. As the temperature increases from 325˚C to 400˚C, the ionized impurity scattering is more dominant in determining the hall mobility. At high temperature, more defects are activated and these ionized defects can act as the source of impurity scattering (or charged carrier scattering) as well as assist with increasing the carrier concentration [73]. In our case, the population of Sn$_{Zn}$ anti-site point defects (most favorable defects in ZnSnN$_2$) is estimated to increase dramatically with the increase in temperature, according to the decrease of Zn/Sn ratios from XPS measurements. So, we speculate that the ionized Sn$_{Zn}$ anti-site defects contribute most parts of concentration of charged carrier scattering centers at the high growth temperature. Additionally,

74

the crystallinity of films deposited at 325°C is slightly different from the one of 400 °C films. The values of FWHM of 325°C and 400 °C films are 0.221° and 0.178°, respectively based on the fitting data of (121) peak from XRD analysis.

The impacts of different $N_2/(N_2+Ar)$ ratios on the electrical properties of $ZnSnN_2$ films are illustrated in Figure 3.22. A downward trend was observed in carrier concentration with the increase of $N_2/(N_2+Ar)$ ratios from 25% to 80%. The decrease in carrier concentration is partially attributed to the formation of N-N bonding in the context of high N_2 content in the mixture of total reactive gas [77]. In addition, the bulk composition of films shifts from Zn-richness to Zn-neutrality with more nitrogen atoms activated by plasma, leading to the loss of Zn_i interstitial point defects(n-type defects in $ZnSnN_2$) as well as the decrease of the carrier concentration. The resistivity of films, simultaneously, increased with increased incorporation of $N_2/(N_2+Ar)$ ratios. The hall mobility first decreased then increased with the variance of $N_2/(N_2+Ar)$ ratios.
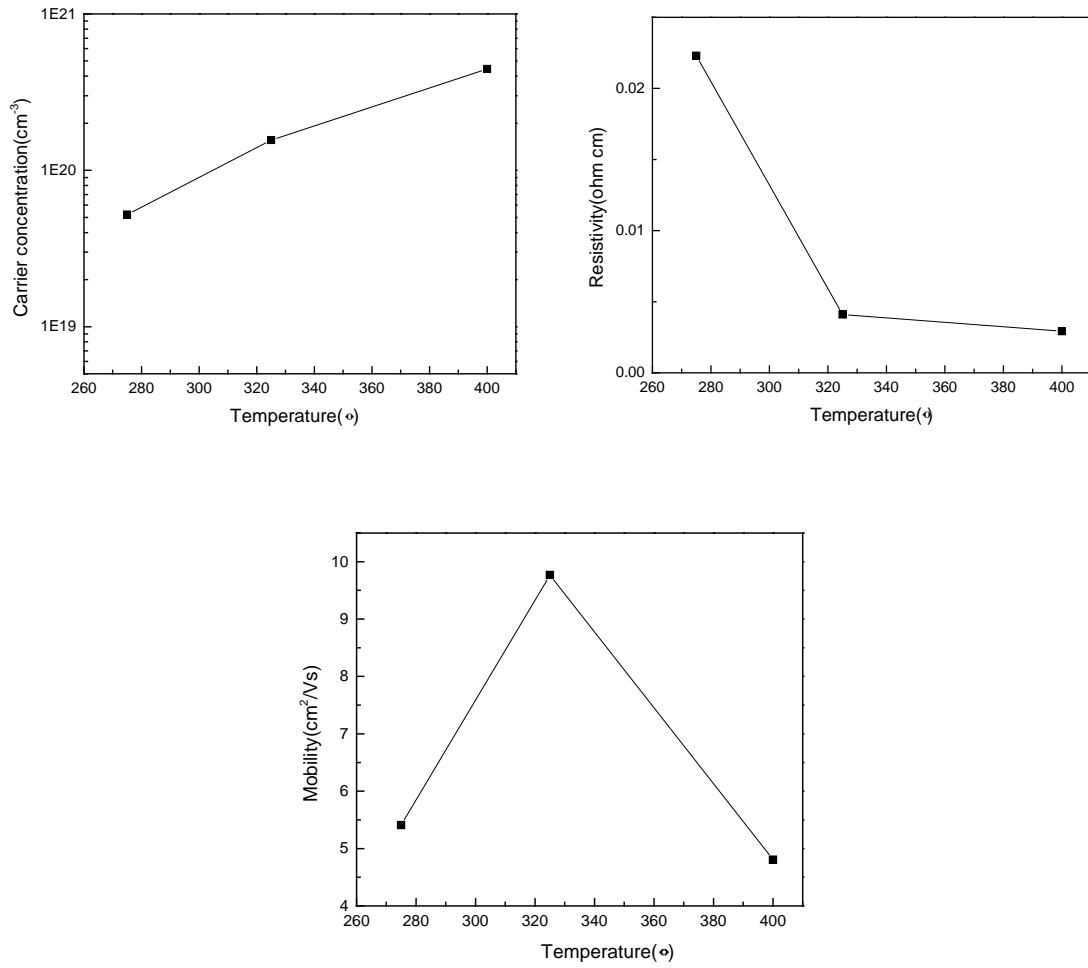
Figure 3.21 Electrical properties of ZnSnN$_2$ thin films as a function of substrate temperatures, carrier concentration (upper left), resistivity (upper right) and mobility (lower). The films are deposited at a fixed N$_2$/(N$_2$+Ar) ratio of 50%.
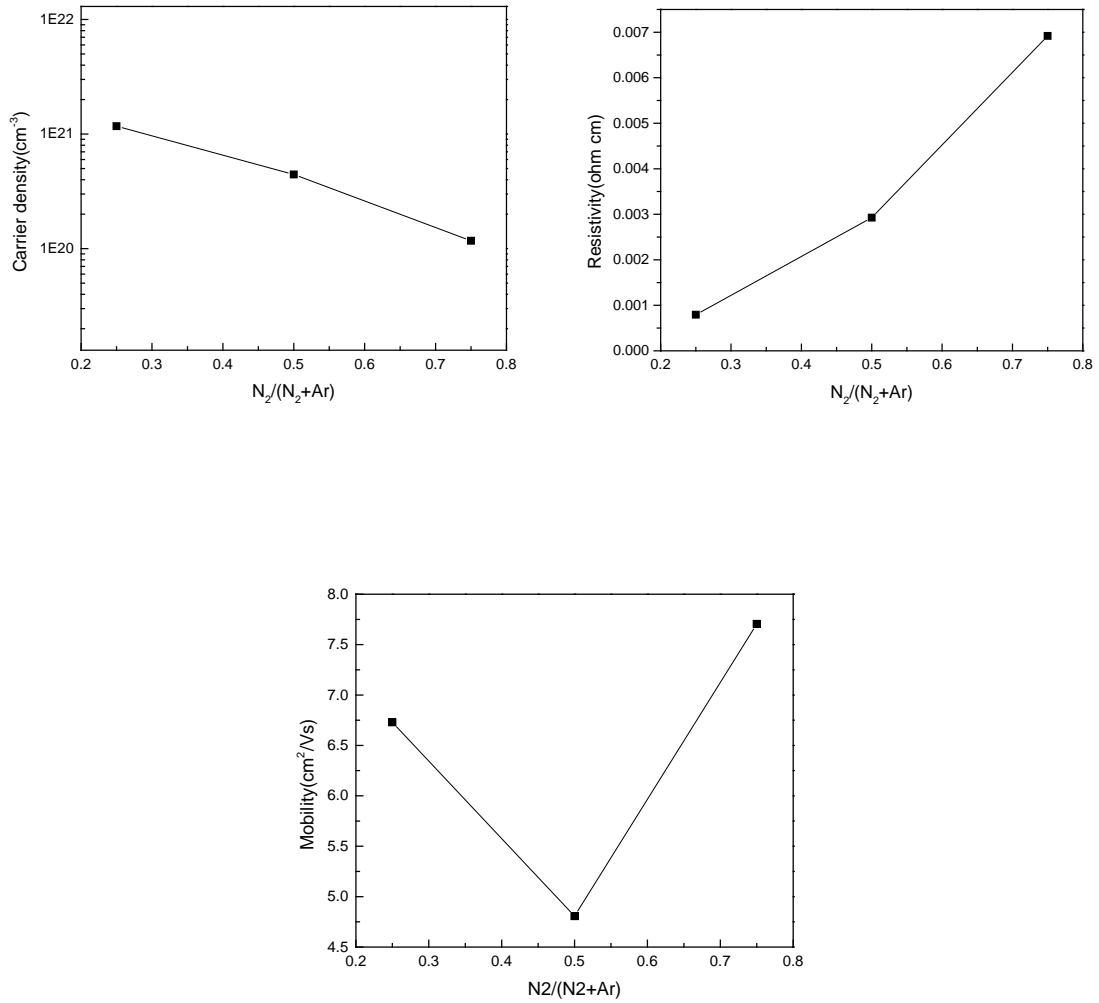
Figure 3.22 Electrical properties of ZnSnN$_2$ thin films as a function of N$_2$/(N$_2$+Ar), carrier concentration (upper left), resistivity (upper right) and mobility(lower). The films are deposited at a fixed substrate temperature of 400 ˚C.

3.2.6 Optical properties

The optical transmittance and reflectance of ZnSnN$_2$ thin films were collected using a Shimadzu UV-3101PC UV/VIS/NIR scanning spectrometer from the wavelength of 300nm to 1200nm. The absorption coefficient (α) of ZnSnN$_2$ was obtained based on the analysis of film's transmittance as well as reflectance. Since ZnSnN$_2$ is a kind of direct band gap semiconductor,

the band gaps can be estimated based on the linear extrapolation from the curve of square of absorption coefficient (α^2) versus photon energy (hv) to the energy axis. The optical band gaps of our films with different growth conditions are in the range between 1.6eV and 1.93eV, which are in good agreement with the band gap calculated by our DFT method (2.08eV). These numerical values are also comparable to the band gaps reported by other research groups [10,13,27,28,73,74].

The square of absorption coefficient plotted as a function of photon energy is indicated in Figure 3.23. With the increase of substrate temperatures, the band gaps increased from 1.6 eV to 1.93 eV. This change was in coincidence with the increase of carrier concentration obtained by Hall measurements, suggesting a large Burstein-Moss effect on the apparent band gap of $ZnSnN_2$ films [12]. The Burstein-Moss effect results from the conduction band filling, namely, more free electrons filling the bottom of conduction band will cause larger optical band gaps. Our results are also consistent with the results from previous works [12],[73].

Figure 3.24 shows the effects of different $N_2/(N_2+Ar)$ ratios on the optical properties of $ZnSnN_2$ films. With the increase of $N_2/(N_2+Ar)$ ratios, the band gaps of films were almost the same. Possibly, the optical band gap is minimally affected by the variance of N_2 concentration in the mixture of total reactive gas. The reason is still not clear and more investigations are needed to understand this phenomenon.
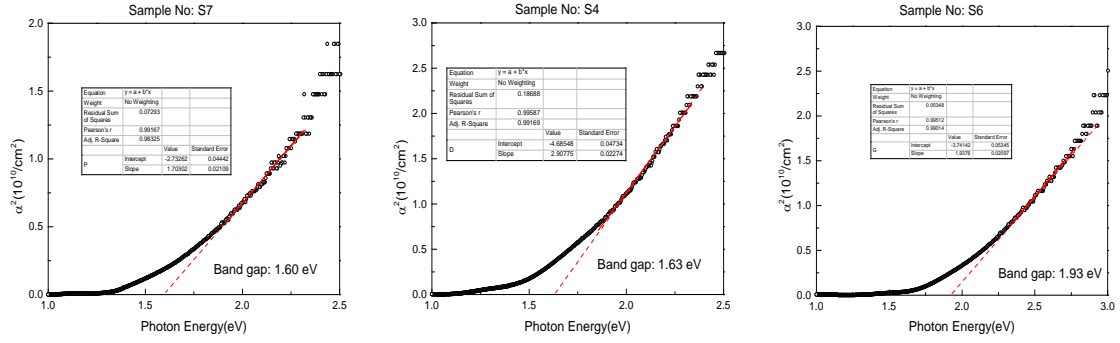
Figure 3.23 Plots of square of absorption coefficient (α^2) versus photon energy (hv) of ZnSnN$_2$ films deposited at different substrate temperatures with a fixed N$_2$/(N$_2$+Ar) ratio of 50%, Left: 275˚C, Middle:325˚C Right: 400˚C.
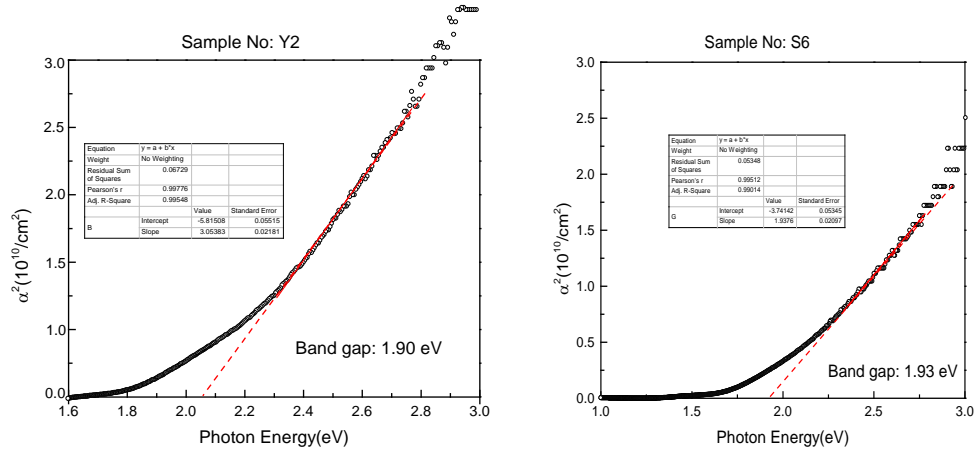
Figure 3.24 Plots of square of absorption coefficient (α^2) versus photon energy (hv) of ZnSnN$_2$ films deposited with different N$_2$/(N$_2$+Ar) ratios of 50% at a fixed substrate temperatures of 400˚C, Left: 25% , Right: 50%.

3.3 Device applications of zinc tin nitride thin films

3.3.1 Device fabrication

In this study, the electrical devices based on $ZnSnN_2$ thin films were fabricated using the standard process for semiconductor devices, including substrate cleaning, photo lithography, wet and dry etching, metal deposition, etc. Figure 3.25 shows the flow chart of the fabrication process. More details can be seen in Appendix B.

```
┌─────────────────────────┐
│    Substrate cleaning   │
└─────────────────────────┘
             │
             ▼
┌─────────────────────────┐
│    ZnSnN₂ deposition    │
└─────────────────────────┘
             │
             ▼
┌─────────────────────────┐
│    Photoresist coating  │
└─────────────────────────┘
             │
             ▼
┌─────────────────────────┐
│    Photo-lithography    │
└─────────────────────────┘
             │
             ▼
┌─────────────────────────┐
│   Developing photoresist│
└─────────────────────────┘
             │
             ▼
┌─────────────────────────┐
│     Metal contact       │
└─────────────────────────┘
             │
             ▼
┌─────────────────────────┐
│   Stripping photoresist │
└─────────────────────────┘
             │
             ▼
┌─────────────────────────┐
│      Post-annealing     │
└─────────────────────────┘
             │
             ▼
┌─────────────────────────┐
│    Devices completed    │
└─────────────────────────┘
```
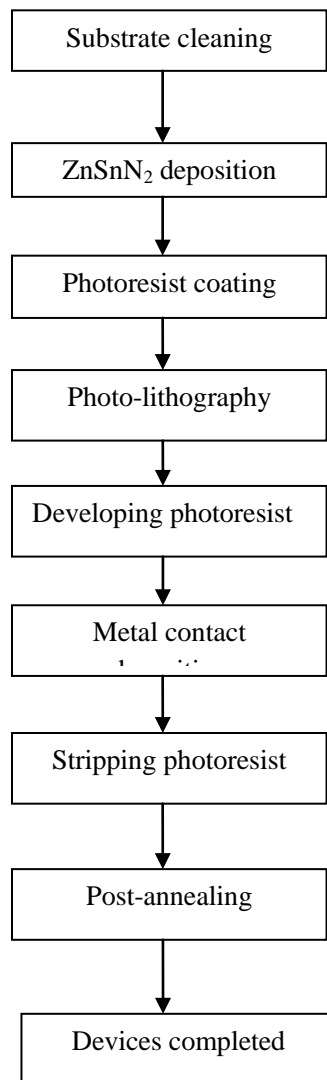
Figure 3.25 Flow chart of fabrication process

Figure 3.26 and Figure 3.27 demonstrate the device structure for contact resistance measurements and the device structure of the diodes based on $ZnSnN_2$/GaN heterojunctions respectively. In the case of contact resistance measurements, 380-400nm thick $ZnSnN_2$ layers were grown on the c-plane sapphire substrates by a reactive RF-magnetron sputtering method. The metal contacts based on a sequence of 20nm Ti, 120nm Al, 40nm Ni, and 50nm Au were deposited on top of thick $ZnSnN_2$ films, according to the patterns of transmission line measurement (TLM). In terms of the diodes' structure, 18 to 20nm thick $ZnSnN_2$ films were deposited on (0001) GaN templates from Kyma technologies (5um GaN films grown on c-plane sapphire substrates by HVPE method) to form $ZnSnN_2$/GaN heterojunctions. All of the metal contacts were fabricated in a stack of 20nm Ti, 120nm Al, 40nm Ni, then 50nm Au, showing good ohmic characteristics between metal and semiconductors.

Metal contact 20nm Ti/120nm Al/ 40nm Ni /50nm Au

320nm thick $ZnSnN_2$ thin films

c-plane sapphire substrate
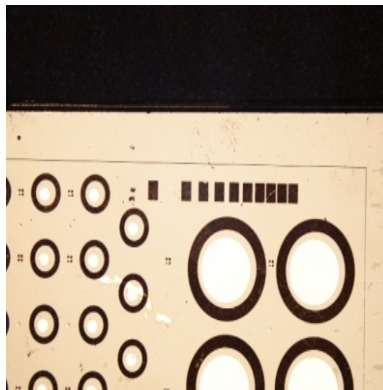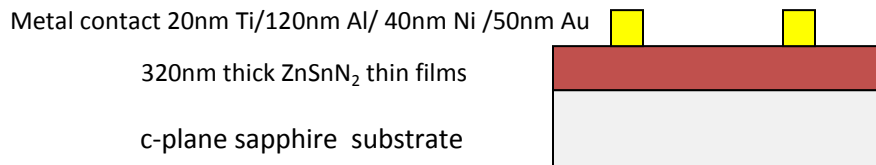
Figure 3.26 Upper: Device structure for contact resistance measurement Lower: a top-view image of the layout for contact resistance taken by a Nikon optical microscopy with 2X magnification

81

Gold layer: metal contact 20nm Ti/120nm Al/ 40nm Ni/ 50nm Au

Brown layer: 20nm ZnSnN$_2$

Purple layer: 5um GaN template

Grey layer: c-plane sapphire substrate

Inner gold circle: metal contact with ZnSnN$_2$(ohmic contact)

Outer gold circle: metal contact with GaN template(ohmic contact)

200um

1000um

1200um
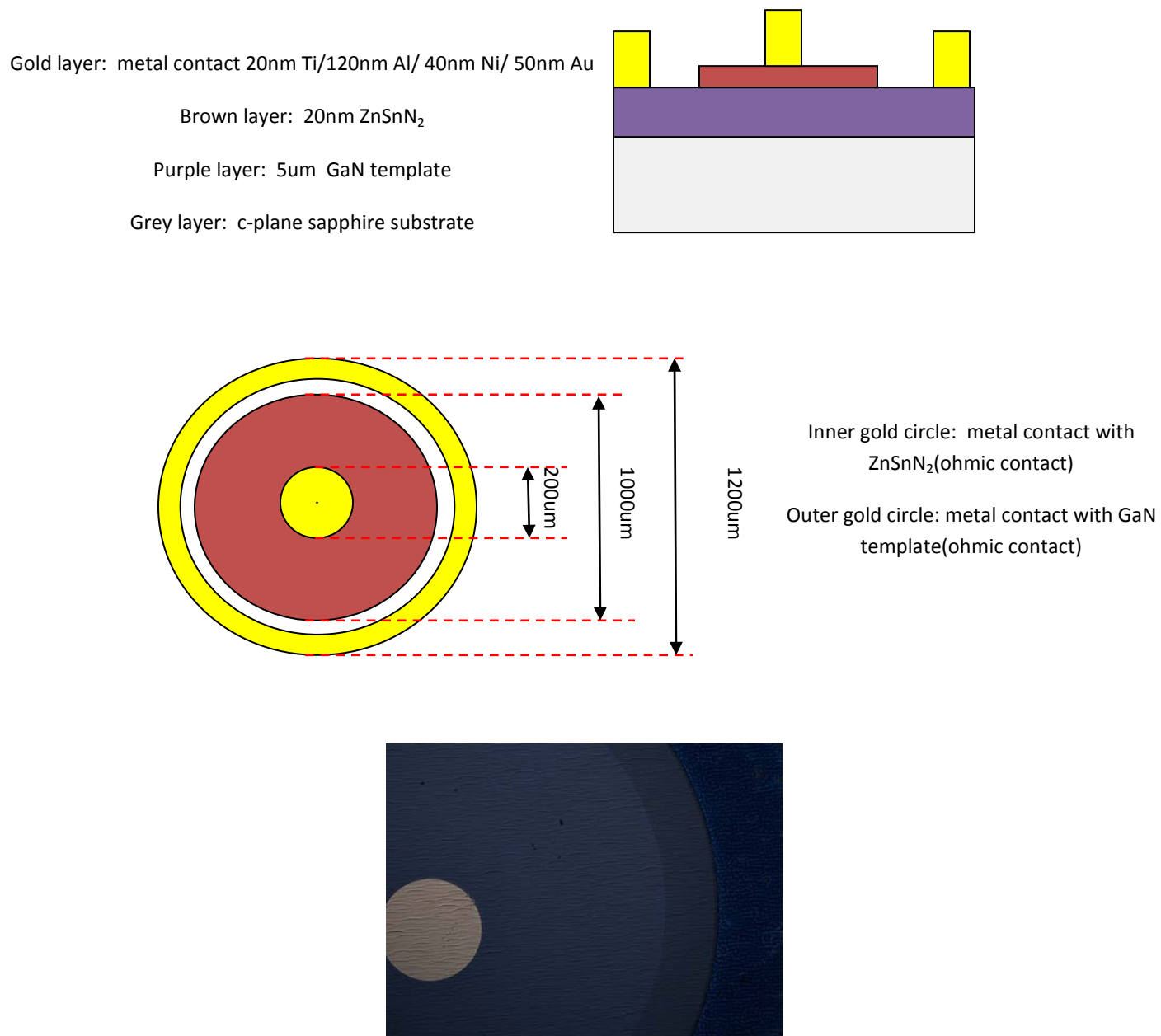
Figure 3. 27 Upper: cross-section of the diodes based on ZnSnN$_2$/GaN heterojunctions, Middle: top-view of the diodes' structure based on ZnSnN$_2$/GaN heterojunctions Lower: a top-view image of diodes' configuration taken by a Nikon optical microscopy with 20X magnification

3.3.2 Band alignment of ZnSnN$_2$/GaN heterojunctions

It is very important to study the band offsets between ZnSnN$_2$ and GaN to optimize the performance of opto-electrical devices based on ZnSnN$_2$/GaN heterojunctions. In 2013, A. Punya et al. pointed out that a type II band alignment is found between ZnSnN$_2$ and GaN, using the density functional theory (DFT) method[33]. According to their theoretically calculated results, the valence band offset (VBO) and the conduction band offset (CBO) are 1.9eV and -0.2eV respectively. However, until now, no experimental results have been reported about the band offsets of this novel heterojunction. Here, we measured the band offsets at the interface between ZnSnN$_2$ and GaN using the X-ray photoelectron spectroscopy (XPS) technique for the first time.

The valence band offset of ZnSnN$_2$/GaN heterojunctions can be obtained using: the XPS detection of the valence band and the core-level photo-emission from bulk ZnSnN$_2$ sample, a bulk GaN sample, and a sample with an interface between ZnSnN$_2$ and GaN. The "interface" sample is required to be thin enough to acquire the XPS core-level signals of both the ZnSnN$_2$ layers and the underlying GaN templates. Therefore, in our work, ultra-thin ZnSnN$_2$ layers(thickness around 3-4nm) were grown on the (0001) GaN templates by carefully controlling the deposition time and sputtering rate. Additionally, 380 to 400nm thick ZnSnN$_2$ films were deposited on the c-plane sapphires, acting as the bulk ZnSnN$_2$ samples. And the bulk GaN samples were 5 um thick GaN templates from Kyma technologies.

Valence band offset (VBO) between ZnSnN$_2$ and GaN is determined by the following equation:

$$VBO = [E_{CL}^{ZnSnN_2}(b) - E_V^{ZnSnN_2}(b)] - [E_{CL}^{GaN}(b) - E_V^{GaN}(b)] - [E_{CL}^{ZnSnN_2}(i) - E_{CL}^{GaN}(i)] \qquad (3\text{-}5)$$

The subscripts "CL" and " V" denote the binding energy(BE) for the core-level and valence band maximum (VBM). The notions (b) and (i) indicate the bulk and interface binding energies, respectively. This method has been widely used to calculate the band offsets of GaN-related heterojunctions such as Al_2O_3/GaN and InN/GaN [75],[80],[81]. Table 3.7 shows detailed information of the tested $ZnSnN_2$ samples.

Table 3.7 Details of different $ZnSnN_2$ samples deposited at 400 ˚C

Sample No	Type	Thickness of $ZnSnN_2$(nm)	$N_2/(N_2+Ar)$ (%)	Substrate
S10	bulk	400	50	c-plane sapphire
Y4	bulk	400	25	c-plane sapphire
X1	interface	4	50	GaN template
X12	interface	4	25	GaN template

Figure 3.28 to 3.32 show the XPS spectra of Ga 3d, Zn 3d core-level and valence bands for "interface" $ZnSnN_2$ ($ZnSnN_2$/GaN heterojunctions), "bulk" GaN, and "bulk" $ZnSnN_2$ samples. The values of valence band maximum (VBM) for different samples are obtained, by extrapolating from the intersections between the leading edge of valence band spectrum and the baseline [80]. Table 3.8 summarizes the binding energy of core-level peaks in "bulk" GaN, "bulk" $ZnSnN_2$, and "interface" $ZnSnN_2$ samples.
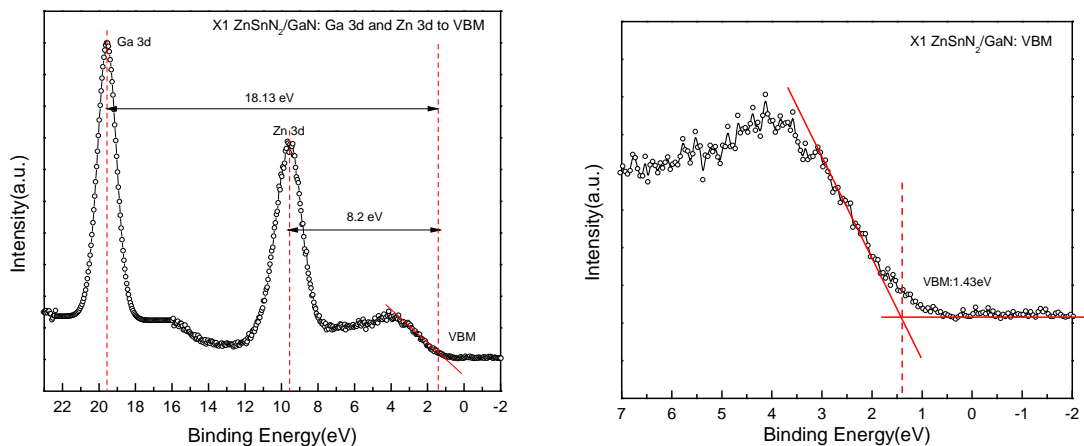
Figure 3.28 Left: High resolution XPS spectrum of Ga 3d, Zn 3d core-level and valence bands for X1 ("interface" ZnSnN$_2$ sample deposited on GaN template with a N$_2$/(N$_2$+Ar) ratio of 50%) Right: fine scan spectrum of valence band structure for X1
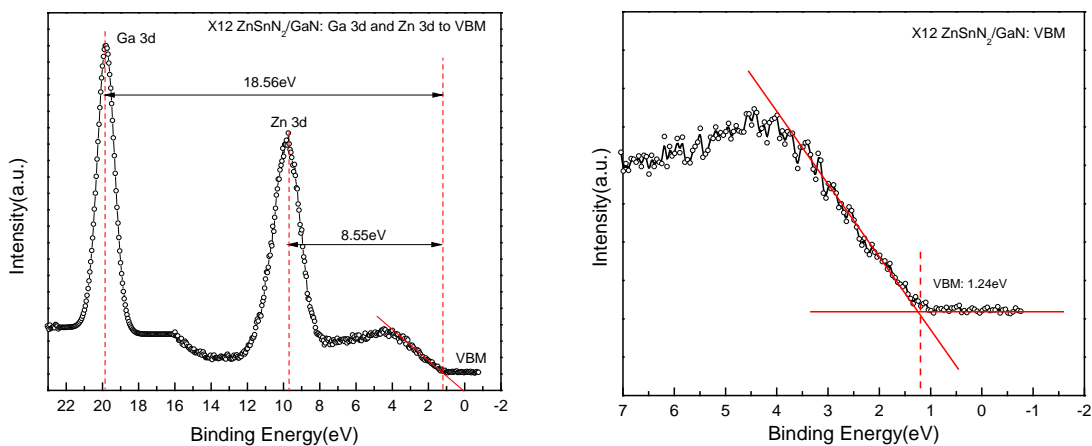
Figure 3.29 Left: High resolution XPS spectrum of Ga 3d, Zn 3d core-level and valence bands for X12 ("interface" ZnSnN$_2$ sample deposited on GaN template with a N$_2$/(N$_2$+Ar) ratio of 25%) Right: fine scan spectrum of valence band structure for X12

Figure 3.30 Left: High resolution XPS spectrum of Zn 3d core-level and valence bands for S10 ("bulk" ZnSnN$_2$ sample deposited on c-plane sapphire substrates with a N$_2$/(N$_2$+Ar) ratio of 50%) Right: fine scan spectrum of valence band structure for S10

Figure 3.31 Left: High resolution XPS spectrum of Zn 3d core-level and valence bands for Y4 ("bulk" ZnSnN$_2$ sample deposited on c-plane sapphire substrate with a N$_2$/(N$_2$+Ar) ratio of 25%) Right: fine scan spectrum of valence band structure for Y4

Figure 3.32 Left: High resolution XPS spectrum of Ga 3d core-level and valence bands for Kyma GaN templates Right: fine scan spectrum of valence band structure for Kyma GaN templates

Table 3.8 Binding energy of core-level peaks in the $ZnSnN_2$ and $ZnSnN_2$/GaN samples with different ratios of $N_2/(N_2+Ar)$

	Binding Energy(eV)					
	Zn 3d		Zn 2p 3/2		Ga 3d	
$N_2/(N_2+Ar)$	$ZnSnN_2$	$ZnSnN_2$/GaN	$ZnSnN_2$	$ZnSnN_2$/GaN	$ZnSnN_2$/GaN	GaN(Kyma template)
25%	9.86	9.79	1021.11	1020.84	19.80	20.34
50%	9.91	9.63	1021.11	1021.18	19.56	20.34

According to equation 3-5 and the core-level peaks of Ga 3d and Zn 3d, valence band offsets of $ZnSnN_2$/GaN samples with different $N_2/(N_2+Ar)$ ratios are obtained 1.46 eV and 0.85 eV, respectively(Table 3.9). Correspondingly, the conduction band offsets(CBO) between $ZnSnN_2$ and GaN are calculated to be -0.07eV and 0.52eV after taking into account the band gaps of GaN and $ZnSnN_2$ materials (The value of GaN template band gap is 3.3 eV, taken from Kyma technology).

87

Table 3.9 Valence band offsets (VBO) of $ZnSnN_2$/GaN heterojunctions calculated using core-level peaks of Ga 3d and Zn 3d

		VBO (eV)
$N_2/(N_2+Ar)$		Zn 3d
25%	Ga 3d	1.46
50%	Ga 3d	0.85

The energy band alignment for the ZnSnN2/GaN heterojunction with different $N_2/(N_2+Ar)$ ratios are shown in Figure 3.33. In the case of low N_2 content in the total reactive gas mixture (25%), a type-II heterojunction is found in the staggered arrangement [81]. This experimental result supports the calculated one from Ref [35]. We can achieve a better agreement of VBO between our experiments and A.Pauya's work by decreasing the $N_2/(N_2+Ar)$ ratio. On the other hand, we find that a straddled type-I alignment between $ZnSnN_2$ and GaN is attained by increasing the $N_2/(N_2+Ar)$ ratio to 50%. A Schottky-like barrier height is calculated to be 1.09eV. More details about the calculation of VBO and Schottky barrier height can be found in Appendix C.

The type-I alignment of $ZnSnN_2$/GaN heterojunctions can be applied as a quantum well structure to confine the both holes and electrons in the $ZnSnN_2$ side. Based on this structure, a novel "2d gas" channel is estimated to form. Also, relying on type-I structure, some optoelectronic devices such as LED, which is operated based on the mechanism of recombination between electrons and holes, can be fabricated. Additionally, as a type-II structure, holes are confined into the $ZnSnN_2$ layer, and electrons will be confined into the GaN layer. This structure can be used for separating the electrons and holes spatially. One example is heterojunction-based solar cells such as ZnO/CIGS solar cells.

So, from these interesting findings, we claim that by carefully controlling the amount of anion incorporation, different band alignments of ZnSnN$_2$/GaN heterojunctions can be formed. This can open up a new avenue for multiple applications in optoelectronic devices based on ZnSnN$_2$/GaN heterojunctions.
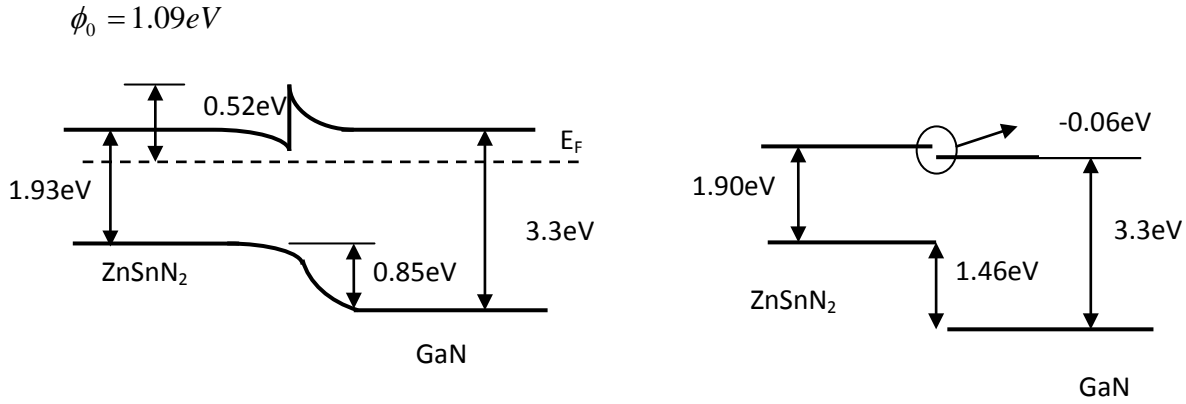
$$\phi_0 = 1.09eV$$

Figure 3.33 Schematic of energy band diagrams for the ZnSnN$_2$/GaN heterojunction with different N$_2$/(N$_2$+Ar) ratios, Left: 50% , Right: 25%

3.3.3 Electrical characteristics of diodes with a structure ZnSnN$_2$/GaN heterojunctions

The diodes based on ZnSnN2/GaN heterojunctions with different N$_2$/(N$_2$+Ar) ratios were fabricated, using the standard process for semiconductor devices mentioned in section 3.3.1. the current-voltage(I-V) and the capacitance-voltage (C-V) measurements are performed with a probe station connected to a HP 4145B semiconductor parameter analyzer and an Agilent 4284A precision LCR meter(20Hz-1MHz), respectively. The data were acquired and processed ,using the Metric ICS software(UCLA Microlab).

Figure 3.34 indicates the I-V characteristics of the diodes with $ZnSnN_2$/GaN heterojunctions grown at N_2/(N_2+Ar) ratios of 25% and 50%. In terms of a 25% N_2 content, the device shows ohmic characteristics, suggesting type-II band alignment between these two materials. It is noted that the series resistance extrapolated from the high injection region (from 0.6 eV to 1.0 eV) is higher than the resistance in the low injection region (0 to 0.6 eV). In the case of a N_2/(N_2+Ar) ratio of 50%, the hetero-junction between $ZnSnN_2$ and GaN exhibits Schottky-like behavior. The forward current (I_F) at a bias of 2.0 V is about 0.01 mA and the reverse current (I_R) is around 10^{-5} A, resulting in the ratio of I_F/ I_R around 10^3. This relative high ratio demonstrates that the diodes have good rectifying capabilities [81],[82]. The ideal factor n of this $ZnSnN_2$/GaN Schottky-like diode is 9.37, using the following equation for forward I-V characteristics of Schottky diode [81],[82],[83].

$$J = J_0 \exp(\frac{qV}{nkT})[1 - \exp(\frac{-qV}{kT})]$$

$$n = \frac{q}{kT}(\frac{dV}{d(\ln I)})$$

(3-6)
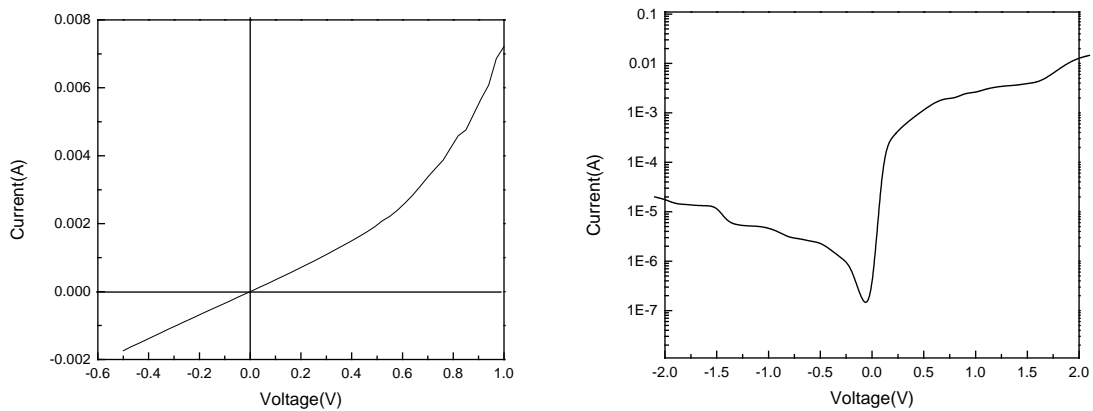
Figure 3.34 I-V characteristics of the diode with a structure of $ZnSnN_2$/GaN heterojunction with different N_2/(N_2+Ar) ratios, Left: 25% (I-V curve in linear scale) , Right: 50% (I-V curve in semi-log scale)

The left figure in Figure 3.35 shows the C-V characteristics of the diode with a structure of ZnSnN$_2$/GaN heterojunctions with N$_2$/(N$_2$+Ar) ratios of 50%. The capacitance–voltage (C–V) measurements were acquired with a high frequency of 100 khz to avoid the contribution from the interface state charges at low frequency to the diode's capacitance [84]. The junction capacitance (depletion capacitance) per unit area of our schottky-behavior diode is obtained, using the following equations for conventional n-type schottky diodes[82],[83],[84]:

$$\frac{C}{A} = \sqrt{\frac{q\varepsilon_s N}{2(V_{bi} - V - kT/q)}}$$

$$(C/A)^{-2} = \frac{2}{q\varepsilon_s N}(V_{bi} - V - kT/q) \tag{3-7}$$

C is the junction capacitance, A is the junction area of ZnSnN2/GaN structure (here, A=3.14x10^{-4} cm^2), ε_S is the dielectric constant ($\varepsilon_S(GaN) = 9\varepsilon_0$ from ref.[85]), V is the applied bias, V_{bi} is the built-in potential, and N is the net carrier concentration(here the net donor concentration). The plot of (C/A)$^{-2}$ versus applied bias is shown on the right side of Figure 3.35. The linear relationship between (C/A)$^{-2}$ and applied voltage suggests a constant carrier concentration [85]. The net carrier concentration N can be extracted from the slope of (C/A)$^{-2}$-V curve and the built-in potential (V_{bi}) is determined by linearly extrapolating from this curve to the voltage axis.

$$N = \frac{2}{q\varepsilon_S}$$

$$V_{bi} = V_0 + \frac{kT}{q} \tag{3-8}$$

Here, V$_0$ indicates the value of applied bias corresponding to the zero point of (C/A)$^{-2}$. Therefore, the Schottky barrier height at zero bias of our schottky-like diode is equal to:

$$\phi_0 = V_{bi} + \frac{kT}{q}\ln(\frac{N_c}{N})cm^{-3} \qquad (3\text{-}9)$$

Where, Nc is the effective density of states in the conduction band ($N_C(GaN) = 2.3 \times 10^{18}\,cm^{-3}$

based on effective mass m=0.2m$_0$ at room temperature from ref.[82]). Then, the net carrier

concentration N is $5.6 \times 10^{15}\,cm^{-3}$. Finally, The schottky barrier height between ZnSnN$_2$ and GaN

is calculated to be 1.11eV according to the equation (3-9). The result is consistent with the

barrier height obtained from our XPS analysis ($\phi_0 = 1.09eV$).
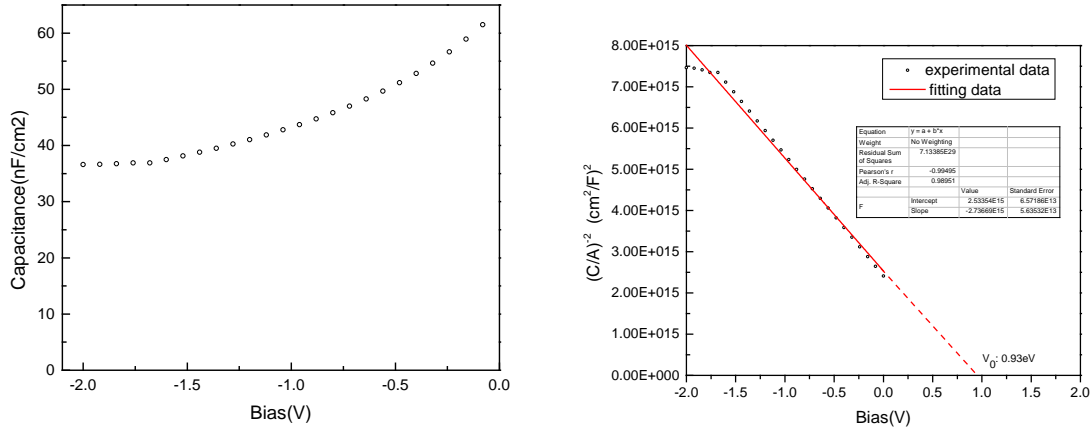
Figure 3.35 Left: C-V characteristics of the diode with a structure of ZnSnN$_2$/GaN heterojunction with the N$_2$/(N$_2$+Ar) ratio of 50%, measured at the frequency of 100 KHz, Right: The plot of (C/A)$^{-2}$ versus bias (dotted line indicates the extrapolation for the V$_0$)

3.3.4 Contact resistances of ZnSnN$_2$ films

In this work, we investigated the contact resistance between ZnSnN$_2$ films and ohmic

metal contacts (a stack layer of 20nm Ti, 120nm Al, 40nm Ni, and 50nm Au), using standard

transmission line measurement (TLM) technique [26]. Figure 3.36 shows the sketch of the TLM

method for calculating the contact resistances between semiconductors and metal contacts.
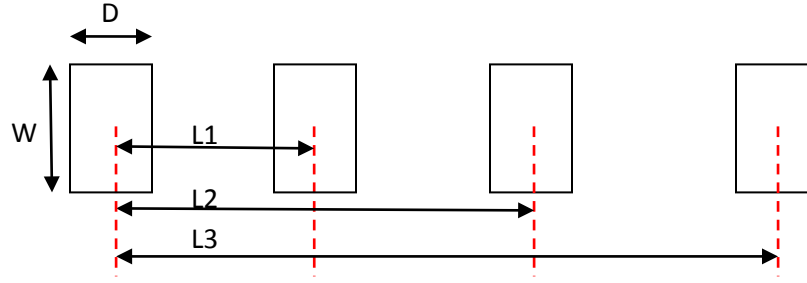
Figure 3 36 A sketch of transmission line measurement

Here, the semiconductor resistance R_{total} is defined as the following equation:

$$R_{total} = 2R_C + R_S = 2R_C + \rho_S \frac{L_S}{A_S}$$ (3-10)

R_c is the contact resistance between a metal and a semiconductor and Rs is the resistance of the semiconductor. Then, when the total resistance is measured and plotted according to the different length L_S, the contact resistance Rc can be obtained from the graph by extrapolating to the point at $L_S=0$, namely,

$$2R_C = \lim_{Ls \to 0} R_{total}.$$ (3-11)

And specific contact resistivity is defined as:

$$\rho_C = R_C * W * D$$ (3-12)

Here, W is 200um and D is 100um in our experiments. The current-voltage (I-V) characteristics of metal contacts to ZnSnN$_2$ films were measured by a probe station connected to a HP 4145B

semiconductor parameter analyzer.The I-V data were acquired and processed using the Metric ICS software (UCLA Microlab).

Figure 3.37 compares the contact resistance between $ZnSnN_2$ films and metal contacts, to the resistance between GaN templates and the same metal contacts. The contact resistance of metal contacts to $ZnSnN_2$ films, $R_c(ZnSnN_2)$, is 4.55 ohm. In comparison, we also extrapolate the contact resistance of GaN templates, Rc(GaN), to be 137.48 ohm by using the same metal contacts(20nm Ti/120nm Al/40nm Ni/50nm Au). The specific contact resistivity of $ZnSnN_2$ and GaN are about 0.0027 ohm-cm^2 and 0.082 ohm-cm^2, respectively. It is necessary to point out that the value of $R_c(GaN)$ was achieved by a post-annealing process after the device fabrication. This process was performed by using rapid thermal annealing (RTA) at 830 ˚C for 1 minute, in the pure N_2 environment, which is a standard process to reduce the contact resistance for GaN-related devices. So, $R_c(ZnSnN_2)$, without any post-annealing treatment, is only 1/30 of $R_c(GaN)$. As we all know, contact resistance is one of the most important concerns in the design and fabrication of GaN-based transistors. A large contact resistance, definitely, inhibits the carrier transportation, reduces the carrier mobility and, even deteriorate the device performance. $ZnSiN_2$ and $ZnGeN_2$ have been regarded as promising materials for the emitters of SiC HBTs. The lowest value of specific contact resistivity (ρ_C) between these two materials and metal contacts was 5.3×10^{-7} ohm-cm^2, achieved after post-annealing for 10 seconds at 800˚C [26]. As the smallest band gap material in the Zn-IV-N_2 group semiconductors, $ZnSnN_2$ also shows it's potential ability to become a qualified candidate for the emitter layer in GaN-based HBTs (heterojunction biplar transistors). As a preliminary result, the specific contact resistivity of $ZnSnN_2$, without any post-annealing treatment, is much lower than the one of GaN, although this numerical value is still higher than the reported value of $ZnGeN_2$. We believe that the lower

contact resistance of ZnSnN$_2$ can be obtained by using the adequate post-annealing strategy and optimizing the process of device fabrication.
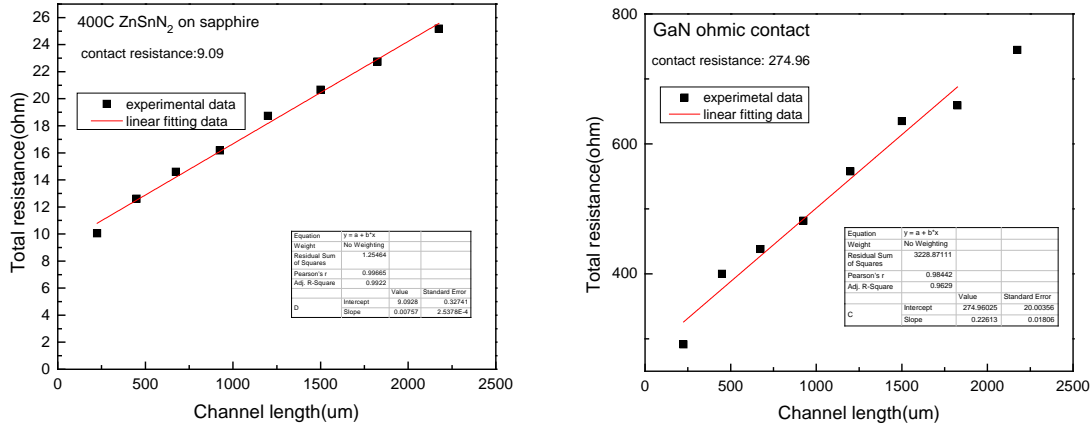
Figure 3.37 Left: total resistance of metal contacts to a 400nm thick ZnSnN$_2$ layer deposited on a c-plane sapphire substrate at a substrate temperature of 400˚C and with a N$_2$/(N$_2$+Ar) ratio of 50%, Right: total resistance of metal contacts to a GaN template from Kyam technology

3.4 Conclusion

In conclusion, we have successfully synthesized ZnSnN$_2$ thin films on c-plane sapphire substrates and GaN templates by the reactive RF-magnetron sputtering method. The properties of ZnSnN$_2$ films have been fully characterized using various kinds of techniques including X-ray diffraction (XRD), Raman spectroscopy, X-ray photoemission spectroscopy (XPS), scanning electron microscopy (SEM), atomic force microscopy (AFM), Hall effect measurement, UV-Vis-NIR spectrometer, etc. By optimizing the growth conditions such as substrate temperatures and N$_2$ contents in the mixture of total reactive gas, ZnSnN$_2$ thin films with an average grain size larger than reported results have been obtained. Additionally, for the first time, the valence band

structure of $ZnSnN_2$ has been investigated by XPS analysis. The result is consistent with our calculated density of states (DOS). The vibrational modes of $ZnSnN_2$ are also studied by Raman spectroscopy. We have found that our Raman spectra are comparable to the phonon density of states of $ZnSnN_2$ materials calculated by T.R. Paudel et al [62]. In terms of the band alignment between $ZnSnN_2$ and GaN, we have surprisingly found that the $ZnSnN_2$/GaN heterojunctions can be tuned from type-II structure to type-I structure by carefully controlling the incorporation of nitrogen anions during the films' growth. This result is estimated to open a new avenue for versatile applications in optoelectronic devices based on $ZnSnN_2$/GaN heterojunctions. Based on this novel concept, the first schottky-behavior diode with a structure of $ZnSnN_2$/GaN heterojunctions has been successfully fabricated, using the standard fabricating process for semiconductor devices. Standard electrical measurements such as C-V measurements reveal the height of the schottky barrier at the interface between $ZnSnN_2$ and GaN, as confirmed by XPS measurement for band alignment of $ZnSnN_2$/GaN heterojunctions. Finally, the contact resistance between metal contacts and $ZnSnN_2$ has been extracted, using the standard transmission line measurement (TLM) method). A preliminary result shows that the specific contact resistivity of $ZnSnN_2$, without any post-annealing treatment, is much lower than the one of GaN, suggesting that $ZnSnN_2$ can be applied as an emitter layer in GaN-based HBTs in the future.

Chapter 4 Preparation, characterization and device applications of zinc tin oxynitride thin film materials

This chapter discusses the preparation, characterization, and related device applications of zinc tin oxynitride thin films.

4.1 Background and objective

Recently, amorphous transparent oxide semiconductors such as amorphous indium gallium zinc oxide (IGZO) have been studied and developed as active channel materials, pointing to a new way to generate high mobility thin film transistors (TFTs)[86],[87]. These TFT arrays are widely applied for active matrix displays, including AMLCD and AMOLED [88],[89]. However, there are still some drawbacks in terms of IGZO materials. First, indium and gallium are rare elements in the earth and not environmentally friendly. Second, due to the large band gap, IGZO materials cannot be effectively used as photo-sensors for visible light [90]. Third, because of the existence of donor-like oxygen vacancies within their wide band gaps, amorphous IGZO materials are photo-conductive when light illumination and negative gate bias are applied, which results in a light-induced threshold voltage instability [91]. Therefore, in order to solve these problems, several types of zinc based oxynitride semiconductors have also been studied over the past decades. In 1998, M. Futsuhara et al. proposed a method of preparing polycrystalline zinc oxynitride semiconductors and investigated the optical properties of this kind of thin film [92]. Then, in 2009, Yan Ye et al. reported that amorphous zinc oxynitrde

materials with high hall mobility were produced by controlling a reactive sputtering process [93]. In the last two years, Hyun-Suk Kim et al. improved the mobility and stability of nanocrystalline ZnON thin films and demonstrated a TFT structure for the application of high-performance photo-sensors in next-generation flat panel displays [94],[95].

In this study, a kind of novel zinc based oxynitride material, namely, zinc tin oxynitride has been prepared and characterized. By carefully adjusting the ratio of anions as well as cations, a wide range of band gaps from 1.83eV to 2.7 eV and a relatively high mobility have been achieved. Additionally, a good stability of ZnSn(ON) under light illumination is estimated from previous research reports on zinc oxynitride and zinc tin oxide materials. For the first time, a TFT structure, based on zinc tin oxynitride active channel materials has been designed and fabricated. Preliminary results show that these devices feature the fundamental characteristics of transistors, suggesting that zinc tin oxynitride materials are a promising candidate as next-generation oxynitride channel layers.

4.2 Preparation of zinc tin oxynitride thin films

In this study, polycrystalline ZnSn(ON) or $Zn_xSn_{1-x}N_yO_{1-y}$ thin films were deposited on corning 1737 glass substrates and SiO_2/Si wafers using the reactive radio frequency (RF) magnetron sputtering system (ULVAC JSP 8000). A 4-inch diameter zinc tin alloy ($Zn_{0.75}Sn_{0.25}$, 99.995% purity, ACI alloy Inc.) was used as the sputtering target and the substrates were mounted on a rotating metal plate at a horizontal distance of 15cm from the target. The RF sputtering power was set to 300W, and the substrate temperature was fixed at 75 $^{\circ}$C. The reactive

sputtering gas is the mixture of pure N_2, Ar and O_2 with plasma activation. The composition of ZnSn(ON) thin films was controlled by carefully tuning the partial pressure inside the sputtering chamber. During deposition, the O_2 partial pressure was adjusted by O_2 flow rate (0.5–5 sccm) while the flow rates of N_2 and Ar were fixed to 40 sccm and 4 sccm, respectively. The base pressure of the sputtering chamber was in the low range of 10^{-6} Torr (1.0×10^{-6} — 3.0×10^{-6} Torr). Prior to the films deposition, a pre-sputtering process was performed for 20 minutes with pure Ar gas atmosphere in order to clean the surface of the target. The film thicknesses were obtained by Dektak profilometry after deposition.

4.3 Characterization of zinc tin oxynitride thin films

4.3.1 Crystal structure

The thin films' x-ray diffraction (XRD) measurements ($\theta - 2\theta$ geometry) were performed using a PANalytical X'Pert Pro x-ray powder diffractometer with a Cu Kα radiation source and a sealed proportional detector equipped with X'Pert highscore software.

Figure 4.1 shows the impact of oxygen contents in the mixture of total reactive gas on the crystal structure of ZnSn(ON) films. With the increased incorporation of O_2, the main characteristic peaks of $ZnSnN_2$ such as (002) and (121) peaks gradually disappeared. On the contrary, the characteristic peaks of $Zn(OH)_2$ (JCPDS #76-1778) were more dominant. Additionally, a peak at 43.68° was found in the $\theta - 2\theta$ spectra with different O_2 flow rates. This peak is related to the (332) plane of Zn_3N_2 (JCPDS #88-0618). This result indicates that ZnSn(ON) contains $ZnSnN_2$, $Zn(OH)_2$ as well as a small amount of Zn_3N_2. The average grain

99

sizes of ZnSn(ON) films with different O_2 flow rates are around 10 to 30nm, using Scherrer's equation.

Δ Zn_3N_2 (332) 43.68   * $Zn(OH)_2$ # $Zn(OH)_2$ or $ZnSnN_2$
$Zn(OH)_2$ JCPDS # 76-1778 Zn_3N_2 JCPDS #88-0618
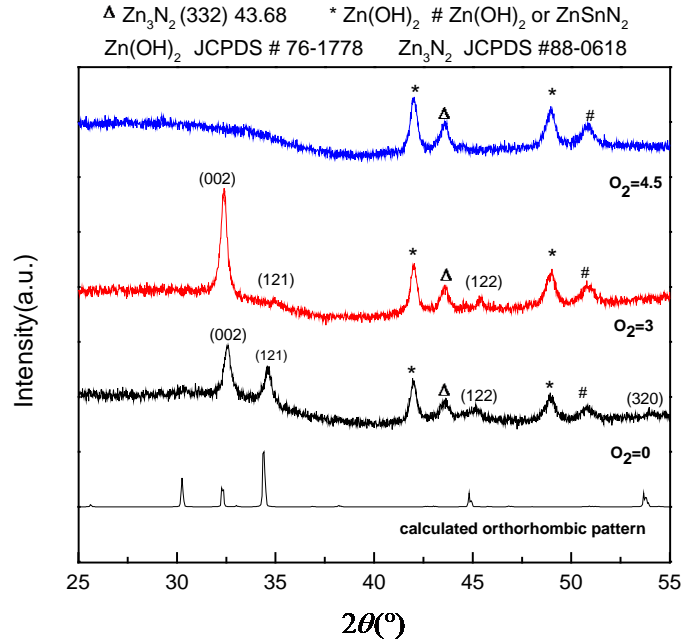
Figure 4.1 XRD patterns with a $\theta - 2\theta$ configuration for as-deposited films with different O_2 flow rates at a substrate temperature of 75˚C (Δ from Zn $(OH)_2$, and * peaks from Zn_3N_2, # peaks from $ZnSnN_2$ or $Zn(OH)_2$)

4.3.2 Chemical bonding, composition and valence band structure

Chemical bonding states, surface composition and the valence band structure of ZnSn(ON) thin films were investigated by X-ray photoelectron spectroscopy (XPS). XPS measurements were performed using a Kratos XPS Axis Ultra DLD system, with the base pressure of 10^{-8} Torr. A monochromatic Al Kα (1486.6 eV) X-ray source was used for excitation and the spectra of fine scans were collected with a pass energy of 20 eV. The obtained XPS

100

spectra were referenced with respect to the surface C 1s line at the binding energy (BE) of 285.0 eV [75]. The spectra were curve-fitted by the commercial software package CasaXPS, with a mixture of Gaussian and Lorentzian line shapes based on a Shirley-type background.

Figure 4.2 to Figure 4.5 show the high resolution XPS spectra of O 1s line, Zn 2p 3/2 line, N1s line, and Sn 3d 5/2 line of ZnSn(ON) thin films deposited at different O_2 flow rates. In Figure 4.2, it is shown that two peaks are observed at the spectra of O1s line. The peak located at 530.31eV is attributed to the O-Zn bonding in ZnSn(ON) films, suggesting the existence of $Zn(OH)_2$ in the films[76]. The binding energy of this peak is in agreement with the previously reported results [76],[77],[92],[96]. Another peak at 531.86eV is related to the O-H bonds reported at 531.95 or 532 eV [77],[92],[97]. This formation of O-H bonds results from the absorption of water molecules in air, indicating the strong affinity between ZnSn(ON) and water molecules[77],[92]. With the O_2 flow rates increased, the peak related to O-Zn bonding was much sharper. Additionally, the relative ratio of $I_{O\text{-}Zn}/I_{O\text{-}H}$ increased by increasing the O_2 flow rate, suggesting the population of O-Zn bonds increased in the films.
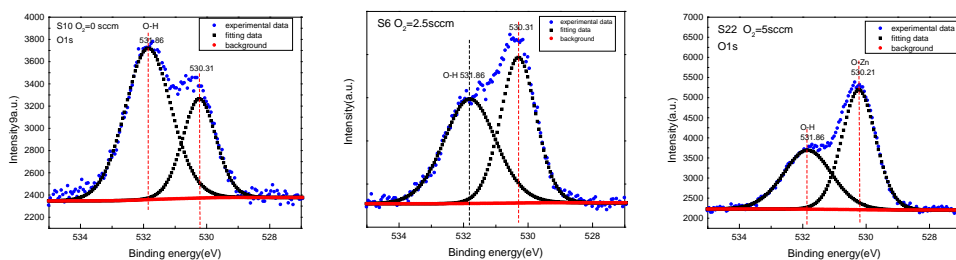
Figure 4.2 High resolution XPS spectra of O1s line for different O_2 flow rates; Left: 0 sccm, Middle: 2.5 sccm, Right: 5 sccm

Figure 4.3 demonstrates the XPS spectra of N1s line. The main N1s peak, located at the region between 396.41eV and 396.86 eV, is regarded as the combination of N-Zn bonding and N-Sn bonding in ZnSn(ON) films, indicating a significant chemical shift in comparison with the

N 1s peak of free amine (398.8eV). The chemical shift in this peak (1.94 to 2.39 eV) is smaller

than the chemical shift for Zn_3N_2 (3 eV)[76], suggesting that the N-metal (Zn and Sn) bonds of

ZnSn(ON) undergo less ionization than the N-Zn bonds in Zn_3N_2. A broad and short peak at

403.1eV or 404.26 eV became more obvious with the increased incorporation of O_2 in the total

reactive gas. This peak is estimated to correspond to the N-N bonding, suggesting the existence

of N-N bonds in ZnSn(ON) films [77],[98]. It is noted that a peak at 398.41 eV was found in the

ZnSn(ON) films with an O_2 flow rate of 5 sccm. This peak is related to the N-H bonds reported

at 398.3 eV [76]. It is possible that the hydrolysis of $ZnSnN_2$ with air exposure leads to the

formation of N-H bonds.
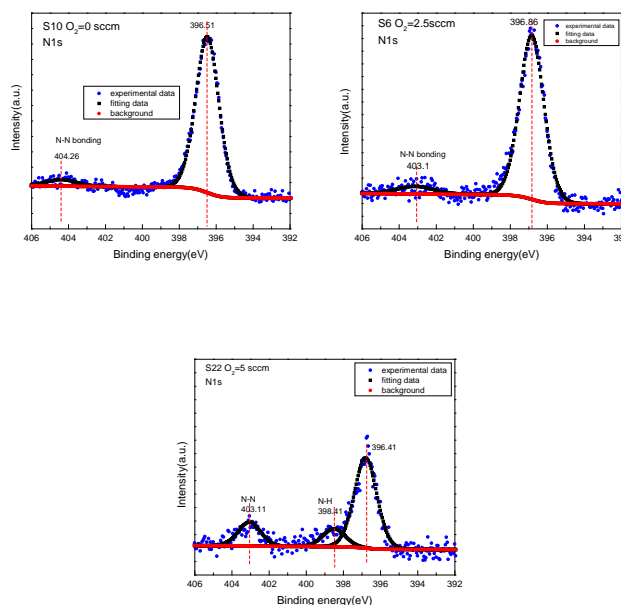
Figure 4.3 High resolution XPS spectra of N1s line for different O_2 flow rates; Upper left: 0 sccm, Upper right: 2.5 sccm, Lower: 5 sccm

Figure 4.4 demonstrates the XPS spectra of Zn 2p 3/2 line at different O_2 flow rates. The

main Zn 2p 3/2 peak corresponds to the Zn-N bonds in ZnSn(ON) and the binding energy of this

Zn-N bonding slightly increased from 1021.51 eV to 1021.81 eV with the increase in the O_2

contents. The Zn 2p 3/2 peak in the films with a 5 sccm O_2 flow rate is close to the Zn 2p 3/2 peak in the Zn_3N_2 [76],[77]. This finding implies the co-existence of multiple phases in ZnSn(ON) films, as confirmed by our XRD analysis. In addition, a peak, located at the region between 1022.81eV to 1023.91eV was more pronounced by increasing the ratio of $O_2/(O_2+N_2+Ar)$ in the total reactive gas, which indicates that the increase of Zn-O bonds in the ZnSn(ON) films. Finally, a small peak of metallic Zn (1019.41eV or 1019.91eV) was observed in the spectra of medium O_2 flow rate and high O_2 flow rate, indicating the appearance of secondary phase of metallic Zn at the surface of films.
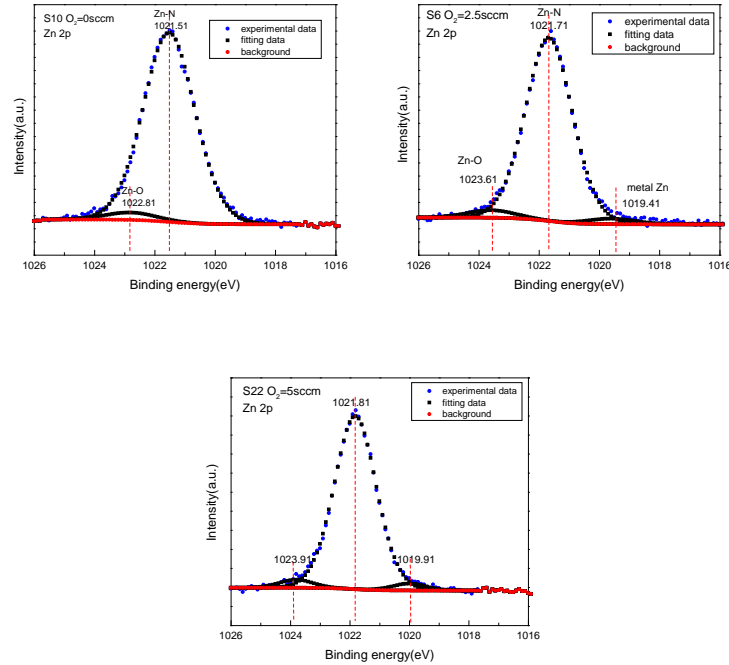
Figure 4.4 High resolution XPS spectra of Zn 2p 3/2 line for different O_2 flow rates; Upper left: 0 sccm, Upper right: 2.5 sccm, Lower: 5 sccm

Figure 4.5 shows XPS spectra of Sn 3d 5/2 line for different O_2 flow rates. The binding energy of this Sn-N bonding decreased slightly from 486.41 eV to 486.01eV with increasing O_2 flow rates.
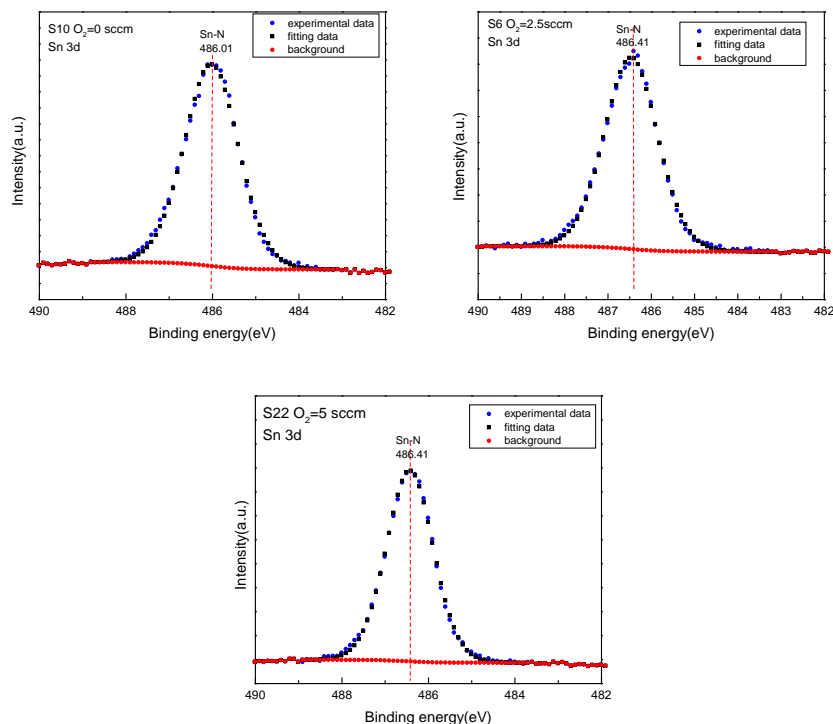
Figure 4.5 High resolution XPS spectra of Sn 3d 5/2 line for different O_2 flow rates; Upper left: 0 sccm, Upper right: 2.5 sccm, Lower: 5 sccm

The XPS spectra of the Zn Auger $L_3M_{4,5}M_{4,5}$ lines are shown in Figure 4.6. According to the literature, investigation of Zn $L_3M_{4,5}M_{4,5}$ Auger peaks can reveal more information about the chemical states of Zn elements. Here, the Auger L3 line is related to the deep Zn 2p core-level and the Auger $M_{4,5}$ line corresponds to the shallow Zn 3d core-level [95]. The XPS profile in kinetic enery clearly indicates that the surface of as-deposited films is composed of ZnSnN(991.34 eV), $Zn(OH)_2$ (987.64eV) [77], and ZnO (988.84 eV) [77],[97],[99] phases, with a slight contribution from ZnN phase(989.84 eV) [76],[77],[95] and metal Zn phase (993.29 eV). This result further indicates the multiphase co-existence in ZnSn(ON) films, supporting the claim

based on our XRD analysis. It is noted that the phenomenon of multiphase co-existence is also found in Zn(ON) films [95].
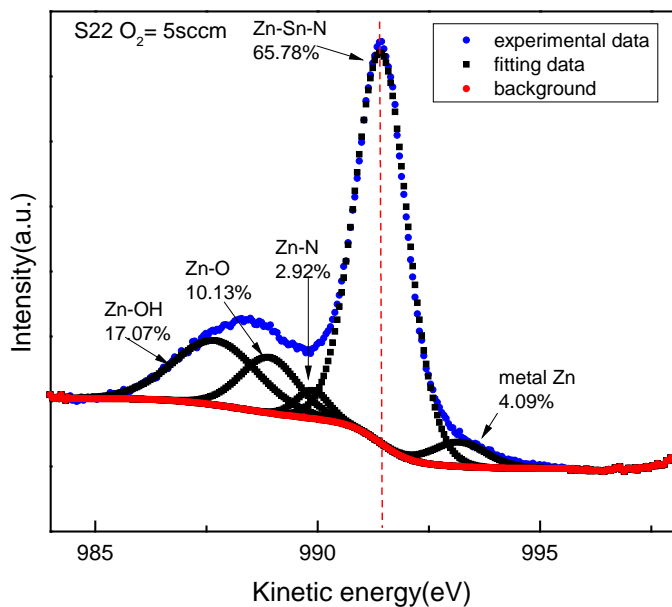
Figure 4.6 High resolution XPS spectra of Zn Auger $L_3M_{4,5}M_{4,5}$ line of ZnSn(ON) films with an O_2 flow rate of 5 sccm

The surface composition is obtained from XPS measurements. The compositional data is summarized in the Table 4.1. A Zn-rich surface is observed in the films with different O_2 contents. The lower ratio of (Zn+Sn)/(N+O) is obtained at an oxygen flow rate of 2.5 sccm, which is close to the stoichiometric ratio of cation/anion.

Table 4.1 Summary of surface compositions of ZnSn(ON) samples with different O_2 flow rates analyzed by XPS

O_2 flow rate (sccm)	Element composition (atomic %)				Relative ratio		
	Zn	Sn	N	O	Zn/Sn	O/N	(Zn+Sn)/(N+O)
0	36.8	19.4	29.9	13.8	1.88	0.46	1.28
2.5	32.5	21.3	19.6	26.6	1.5	1.35	1.17
5	38.4	20.7	11.9	28.9	1.85	2.42	1.45

Figure 4.7(a) indicates that the position of the valence band maximum(VBM) shifts upwards by 0.95eV with decreasing O_2 flow rates, which is mainly attributed to the fact that the oxygen anions feature lower p orbital energy than the nitrogen anions [94]. In addition, figure 4.7(b) shows that the amount of O_2 flow rate has obviously affected the intensity of the Auger peak related to Zn-O/Zn-OH bonding (988.6eV) in the Zn $L_3M_{4,5}M_{4,5}$ spectrum, which is confirmed by the compositional analysis of the films, namely, the ratio of O/N in the ZnSn(ON) thin films increased from 0.46 to 2.42 with the increase in O_2 flow rates.
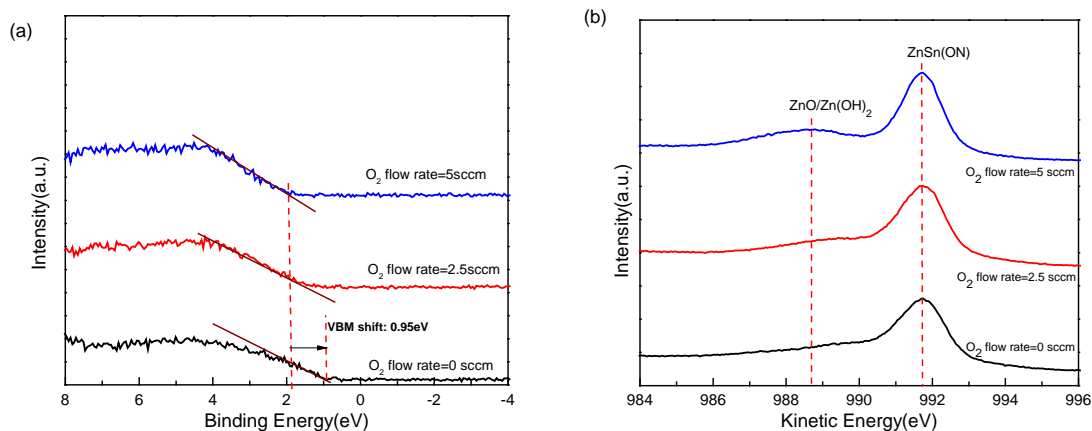
Figure 4.7 XPS spectra of ZnSn(ON) thin films prepared by different O_2 flow rates (a) valence band structure of ZnSn(ON) (b) Auger transition of Zn atom

4.3.3 Surface morphology

Atomic force microscopy (AFM) was employed to investigate the properties of surface morphology of ZnSn(ON) thin films. AFM images were obtained from a Quesant Q-scope atomic force microscopy (scanning probe microscopy).

Figure 4.8 shows the AFM images of ZnSn(ON) thin films deposited with different O_2 flow rates. With the increased incorporation of O_2, the surface roughness of films, correspondingly, increased from 1.1nm to 2.1nm, evaluated by root mean square (RMS) roughness. One possible reason for this is that the incorporation of $Zn(OH)_2$ leads to the larger RMS value.
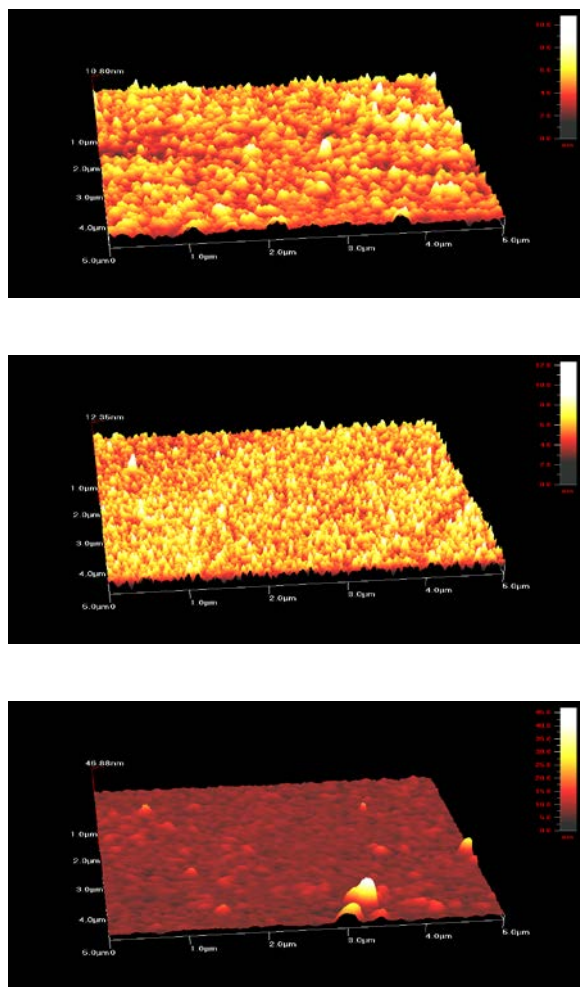
Figure 4.8 3D AFM images of ZnSn(ON) thin films deposited with various O_2 flow rates, 0 sccm (upper), 3 sccm (middle), and 5 sccm (lower)

4.3.4 Electrical properties

The electrical properties of ZnSn(ON) films such as carrier concentration, resistivity and mobility were characterized by Hall-effect measurements and four-probe resistivity measurements. Our room temperature Hall measurements were operated in a DHE-21 Hall system from SES Instruments Pvt. Ltd, using a standard four point Vand der Pauw contact configuration [77]. The four-probe resistivity measurements were carried on a Omnimap RS 35C resistivity mapper to obtain the films' resistivity. Because a good ohmic contact is usually

required for electrical measurements including Hall and four-probe resistivity measurements, 120nm-thick Al films with Van der Pauw patterns were deposited on the $ZnSn(ON)$ samples as ohmic contacts before our measurements. The magnetic field's magnitude was set to 2700 G in Hall system. The investigated samples were grown on corning 1737 glass substrates and SiO_2/Si wafers with different oxygen flow rates. All samples are found to feature n-type semiconductor characteristics. For most samples, the carrier concentration is in the range of 10^{18} cm^{-3} to 10^{20} cm^{-3} and the resistivity is between 10^{-2} Ωcm and 3 Ωcm.

Figure 4.9 reflects the relationship between the electrical properties of $ZnSnN_2$ and different O_2 flow rates. The carrier concentration decreased as the O_2 flow rate was increased. One possible reason for this is that the population of oxygen vacancy point defects (V_O), which are the main n-type defects in $ZnSnN_2$ or ZnO, decreases with increased incorporation of oxygen. The Hall mobility increased with increasing O_2 flow rates. The highest mobility is 45cm^2 V^{-1}s^{-1}, coinciding with the lowest electron concentration of 1.63×10^{18} cm^{-3}.
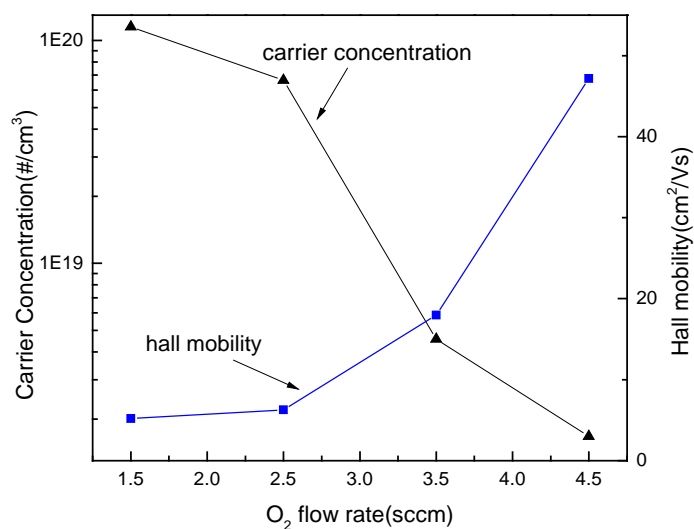
Figure 4.9 The effect of different O_2 flow rates on carrier concentration and Hall mobility of ZnSn(ON) thin films

4.3.5 Optical properties

The optical transmittance and reflectance of ZnSn(ON) thin films were collected using a Shimadzu UV-3101PC UV/VIS/NIR scanning spectrometer from a wavelength of 300nm to 1200nm. The absorption coefficient (α) of ZnSn(ON) was obtained based on the analysis of the film's transmittance as well as reflectance. The band gaps of ZnSn(ON) can be estimated based on the linear extrapolation from the curve of the square of the absorption coefficient (α^2) versus photon energy (hv) to the energy axis.

Figure 4.10 shows the optical properties of zinc tin oxynitride films produced by different O_2 flow rates (O_2 flow rate=0, 2.5 and 5 sccm). Based on the linear extrapolation from the square of the absorption coefficient ($\alpha2$) versus photon energy (hv), the band gaps of films are calculated to be 1.83eV, 2.08eV, and 2.7eV, respectively. The shift in band gap is about 0.87eV,

which is in a good agreement with the VBM shift. This result implies that the difference of VBM contributes to the variance in band gaps of ZnSn(ON) films.
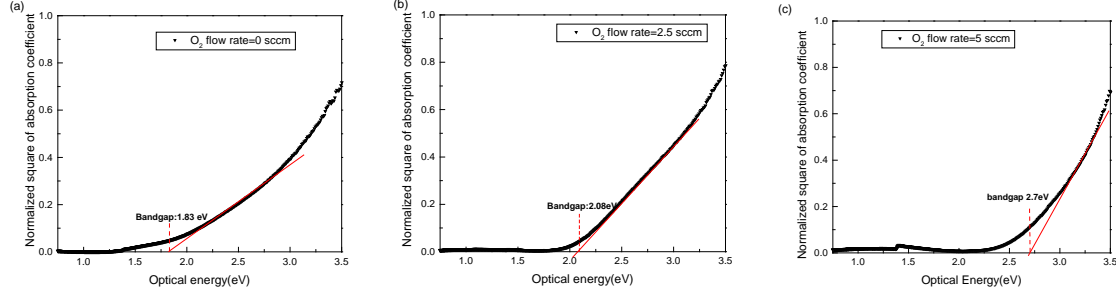
Figure 4.10 Optical properties of ZnSn(ON) thin films produced by different O_2 flow rates (a) 0 sccm (b) 2.5 sccm (c) 5 sccm

4.4 Device applications of zinc tin oxynitride thin films: TFT based on ZnSn(ON) materials

4.4.1 Device fabrication

In this study, ZnSn(ON) TFTs with an inverted bottom-gate and top-contact configuration [94] were fabricated on SiO_2/Si wafers using the standard semiconductor fabrication process. The device structure was shown in Figure 4.11. Here, highly p-type doped Si wafers served as the bottom-gate. First, Si wafers were cleaned using acetone, IPA and DI water sequentially. Then, wafers were baked on the hot plate at 150 ˚C for 1 minute to remove the residual water molecules on the surface. Then, 100nm thick SiO_2 films, working as gate dielectric layers, were grown on top of silicon wafers by dry oxidation. Subsequently, The ZnSn(ON) active channel layers with a thickness of 40nm were deposited on the wafers by using the reactive RF-magnetron sputtering method. Finally, a metal stack of 20 nm Ti, 120 nm Al, 40 nm Ni, and 50 nm Au was deposited by E-beam evaporation, acting as the source-drain electrodes.

111

Stainless steel shadow masks were used to define the channel length and channel width (channel length/width=200/1000 μm).The fabricated transistors were post-annealed in air for 10 minutes at 200 ˚C.

Metal contact: 20nm Ti/120nm Al/40nm Ni/50nm Au

50nm ZnSn(ON) active channel layer

100nm thermally grown SiO$_2$

Highly doped p-type Si wafer
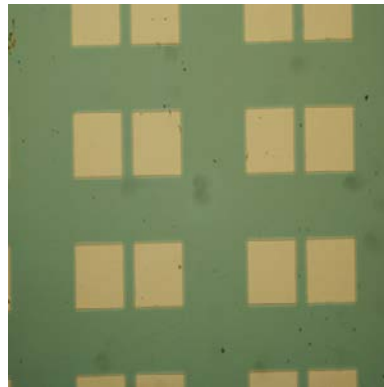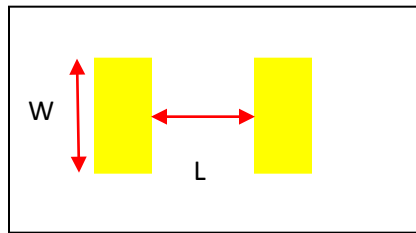
Figure 4.11 Upper: cross-section of the inverted structure of TFTs based on ZnSn(ON) active channel layers, Middle: top-view of the TFTs, Lower: a top-view image of TFTs' configuration taken by a Nikon optical microscopy with 20X magnification

4.4.2 Electrical characteristics of ZnSn(ON) TFTs

The current-voltage (I-V) measurements were performed with a probe station connected to an HP 4145B semiconductor parameter analyzer. The data were acquired and processed using the Metric ICS software (UCLA Microlab).

Figure 4.12 shows the output characteristics of ZnSn(ON) TFTs. We found that source-to-drain current (I_{DS}) increased significantly with the increase in the source-to-drain voltage (V_{DS}) at a positive gate bias (V_G). This result suggests that the ZnSn(ON) channel layer is a kind of n-type semiconductor, as confirmed by our Hall measurements. In addition, a linear region, a non-linear region (pinch-off region), and a saturation region can be clearly distinguished in the V_{DS}-I_{DS} curve, indicating that the operation of our TFTs is in agreement with the standard model of field effect transistors[83],[94].
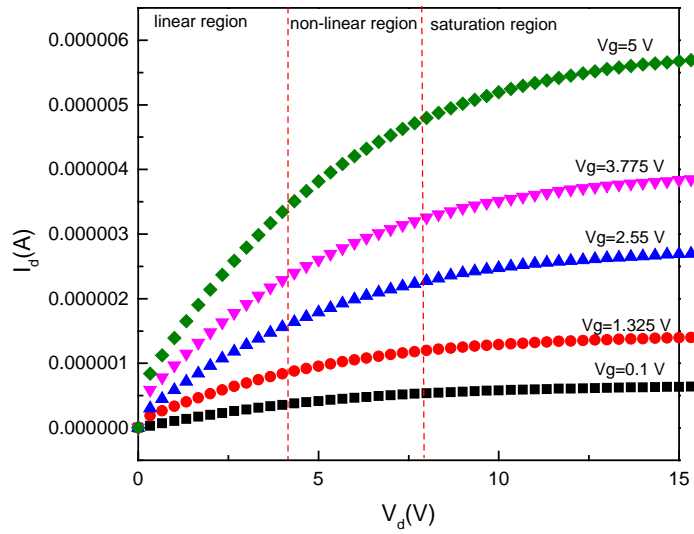
Figure 4.12 Output characteristics (I_D vs.V_D) of ZnSn(ON) TFTs acquired with different V_G

Figure 4.13 illustrates the transfer characteristics of ZnSn(ON) TFTs. The key device parameters such as threshold voltage (V_T), subthreshold swing (SS), and linear field-effect mobility μ_{linear} were calculated according to the gradual channel approximation and pinch-off approximation [83],[100]. The threshold voltage (V_T) and linear field-effect mobility μ_{linear} were extracted from the transfer curves in the linear region (V_{DS}=0.325V). The equation for long channel I-V characteristics in the linear region is listed as follows:

$$I_D = \mu \frac{W}{L} C_{ox} (V_G - V_T - \frac{V_D}{2}) V_D. \tag{4-1}$$

Here, C_{ox} is the capacitance of 100nm thick SiO_2 dielectric layer (C_{ox}=3.45x10^{-8}Fcm^{-2}). The extrapolated threshold voltage is 6.34 V. This positive value indicates that the ZnSn(ON) TFTs operate in enhancement mode [83],[94],[100]. The mean linear field-effect mobility (μ_{linear}) is calculated to be 39.6 cm^{2}V^{-1}s^{-1}, which is consistent with our Hall mobility of ZnSn(ON) films (45 cm^{2}V^{-1}s^{-1}). The subthreshold swing (SS) can be obtained from the inverse slope of the curve of log(I_D) vs.V_G (right side of Figure 4.13) and the relationship is listed as follows:

$$SS = \frac{dV_G}{d \log(I_D)}. \tag{4-2}$$

The calculated SS is around 1.86V/decade, which is far from the theoretical value of SS at room temperature for silicon-based transistors (60mV/decade). A relatively large SS was also found in Zn(ON) TFTs in recent reports[94]. The origin of this phenomenon is still unclear. The nitrogen

vacancy (V_N) point defects and poor interfaces between the channel layers and dielectric layers, possibly, contribute to a large SS [94],[101].
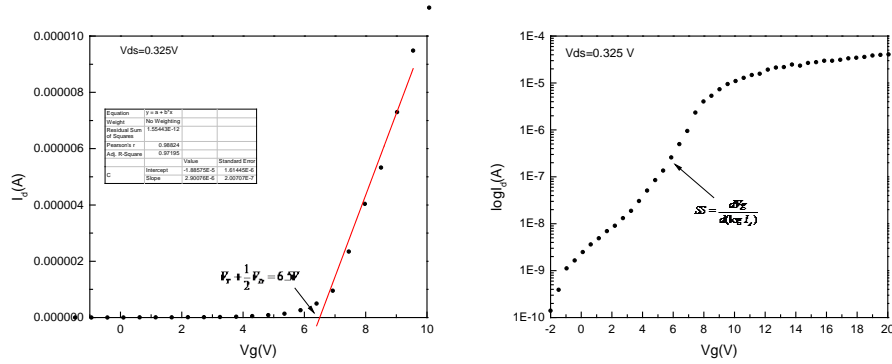
Figure 4.13 Left: transfer characteristics (I_D vs.V_G) of ZnSn(ON) TFTs with a V_D of 0.325V (I_D in linear scale to extract V_T, Right; transfer characteristics (I_D vs.V_G) of ZnSn(ON) TFTs with a V_D of 0.325V (I_D in logarithmic scale to deduce the subthreshold swing)

4.5 Conclusion

In conclusion, we have successfully synthesized zinc tin oxynitride, a kind of novel oxynitride material, on corning 1737 glass substrates and SiO_2/Si wafers by the reactive RF-magnetron sputtering method. The properties of ZnSn(ON) films have been fully characterized using various kinds of techniques including X-ray diffraction (XRD), X-ray photoemission spectroscopy (XPS), atomic force microscopy (AFM), Hall effect measurement, and UV-Vis-NIR spectrometry. By optimizing the O_2 content in the mixture of total reactive gas, ZnSn (ON) thin films with a Hall mobility of 45 cm^2 $V^{-1}s^{-1}$ and a carrier concentration of 1.63×10^{18} cm^{-3} have been obtained. Additionally, for the first time, thin film transistors (TFTs) based on ZnSn(ON) has been successfully fabricated, using the standard fabricating process for

115

semiconductor devices. The important device parameters including threshold voltage (V_T), subthreshold swing (SS), and linear field effect mobility (μ_{linear}) are extracted from transfer characteristics of TFTs in the linear region. The mean linear field effect mobility can reach to 39.6 cm^2 V^{-1}s^{-1}, which is in agreement with the Hall measurements. Preliminary results show that ZnSn(ON) is a promising candidate for next-generation oxynitride channel layers.

Chapter 5 Summary

In this thesis, a combinatorial study on zinc tin nitride and zinc tin oxynitride materials is presented. These properties of these materials such as crystal structures, lattice parameters, and electronic band configuration are investigated by theoretical calculations and experimental results. The devices based on $ZnSnN_2$ as well as ZnSn(ON) compounds have been fabricated and preliminary results indicate that these novel materials are some of the most potential candidates for future optoelectronic applications. Main achievements in this work are listed as follows:

(1)   We have successfully synthesized $ZnSnN_2$ thin films on c-plane sapphire substrates and (0001) GaN templates by the reactive RF-magnetron sputtering method. By optimizing the growth conditions including substrate temperatures and nitrogen contents in the mixture of total reactive gas, $ZnSnN_2$ thin films with an average grain size (133nm) larger than reported results have been obtained.

(2)   We have successfully grown zinc tin oxynitride, a kind of novel oxynitride material, on corning 1737 glass substrates and SiO_2/Si wafers by the reactive RF-magnetron sputtering method. By optimizing the O_2 contents in the mixture of total reactive gas, ZnSn (ON) thin films with a Hall mobility of 45 $cm^2 V^{-1}s^{-1}$ and a carrier concentration of 1.63×10^{18} cm^{-3} have been obtained.

(3)   We have presented a first-principles calculation of the crystal structure, lattice parameters, atomic positions, band structure and density of states of $ZnSnN_2$. The calculated lattice constants a, b and c are comparable to our experimental

results as well as previous calculations. In terms of the band structure, we find that the band gap obtained by PBE-GGA is underestimated significantly compared with experimental data from our work and reported by other groups. This is because the GGA method, intrinsically, is not suitable for the estimation of the excited-state properties such as the band gap. In addition, based on the careful analysis of the total and decomposed density of states of $ZnSnN_2$, we can predict that DOS of the valence band can be separated into 3 regions, namely, the N-2s orbital contributes to the DOS in the range around -15eV, the N-2p orbital dominates the range from 0 to -5 eV and hybridization between Zn-3d orbitals and N-2p orbitals construct the distribution of DOS in the range from -5 eV to -10 eV.

(4)   For the first time, the valence band structure of $ZnSnN_2$ has been investigated by XPS analysis. The result is consistent with our calculated density of states (DOS). The vibrational modes of $ZnSnN_2$ are also studied by Raman spectroscopy. We have found that our Raman spectra are comparable to the phonon density of states of $ZnSnN_2$ materials calculated by T.R. Paudel et al [62].

(5)   In terms of the band alignment between $ZnSnN_2$ and GaN, we have surprisingly found that the $ZnSnN_2$/GaN heterojunctions can be tuned from type-II structure to type-I structure by carefully controlling the incorporation of nitrogen anions during the films' growth. This result is estimated to open a new avenue for versatile applications in optoelectronic devices based on $ZnSnN_2$/GaN heterojunctions.

118

(6)   The first schottky-behavior diode with a structure of $ZnSnN_2$/GaN heterojunctions has been successfully fabricated, using the standard fabricating process for semiconductor devices. Standard electrical measurements such as C-V measurements reveal the height of the schottky barrier at the interface between $ZnSnN_2$ and GaN, as confirmed by XPS measurement for band alignment of $ZnSnN_2$/GaN heterojunctions.

(7)   The contact resistance between metal contacts and $ZnSnN_2$ has been extracted, using the standard transmission line measurement (TLM) method. A preliminary result shows that the specific contact resistivity of $ZnSnN_2$, without any post-annealing treatment, is much lower than the one of GaN, suggesting that $ZnSnN_2$ can be applied as an emitter layer in GaN-based HBTs in the future.

(8)   For the first time, thin film transistors (TFTs) based on ZnSn(ON) has been successfully fabricated, using the standard fabricating process for semiconductor devices. The important device parameters including threshold voltage (V_T), subthreshold swing (SS), and linear field effect mobility (μ_{linear}) are extracted from transfer characteristics of TFTs in the linear region. The mean linear field effect mobility can reach to 39.6 cm^2 $V^{-1}s^{-1}$, which is in a good agreement with the Hall measurements. Preliminary results show that ZnSn(ON) is a promising candidate for next-generation oxynitride channel layers.

Appendix A

The patterns and photo masks for schottky diodes and contact resistance measurements
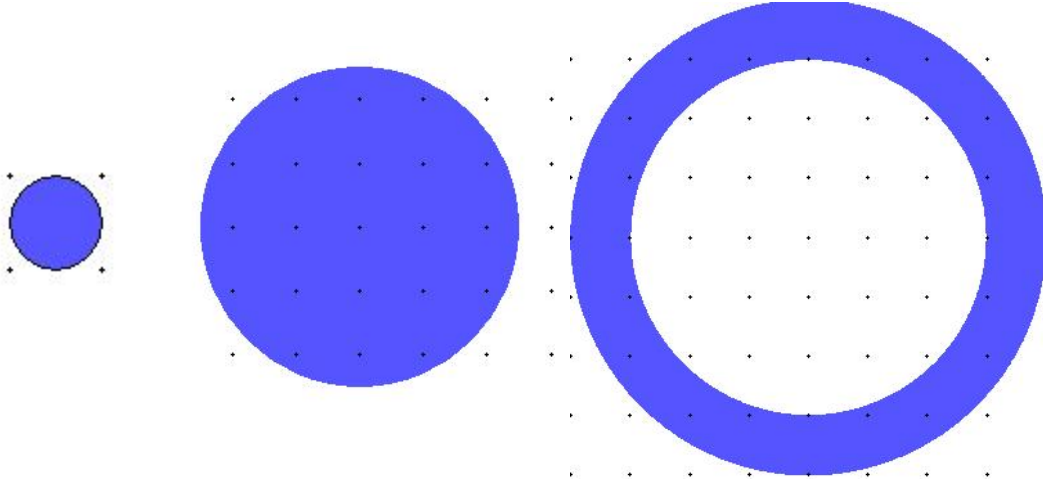
Figure A.1 Patterns of schotteky diodes , Left: inner gate contact, Middle: active area, Right: outer ohmic contact
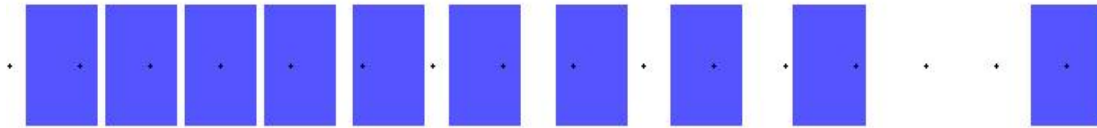
Figure A.2 Patterns of contact resistance measurements according to TLM method.
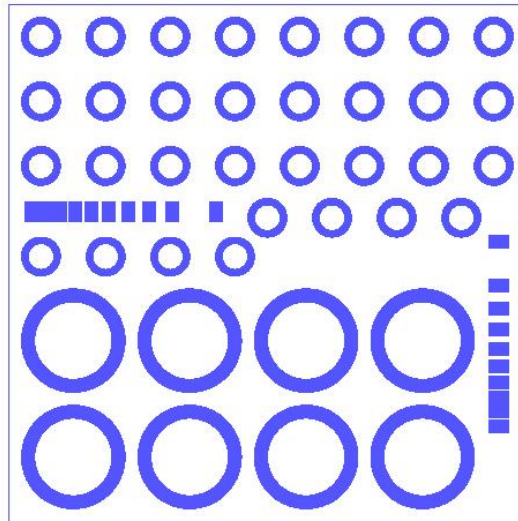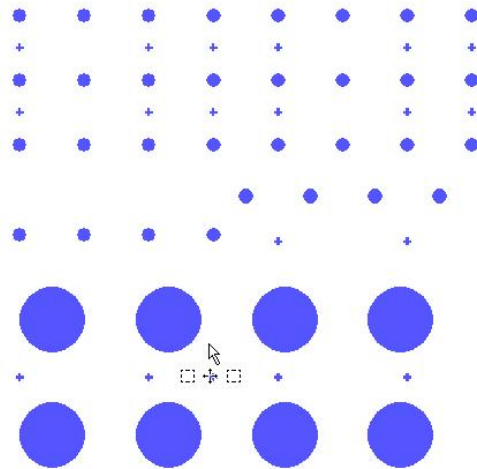
Figure A.3 Upper: the photo mask for the fabrication of outer ohmic contact and TLM patterns, Lower: the photo mask for the fabrication of active layer and inner gate contact patterns

These photo masks are designed by Dr. Jiechen Wu in our group.

Appendix B

Fabrication of diodes based on a structure of $ZnSnN_2$/GaN heterojuctions

1. We started with cleaning the 5um-thick undoped GaN template grown on c-plane sapphire substrates from Kyma technology by the sequence of buffered oxide etcher (BOE), 5% HCl, Acetone, IPA and DI water to remove the surface oxide and excess metals.

2. 20nm-thick $ZnSnN_2$ films were deposited on the GaN substrates to form the $ZnSnN_2$/GaN heterojunctions, using the reactive RF-magnetron sputtering method.

3. These samples were baked in hot plate at 150 ^{0}C for 2 minutes and left in the environment of HDMS for 10 minutes.

4. The 1.2 um-thick thin films of positive photo-resist (PR) were spun on the surface of our samples (SPR-700 was used as a positive PR in this work).

5. These wafers were exposed with a photo-mask to UV light, and developed (First photolithography is to form the active areas of $ZnSnN_2$/GaN heterojunctions).

6. Dry etch was employed to isolate the active areas of $ZnSnN_2$/GaN heterojunctions.

7. Photoresist was removed by PR-stripper.

8. Step 3 was repeated and 1.8 um-thick thin films of negative photo-resist (PR) were spun on the surface of our wafers (nLoff-2020 was used as a negative PR for our work).

9. Step 5 was repeated (Second photolithography is to form ohmic contact between GaN and metal).

10. 20nm Ti/120nm Al/40nm Ni/50nm Au were deposited on the wafers sequentially, using a E-beam evaporation method.

11. Step 7 and step 8 were repeated.

12. Step 5 was repeated (Third photolithography is to form ohmic contact between $ZnSnN_2$ and metal).

13. Step 10 was repeated.

14. Step 7 was repeated.

15. All the samples were post-annealed at 300-400˚C in N_2 environment for 5 minutes.

16. The fabrication of the diodes based on a structure of $ZnSnN_2$/GaN heterojunctions was completed.

Appendix C

Calculation of the valence band offset and the schottky-like barrier height by XPS

Valence band offset (VBO) between $ZnSnN_2$ and GaN is determined by the following equation:

$$VBO = [E_{CL}^{ZnSnN_2}(b) - E_V^{ZnSnN_2}(b)] - [E_{CL}^{GaN}(b) - E_V^{GaN}(b)] - [E_{CL}^{ZnSnN_2}(i) - E_{CL}^{GaN}(i)]$$

The subscript CL and V denote the BE for the core-level and valence band maximum (VBM). The notion (b) and (i) indicate the bulk and interface bind energies respectively.

Based on the set of Zn 3d and Ga 3d core-level, we can obtain the valence band offset at the interface between $ZnSnN_2$ and GaN according to the listed sequential equations.

(1) $N_2/(N_2+Ar)=25\%$

$$E_{CL}^{ZnSnN_2}(i) - E_{CL}^{GaN}(i) = 9.94eV$$
$$E_{CL}^{ZnSnN_2}(b) - E_V^{ZnSnN_2}(b) = 8.6eV$$
$$E_{CL}^{GaN}(b) - E_V^{GaN}(i) = 17.35eV$$
$$VBO = 1.19eV$$

(2) $N_2/(N_2+Ar)=50\%$

$$E_{CL}^{ZnSnN_2}(i) - E_{CL}^{GaN}(i) = 9.65eV$$
$$E_{CL}^{ZnSnN_2}(b) - E_V^{ZnSnN_2}(b) = 8.55eV$$
$$E_{CL}^{GaN}(b) - E_V^{GaN}(i) = 17.35eV$$
$$VBO = 0.85eV$$

The barrier height (ϕ_0) between ZnSnN$_2$ and GaN is calculatd by the following equations:

$$\phi_0(ZnSnN_2 / GaN) = \Delta E_C(ZnSnN_2 / GaN) + \Delta E_{CBM}^{ZnSnN_2}(i)$$

$$\Delta E_C(ZnSnN_2 / GaN) = E_g(GaN) - E_g(ZnSnN_2) - \Delta E_V(ZnSnN_2 / GaN)$$

$$\Delta E_{CBM}^{ZnSnN_2}(i) = E_g(ZnSnN_2) - \Delta E_{VBM}^{ZnSnN_2}(i)$$

$$\Delta E_{VBM}(ZnSnN_2) = E_{VBM}^{ZnSnN_2}(i) - E_F^{ZnSnN_2}(i)$$

Here, VBM and CBM refer to valence band maximum and conduction band minimum. $E_g, E_F, \Delta E_C, \Delta E_V$, and i denote the band gap, Fermi level, conduction band offset(CBO), valence band offset(VBO) and interface binding energy, respectively.

According to the above equations, the barrier height is calculated to be 1.09 eV.
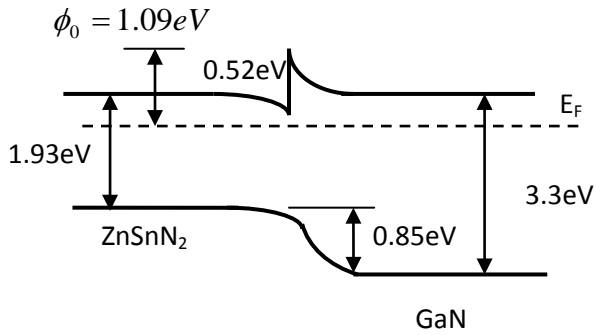
Figure 3.33 Schematic of energy band diagrams for the ZnSnN$_2$/GaN heterojunction with different N$_2$/(N$_2$+Ar) ratios Left: 50%

References

[1] S. Nakamura, S. J. Pearton , and G. Fasol , "The Blue Laser Diode: The Complete Story", 2nd ed. , Springer , Berlin 2000

[2] S. J. Pearton, C. R. Abernathy, F. Ren,"Gallium Nitride Processing for Electronics,Sensors, and Spintronics", Springer , New York , 2006

[3] N. Duxbury, U. Bangert, P. Dawson, E. J. Thrush, W. Van der Stricht, K. Jacobs, I. Moerman, "Indium segregation in InGaN quantum-well structures", Appl. Phys. Lett. , 76 , 1600, 2000

[4] Z. Liliental-Weber, D. N. Zakharov, K. M. Yu, J. W. Ager, W. Walukiewicz, E. E. Haller, H. Lu, W. J. Schaff, "Compositional modulation in $In_xGa_{1-x}N$: TEM and X-ray studies", J. Electron Microsc., 54 , 243, 2005

[5] http://www.nobelprize.org/nobel_prizes/physics/laureates/2014/press.html

[6] Gwinn, W. M. Qu, W. Bousquet, R. W. Price, H. Shines, C. J. Taylor, G. J. Waalkes, M. P. Morgan, D. L. (2014). "Macrophage Solubilization and Cytotoxicity of Indium-Containing Particles as in vitro Correlates to Pulmonary Toxicity in vivo", Toxicological Sciences. doi:10.1093/toxsci/kfu273

[7] T. R. Paudel and W. R. L. Lambrecht, "First-principles calculations of elasticity, polarization-related properties, and nonlinear optical coefficients in Zn-IV-N_2 compounds", Phys. Rev. B., 79(24) , 245205, 2009

[8] A. Punya, W. R. L. Lambrecht , and M. van Schilfgaarde, "Quasiparticle band structure of Zn-IV-N_2 compounds", Phys. Rev. B., 84, 165204, 2011

[9] "Rare Earth Elements—Critical Resources for High Technology, 087-02, U.S. Geological Survey Fact Sheet", [Online]. Available: http://pubs.usgs.gov/fs/2002/fs087-02/.

[10] W.C.Hsu, "Processing-Dependent Growth Mechanisms and Performance Improvement of Kesterite Solar Cells", PhD thesis, University of California at Los Angeles, 2014

[11] B.Gil, "III-Nitride Semiconductors and their modern devices", Oxford university press, UK, 2013, pp 519-585

[12] L. Lahourcade, N. C. Coronel, K. T. Delaney, S. K. Shukla, N. A. Spaldin, H. A. Atwater, "Structural and optoelectronic characterization of RF sputtered ZnSnN2", Adv. Mater. 2013, 25, 2562 -2566

[13] http://en.wikipedia.org/wiki/Gallium_nitride

[14] A.Boochun, W.R.Lambrecht, "First-principles study of the elasticity, piezoelectricity, and vibrational modes in $LiGaO_2$ compared with ZnO and GaN", Phys.Rev.B., 81, 235214, 2010

[15] S.Y.Chen, P.Narang, H.A.Atwater, L.W.Wang, "Phase Stability and Defect Physics of a Ternary ZnSnN2 Semiconductor: First Principles Insights", Adv. Mater., 26, 311-315, 2014

[16] M.Maunaye and J.Lang, "Preparation et Proprietes de ZnGeN$_2$", Mater. Res. Bull, 5:793, 1970

[17] M.Wintenberger, M.Maunaye, and Y. Laurent, "Groupe spatial et ordre des atoms de zinc et de germanium dans ZnGeN$_2$", Mat. Res. Bull., 1:1049, 1973

[18] T. Endo, Y. Sato, H. Takizawa , M. Shimada, "High pressure synthesis of new compounds, ZnSiN$_2$ and ZnGeN$_2$ with distorted wurtzite structure", J. Mater. Sci. Lett.,11 , 424 , 1992

[19] L.D.Zhu, P.H.Maruska, P.E.Norris, P.W.Yip and L.O.Bouthillette, "Epitaxial growth and structural characterization of single crystalline ZnGeN$_2$", MRS Internet J.Nitride Semicond. Res., 4S1:G3.8, 1999

[20] T.Misaki, K. Tsuchiya, D. Sakai, A.Wakahara, H. Okada, and A. Yoshida, "Growth and characterization of ZnGeN$_2$ by using remote-plasma enhanced metalorganic vapor phase epitaxy", Phys. Stat. Solidi., 0:188-191, 2000

[21] T. Misaki, A. Wakahara, H. Okada and A. Yoshia, "Optical properties of ZnGeN$_2$ epitaxial layer", Phys. Stat. Solidi (c), 0:2890-2893, 2003

[22] T. Misaki, A. Wakahara, H. Okada, and A. Yoshida, "Epitaxial growth and characterization of ZnGeN$_2$ by metalorganic vapor phase epitaxy", J.Cryst. Growth, 260:1049, 2004

[23] S. Kikkawa and H. Morisaka, "RF-sputter deposition of Zn-Ge nitride thin films", Solid State Commun., 112:513-515, 1999

[24] K. Du, C. Bekele, C. C. Hayman, J. C. Angus, P. Pirouz, and K .Kash, "Synthesis and characterization of $ZnGeN_2$ grown from elemental Zn and GE sources", J. Cryst. Growth., 310:1057, 2008

[25] B. P. Cook, H. O. Everitt, I. Avrutsky, A. Osinsky, A. Cai, and J. F. Muth, "Refractive indices of $ZnSiN_2$ on r-plane sapphire", Appl.Phys.Lett., 86(121906), 2005

[26] A. Osinsky, V. Fuflyigin, L. D. Zhu, L.D. Goulakov, J. W. Graff, and E. F. Schubert, " New concepts and preliminary results for SiC bipolar transistors: $ZnSiN_2$ and $ZnGeN_2$ heterojunction emitters", In 2000 IEEE/Cornell Conference on High Performance devices, page 168-172. IEEE, 2000

[27] A. Mintairov, J. Merz, A. Osinsky, V. Fuflyigin, and L. D. Zhu, "Infrared spectroscopy of $ZnSiN_2$ single-crystalline films on r-sapphire", Appl. Phys. Lett., 76(18): 2517, 2000

[28] T.R.Paudel, "Structure, Phonons and related Properties in $Zn\text{-}IV\text{-}N_2$ (IV=Si,Ge,Sn), ScN and Rare-Earth Nitrides", PhD thesis, Case Western Reserve University, 2008

[29] P.C.Quayle, K. L. He, J. Shan, and K.Kash, "Synthesis, lattice structure, and bandgap of $ZnSnN_2$", MRS Communications, 3:135-138, 2013

[30] N Feldberg, J. D. Aldous, W. M. Linhart, L. J. Phillips, K. Durose, P. A. Stampe, R .J. Kennedy, D. O. Scanlon, G. Vardar, R. L. Field, T. Y. Jen, R. S. Goldman, T. D. Veal, and S. M. Durbin, "Growth, disorder and physical properties of $ZnSnN_2$", Appl. Phys. Lett., 103, 042109, 2013

[31] W. Walukiewicz, J. W. Ager, K. M. Yu, Z. Liliental-Weber, J. Wu, S. X. Li, R. E. Jones, and J. D. Denlinger, "Structure and electronic properties of InN and In-rich group III-nitride alloys". J. Phys. D: Appl. Phys., 39, R83, 2006

[32] Y. Lee, H. Terashima, Y. Shimodaira, K. Teramura, M. Hara, H. Kobayashi, K. Domen, and M. Yashima, "Zinc germanium oxynitride as a photocatalyst for overall water splitting under visible light", J. Phys. Chem. C., 111(2):1042-1048, 2007

[33] F. Tessier, P. Maillard, Y. Lee, C. Bleugat, and K. Domen, "Zinc Germanium Oxynitride: Influence of the Preparation Method on the Photocatalytic Properties for Overall Water Splitting", J. Phys. Chem. C.,113:8526–8531,2009

[34] K. Takanabe, T. Uzawa, X. Wang, K. Maeda, M. Katayama, J. Kubota, A. Kudob, and K. Domen, "Enhancement of photocatalytic activity of zinc-germanium oxynitride solid solution for overall water splitting under visible irradiation", Dalton Trans., 45: 10055–10062, 2009

[35] A. Punya and W. R. L. Lambrecht, "Band offsets between $ZnGeN_2$, GaN, ZnO, and $ZnSnN_2$ and their potential impact for solar cells", Phys.Rev.B., 88,075302, 2013

[36] K. Capelle, "A Bird's-Eye View of Density-Functional Theory", arXiv:condmat/ 0211443v5 [cond-mat.mtrl-sci], Nov 18 2006

[37] P. Hohenberg and W. Kohn," Inhomogeneous electron gas", Phys.Rev.,136(3B): B864-B871, Nov 1964

[38] W. Kohn and L. J. Sham, "Self-consistent equations including exchange and correlation effects", Phys Rev., 140(4A): A1133-A1138, Nov 1965

[39] David S. Sholl, and Janice A. Steckel, "Density Funtional Theory: A Practical Introduction", Wiley Publication, USA, 2008, pp 1-35

[40] http://www.nobelprize.org/nobel_prizes/chemistry/laureates/1998/

[41] U. von Barth and L. Hedin, "A local exchange-correlation potential for the spin polarized case", J.Phys.C: Solid State Phys., 5:1629, 1972

[42] J. P. Perdew, A. Ruzsinszky, J. M. Tao, V. N. Staroverov, G. E. Scuseria, and G. I. Csonka, "Prescription for the Design and Selection of Density Functional Approximations: More Constraint Satisfaction with Fewer Fits", J.Chem. Phys., 123, 062201, 2005

[43] J. P. Perdew, J. A. Chevary, S. H.Vosko, K. A. Jackson, M. R. Pederson, D.J. Singh, and C. Fiolhais, "Atoms, molecules, solids, and surfaces: Applications of the generalized gradient approximation for exchange and correlation", Phys. Rev. B., 46 (11): 6671, 1992

[44] J. P. Perdew, K. Burke, and M.Ernzerhof, "Generalized gradient approximation made simple", Phys. Rev. Lett., 77(18): 3865-3868, 1996

[45] F. Litimein, B. Bouhafs, G. Nouet, and P. Ruterana, "Meta-GGA Calculation of the Electronic Structure of Group III-V Nitrides", Phys, Stat. Sol. B., 243, 1577, 2006

[46] J. P. Perdew, J. Tao, and S. Kümmel, "in Recent Advances in Electron Correlation Methodology" , edited by A. K. Wilson and K. A. Peterson, ACS Books, Washington, DC, 2004

[47] J. P. Perdew, S. Kurth, A. Zupan, and P. Blaha, "Accurate Density Functional with Correct Formal Properties: A Step Beyond the Generalized Gradient Approximation", Phys. Rev. Lett. , 82, 2544, 1999

[48] J. Tao, J. P. Perdew, V. N. Staroverov, and G. E. Scuseria, "Climbing the Density Functional Ladder: Nonempirical Meta–Generalized Gradient Approximation Designed for Molecules and Solids", Phys. Rev. Lett., 91, 146401 2003

[49] J. P. Perdew and K. Schmidt, "in Density Functional Theory and Its Application to Materials", edited by V. Van Doren, C. Van Alsenoy, and P. Geerlings , AIP, Melville, NY, 2001

[50] J. Heyd and G. E. Scuseria, "Efficient hybrid density functional calculations in solids: Assessment of the Heyd–Scuseria–Ernzerhof screened Coulomb hybrid functional", J. Chem. Phys., 121, 1187, 2004

[51] Z. Yan, J. P. Perdew, and S. Kurth, "Density functional for short-range correlation: Accuracy of the random-phase approximation for isoelectronic energy changes", Phys. Rev. B., 61, 16430, 2000

[52] F. Furche, "Molecular tests of the random phase approximation to the exchange-correlation energy functional", Phys. Rev. B., 64, 195120, 2001

[53]M. Fuchs, and X. Gonze, "Accurate density functionals: Approaches using the adiabatic-connection fluctuation-dissipation theorem", Phys. Rev. B., 65, 235109, 2002

[54] J. F. Dobson, J. Wang, and T. Gould, "Correlation energies of inhomogeneous many-electron systems", Phys. Rev. B., 66, 081108, 2002

[55] S. Limpijunmnong, S. N. Rashkeev, and W.R.L. Lambrecht, "Electronic structure and optical properties of $ZnGeN_2$", MRS Internet J. Nitride Semicond. Res., 4S1:G6.11, 1999

[56] M. Methfessel, M. van Schilfgaarde, and R. A. Casali, "A full-potential LMTO method based on smooth hankel functions", In H. Dreysse, editor, Electronic Structure and Physical Properties of Solids. The Use of the LMTO Method", volume 535 of Lecture Notes in Physics, P. 114. Berlin Springer Verlag, 2000

[57] T. Kotani and M. van Schilfgaarade, "Fusion of the LAPW and LMTO methods: The augmented plane wave plus muffin-tin orbital method", Phys. Rev. B., 81, 125117, 2010

[58] V. L. Shaposhnikov, A. V. Krivosheeva, F. Arnaud D'Avitaya, J. L. Lazzari, and V. E. Borisenko, "Structural, electronic and optical properties of II-IV-N_2 compounds, (II=Be, Zn; IV=Si, Ge)", Phys. Stat. Solidi(b), 245: 142-148, 2008

[59] W. R. L. Lambrecht, E. Alldredge, and K. Kim, "Structure and phonons of ZnGeN$_2$", Phys. Rev. B., 72(15): 155202, 2005

[60] T. R. Paudel and W.R.L. Lambrecht, "First-principles calculation of the zone center phonons in ZnSiN$_2$: Comparison with infrared data", Phys. Rev. B., 76(11): 115205, 2007

[61] T. J. Peshek, T. R. Paudel, K. Kash, and W. R. Lambrecht, "Vibrational modes in ZnGeN$_2$: Raman study and theory", Phys. Rev. B., 77(23): 235213, 2008

[62] T. R. Paudel and W. R. L. Lambrecht, "First-principles study of phonons and related ground-state properties and spetra in Zn-IV-N2 compounds", Phys.Rev. B., 78(11); 115204, 2008

[63] A. Punya, T. R. Paudel, and W.R.L.Lambrecht, "Electronic and lattice dynamical properties of II-IV-N_2 semiconductors", Phys. Stat. Solidi C., 8, 2492-2499, 2011

[64] J. Heyd, G. E. Scuseria , M. Ernzerhof, "Screened hybrid density functionals applied to solids", J. Chem. Phys., 124 ,219906,2006

[65] X. Gonze, "First-principles responses of solids to atomic displacements and homogenous electric fields: Implementation of a conjugate-gradient algrorithm", Phys. Rev. B., 55(16): 11337-11354, 1997

[66] X. Gonze and C. Lee., "Dynamical matrices, Born effective charges, dielectric permittivity tensors, and interatomic force constants from density-functional perturbation theory", Phys. Rev. B., 55(16):10355-10368, 1997

[67] R. Viennois, T. Taliercio, V.Potin, A. Errebbahi, B.Gil, S.Charar, A. Haidoux, and J.-C. Tedenac, "Prospective investigations of orthorhombic $ZnGeN_2$: synthesis, lattice and optical properties", Mater. Sci. Eng.B., 82:45-49, 2001

[68] G.Kresse and J. Furthmüller, "Efficient iterative schemes for ab initio total-energy calculations using a plane-wave basis set", Phys. Rev. B., 54, 11169,1996

[69] G.Kresse and D. Joubert, "From ultrasoft pseudopotentials to the projector augmented wave method", Phys. Rev. B., 59, 1758, 1999

[70] M. Methfessel and A. T. Paxton, "High-precision sampling for Brillouin-zone integration in metals", Phys. Rev. B., 40, 3616,1989

[71] B. D. Cullity, "Elements of x-ray diffraction", second edition, Addison-Wesley Publishing Company, Inc., 1978

[72] F. Deng, H. Cao, L. Liang, J. Li, J. Gao, H. Zhang, R. Qin, and C. Liu, "Determination of the basic optical parameters of ZnSnN$_2$", OPTICS LETTERS, 40(7), 1282-1285, 2015

[73] A. N. Fioretti, A. Zakutayev, H. Moutinho, C. Melamed, A. Norman, M. Al-Jassim, E. S. Toberer, and A. C. Tamboli, "A Combinatorial Material Study on ZnSnN2 Solar Absorber", arXiv:1504.01819v1 [cond-mat.mtrl-sci] 8 Apr 2015

[74] G. L. Miessler and D. A. Tarr, "Inorganic chemistry", 4th edition, Pearson Prentice Hall, USA, 2011, pp 81-126

[75] T. L. Duan, J. S. Pan, and D. S. Ang, "Interfacial chemistry and valence band offset between GaN and Al$_2$O$_3$ studied by X-ray photoelectron spectroscopy", Applied Physics Letters, 102, 201604, 2013

[76] M. Futsuhara, K. Yoshioka, and O.Takai, "Structural, electrical and optical properties of zinc nitride thin films prepared by reactive rf magnetron sputtering", Thin Solid Films, 322, 274–281, 1998

[77] N. K. Jiang, "Reactive Sputtering Deposition and Characterization of Zinc Nitride and Oxy-Nitride Films for Electronic and Photovoltaic Applications", PhD thesis, The University of Toledo, 2013

[78] L. F. J. Piper, T. D. Veal, P. H. Jefferson, and C. F. McConville, "Valence-band structure of InN from x-ray photoemission spectroscopy", PHYSICAL REVIEW B, 72, 245319, 2005

[79] U. K. MISHRA, and J. SINGH, "SEMICONDUCTOR DEVICE PHYSICS AND DESIGN", Springer, The Netherlands, 2008

[80] P. D. C. King, T. D. Veal, C. E. Kendrick, L. R. Bailey, S. M. Durbin, and C. F. McConville, "InN/GaN valence band offset: High-resolution x-ray photoemission spectroscopy measurements", PHYSICAL REVIEW B, 78, 033308, 2008

[81] Shibin Krishna TC and Govind Gupta, "Band alignment and Schottky behaviour of InN/GaN heterostructure grown by low-temperature low-energy nitrogen ion bombardment", RSC Adv., 4, 27308, 2014

[82] N. C. Chen, P. H. Chang, Y. N. Wang, H. C. Peng, W. C. Lien, C .F. Shih, Chiu-An Chang, and G. M. Wu, "Schottky behavior at InN–GaN interface", Applied Physics Letters, 87, 212111, 2005

[83] S. M. Sze and K. K. Ng, "Physics of Semiconductor Devices", Third edition, Wiley, 2007

[84] K. R. Peta, B. G. Park, S .T .Lee, M. D. Kim, J. E. Oh, T. G. Kim, and V. R. Reddy, "Analysis of electrical properties and deep level defects in undoped GaN Schottky barrier diode", Thin solid films, 534, pp 603-608, 2013

[85] Y. Zhou, D. Wang, C. Ahyi, C. C. Tin, J. Williams, M. Park, N. M. Williams, A. Hanser, and E. A. Preble, "Temperature-dependent electrical characteristics of bulk GaN Schottky rectifier", J. Appl. Phys., 101, 024506, 2007

[86] H. Hosono, N. Kikuchi, N. Ueda, and H. Kawazoe, "Working hypothesis to explore novel wide band gap electrically conducting amorphous oxides and examples", J. Non-Cryst. Solids., 198–200, 165, 1996

[87] K. Nomura, H. Ohta, A. Takagi, T. Kamiya, M. Hirano, and H. Hosono, "Room-temperature fabrication of transparent flexible thin-film transistors using amorphous oxide semiconductors", Nature, 432, 488, 2004

[88] J. H. Lee, D. H. Kim, D. J. Yang, S. Y. Hong, K. S. Yoon, P. S. Hong, C. O. Jeong, H. S. Park, S. Y. Kim, S. K. Lim, S. S. Kim, "42.2: World's Largest (15-inch) XGA AMLCD Panel Using IGZO Oxide TFT", SID 08 Digest: SID International Symposium Digest of Technical Papers, May 20, 2008, vol. 39, pp. 626-628.

[89] K. S. S, T. S. Kim, J. S. Jung, M. K. Ryu, K. B. Park, B. W. Yoo, J.W. Kim, Y. G. Lee, J. Y. Kwon, S. Y. Lee, and J. M. Kim, "42.4L: Late-News Paper: 4 inch QVGA AMOLED Driven by the Threshold Voltage Controlled Amorphous GIZO (Ga_2O_3-In_2O_3-ZnO) TFT", SID 08 Digest: SID International Symposium Digest of Technical Papers, May 20, 2008, vol. 39, pp. 633-636

[90] S. E. Ahn et al.,"Metal Oxide Thin Film Photo-Transistor for Remote Touch Interactive Display". Advanced Materials, 24, 2631, 2012

[91] M. D. H. Chowdhury, P. Migliorato, and J. Jang, "Light induced instabilities in amorphous indium-gallium-zinc-oxide thin-film transistors", Appl. Phys. Lett., 97,173506, 2010

[92] M. Futsuhara, K. Yoshioka, and O. Takai, "Optical properties of zinc oxynitride thin films", Thin Solid Films, 17,322-325, 1998

[93] Y. Ye, R. Lim, and J. M. White, "High mobility amorphous zinc oxynitride semiconductor material for thin film transistors". J. Appl. Phys. 106, 074512, 2009

[94] H. S. Kim et al., "Anion control as a strategy to achieve high-mobility and high stability oxide thin-film transistors", Scientific Reports, 3, 1459, 2013

[95] E. H. Lee et al., "Nanocrystalline ZnON; High mobility and low band gap semiconductor material for high performance switch transistor and image sensor application", Scientific Reports, 4, 4948, 2014

[96] C. Palacio, J. M. Sanz, and J. M. Martinez-Duart, "PREFERENTIAL SPUTTERING EFFECTS IN TANTALUM NITRIDE THIN FILMS", Thin Solid Films, 124 , 243, 1985

[97] C. Wang, Z. Ji, K. Liu, Y. Xiang, and Z. Ye, "p-Type ZnOthin films prepared by oxidation of Zn3N2 thin films deposited by DC magnetron sputtering", J. Cryst. Growth., 259, 279, 2003

[98] Z. X. Zhang, X. J. Pan, L. X. Liu, Z. W. Ma, H. T. Zhao, L. Jia, and E. Q. Xie, "Green photoluminescence from Zn_3N_2 :Tb films prepared by magnetron sputtering", J. Appl. Phys., 105, 016101, 2009

[99] I. Bertoti, M. Mohai, J. L. Sullivan, and S. O. Saied, "Surface characterisation of plasma-nitrided titanium: an XPS study", Appl. Surf. Sci., 84, 357, 1995

[100] Y. Taur and T. H. Ning, "Fundamentals of Modern VLSI Devices", Second Edition, Cambridge Press, UK, 2009

[101] R. Long, Y. Dai, L. Yu, B. Huang, and S. Han, "Atomic geometry and electronic structure of defects in Zn_3N_2", Thin Solid Films, 516, 1297–1301, 2008